

DISSERTATION

# Advanced Macroscopic Transport Models

ausgeführt zum Zwecke der Erlangung des akademischen Grades  
eines Doktors der technischen Wissenschaften

eingereicht an der Technischen Universität Wien  
Fakultät für Elektrotechnik und Informationstechnik  
von

MARTIN-THOMAS VASICEK



Wien, im Oktober 2009

---

---

# Kurzfassung

---

**M**AKROSKOPISCHE TRANSPORTMODELLE zur Beschreibung des Ladungsträgertransports basierend auf der Boltzmann-Gleichung, wie das Drift-Diffusionsmodell sowie das Energie-Transportmodell, genügen ingenieurtechnischen Anwendungen und sind sehr effizient im Vergleich zu deutlich zeitaufwändigeren Monte Carlo Simulationen. Mit fortschreitender Bauteilminiaturisierung hin in den Deka-Nanometerbereich verlieren jedoch nacheinander das Drift-Diffusionsmodell und das Energie-Transportmodell ihre Gültigkeit. Wie in dieser Arbeit gezeigt wird, ist ein Transportmodell höherer Ordnung basierend auf den ersten sechs Momenten der Boltzmann-Gleichung eine effiziente Lösung, um die Genauigkeit zu erhöhen. Dabei spielt die Charakterisierung der Transportparameter eine entscheidende Rolle. Es wird gezeigt, dass ein Transportparametermodell, das auf Monte Carlo Tabellen beruht, eine sehr genaue Parameterbeschreibung zulässt.

Der theoretische Teil dieser Arbeit liefert einerseits eine Einführung in die bestehenden Simulationenmethoden des Quantentransports und andererseits wird auf die Ableitung von makroskopischen Transportmodellen höherer Ordnung sehr genau eingegangen. Näherungen bei den Herleitungen der Modelle und die wichtige Abschlussbedingung des Sechsmomenten-Modells werden beschrieben. Die zugrundeliegenden Ideen der Monte Carlo Simulation und die Technik der Expansion der Verteilungsfunktion in Kugelflächenfunktionen werden besprochen. Beide Methoden liefern Referenzergebnisse zur Verifikation der entwickelten makroskopischen Transportmodelle.

Um den Gebrauch für moderne Applikationen zu verdeutlichen, beschäftigt sich der praktische Teil dieser Arbeit mit dem Gültigkeitsbereich der makroskopischen Transportmodelle. Dabei wird eine genaue Untersuchung bezüglich des Verhaltens der Modelle in einem dreidimensionalen Elektronengas durchgeführt. Kurzkanaleffekte werden dabei analysiert. Das Hauptaugenmerk dieser Arbeit liegt im Verhalten von Transportmodellen in der Inversionsschicht eines UTB SOI MOSFET-Bauteils. Eine genaue Studie im homogenen Inversionskanal bezüglich des Einflusses der Oberflächenrauigkeit und der Quantisierung auf Transportparameter wird mit Hilfe der Subband Monte Carlo Methode durchgeführt. Um die gesamte Inversionsschicht eines Bauteils zu berücksichtigen, wurde ein zweidimensionales Sechsmomenten-Modell basierend auf Subband Monte Carlo Tabellen entwickelt. Die Resultate wurden mit der sehr genauen Bauteil-Subband Monte Carlo Methode als Referenz verglichen. Abschließend wurden Transportparameter höherer Ordnung sowie die empirische Abschlussbedingung für das Sechsmomenten-Modell in Legierungen wie SiGe oder GaAs untersucht.

---

# Abstract

---

THE CHARACTERIZATION of carrier transport for engineering applications with macroscopic models based on *Boltzmann's* transport equation, like the drift-diffusion model or the energy transport model, are very efficient compared to the time consuming Monte Carlo technique. However, by aggressive downscaling of the device dimensions into the deca-nanometer regime, both the drift-diffusion and the energy transport model continuously lose their validity. As will be pointed out, an efficient solution to extend the range of accuracy is to consider the first six moments of *Boltzmann's* transport equation. In the analysis of these higher-order macroscopic models up to the sixth order, it is crucial to describe the transport parameters with as few simplifying assumptions as possible. It turns out to be a very precise technique to extract these transport parameters from homogeneous Monte Carlo simulations.

The theoretical part of this thesis gives an introduction into quantum transport and a thorough derivation of macroscopic transport models up to the sixth order. The assumptions made during the derivation and their consequences as well as the closure problem of the six moments model are described in detail. The basic ideas behind the Monte Carlo technique and the Spherical Harmonics Expansion method, which both serve as references to the macroscopic transport model simulations, are illustrated.

The practical part deals with an analysis of the validity of higher-order macroscopic transport models. First, investigations concerning the behavior of the macroscopic models within the three dimensional electron gas using transport parameter models extracted from fullband Monte Carlo tables is given. Short channel effects as well as a benchmark to the Spherical Harmonics method are demonstrated. The second and the main part of this section shows the coverage of inversion layer effects by two dimensional higher-order transport models. A detailed study concerning the impact of surface roughness scattering and quantization on higher-order transport parameters is given using a self-consistent Subband Monte Carlo simulator. In order to describe carrier transport in the inversion layer of a whole device, a two dimensional six moments model based on Subband Monte Carlo tables has been developed and the model predictions are benchmarked with device Subband Monte Carlo simulations. Finally, a Monte Carlo higher-order parameter study in material alloys as SiGe and GaAs is given, and the empirical closure relation of the six moments model is discussed.

---

# Acknowledgment

---

FIRST AND FOREMOST I want to express my gratitude to my adviser *Prof. Tibor Grasser* for giving me the opportunity to join his research group and the chance to attend at several scientific conferences. He impressed me not only with his persistent way of solving scientific problems, but also with his positive and motivating mood. He amused me with his daily sarcastic remarks.

Furthermore, I am indebted to *Prof. Siegfried Selberherr* and *Prof. Erasmus Langer*, the head of the Institute, for the excellent working conditions, and the calm working climate, which serves as a basis for world-class scientific work. *Prof. Hans Kosina* impressed me with his deep theoretical knowledge as well as his ability to pass it even in the most hectic days on.

Furthermore, I owe gratitude to *Prof. Johann Summhammer*, who kindly agreed to serve on my examination committee.

Special thanks go to *Prof. David Esseni* and to *Prof. Pierpaolo Palestri* from the University of Udine, who gave me the chance to work in their group, and to learn a lot about Monte Carlo simulations. The results of the code developed is one of the cornerstone of this thesis.

I am also indebted to *Prof. Christoph Jungemann*, who provided me a Spherical Harmonics code and answered a lot of my questions concerning the usability of his simulator.

I enjoyed the luck to work closely together with many colleagues. *Martin Wagner*, one of my roommates, bootstrapped me at the institute and helped me to settle down into the world of Microelectronics. Thank you for carefully proofreading my thesis and for many discussions and suggestions not only concerning our work, but also in daily life. I am also grateful to *Johann Cervenka* for all his efforts and help in the model implementations into MINIMOS-NT, to *Enzo Ungersböck* and *Markus Karner*, who introduced me into the Vienna Monte Carlo simulator VMC and into the Vienna Schrödinger-Poisson solver VSP, *Viktor Sverdlov* for many discussions about quantum physics, *Mahdi Pourfath*, *Wolfgang Gös*, *Stanislav Tyaginov* for being very cooperative and helpful roommates, *Paul-Jürgen Wagner* for the help with the typesetting system L<sup>A</sup>T<sub>E</sub>X, *Oliver Triebel*, one of the MINIMOS-NT experts at the institute, and *Ivan Starkov*, who assisted me with Monte Carlo simulations.

## ACKNOWLEDGMENT

---

During my stay at the institute I had the pleasure to collaborate on different levels with many other colleagues I have a high regard for: *Oskar Baumgartner, Siddhartha Dhar, Robert Entner, Otmar Ertl, Philipp Hehenberger, Gregor Meller, Goran Milovanovic, Vassil Palankovski, Karl Rupp, Philipp Schwaha, Franz Schanovsky, Stanislav Vitanov, and Thomas Windbacher* as well as those I apologize not to mention here. I want to express my warmest thanks also to the administration staff, namely *Manfred Katterbauer, Ewald and Christoph Haslinger*, and to *Renate Winkler*.

Above all, I want to thank my family. My parents made possible all of my studies by their continuous support. They have strongly influenced my way, visions, and they have implanted in me the values that really matter in life. My wife *Andrea* provided me with love and understanding for endless working days and encouraged me whenever possible. And of course, there is my little sunshine *Sophie*, most probably the greatest success of my life!

---

# Contents

---

|   |             |
|---|-------------|
| <b>Kurzfassung</b>                                      | <b>i</b>    |
| <b>Abstract</b>   | <b>ii</b>   |
| <b>Acknowledgment</b>                                   | <b>iii</b>  |
| <b>Contents</b>   | <b>v</b>    |
| <b>List of Symbols</b>                                  | <b>viii</b> |
| Notation . . . . .                                      | viii        |
| Physical Quantities . . . . .                           | ix          |
| Constants . . . . .                                     | x           |
| <b>List of Figures</b>                                  | <b>xi</b>   |
| <b>1 Introduction</b>                                   | <b>1</b>    |
| <b>2 Theory of Transport Modeling</b>                   | <b>3</b>    |
| 2.1 Basic Equations . . . . .                           | 5           |
| 2.1.1 Derivation of <i>Poisson's</i> Equation . . . . . | 5           |
| 2.1.2 <i>Schrödinger-Poisson</i> System . . . . .       | 6           |
| 2.1.3 <i>Boltzmann's</i> Transport Equation . . . . .   | 9           |
| 2.1.3.1 The Distribution Function . . . . .             | 9           |
| 2.1.3.2 Diffusion Approximation . . . . .               | 9           |

## CONTENTS

---

|          |   |           |
|----------|---|-----------|
| 2.1.3.3  | Derivation of <i>Boltzmann's</i> Transport Equation . . . . . | 10        |
| 2.2      | Band Structure . . . . .                                      | 13        |
| 2.2.1    | Bulk . . . . .  | 13        |
| 2.2.2    | Subbands . . . . .  | 15        |
| 2.3      | Quantum Transport . . . . .                                   | 16        |
| 2.3.1    | Non-Equilibrium <i>Green's</i> Function Method . . . . .      | 16        |
| 2.3.2    | <i>Wigner</i> Monte Carlo . . . . .                           | 19        |
| 2.3.3    | Quantum Macroscopic Models . . . . .                          | 20        |
| 2.3.4    | Quantum Correction Models . . . . .                           | 21        |
| 2.4      | Semi-Classical Transport . . . . .                            | 22        |
| 2.4.1    | Method of Moments . . . . .                                   | 22        |
| 2.4.2    | Modeling of the Scattering Operator . . . . .                 | 25        |
| 2.4.3    | Macroscopic Transport Models . . . . .                        | 25        |
| 2.4.3.1  | Drift-Diffusion Transport Model . . . . .                     | 26        |
| 2.4.3.2  | Energy Transport Model . . . . .                              | 28        |
| 2.4.3.3  | Six Moments Transport Model . . . . .                         | 29        |
| 2.4.3.4  | Transport Parameter Modeling . . . . .                        | 33        |
| 2.4.4    | Monte Carlo Method . . . . .                                  | 35        |
| 2.4.4.1  | Free Flight - Self Scattering . . . . .                       | 35        |
| 2.4.4.2  | Scattering Events . . . . .                                   | 37        |
| 2.4.4.3  | Fundamental Statistics . . . . .                              | 37        |
| 2.4.5    | Spherical Harmonics Expansion . . . . .                       | 38        |
| <b>3</b> | <b>The Three-Dimensional Electron Gas</b>                     | <b>43</b> |
| 3.1      | Table Based Macroscopic Transport Models . . . . .            | 43        |
| 3.2      | Device Studies . . . . .                                      | 46        |
| 3.2.1    | Long Channel Devices . . . . .                                | 46        |
| 3.2.2    | Short Channel Effects . . . . .                               | 46        |
| 3.2.2.1  | Velocity Overshoot . . . . .                                  | 46        |
| 3.2.2.2  | Hot Electrons . . . . .                                       | 48        |
| 3.2.2.3  | Hot and Cold Electrons . . . . .                              | 49        |
| 3.2.2.4  | Impact Ionization . . . . .                                   | 52        |

## CONTENTS

---

|          |  |            |
|----------|--|------------|
| 3.2.3    | Application of Higher-Order Models on Deca-Nanometer Devices . . . . . | 53         |
| <b>4</b> | <b>Homogeneous Transport in Inversion Layers</b>                       | <b>59</b>  |
| 4.1      | Subband Monte Carlo Model . . . . .                                    | 59         |
| 4.2      | Surface Roughness Scattering . . . . .                                 | 60         |
| 4.3      | Influence of SRS . . . . .   | 63         |
| 4.4      | Comparison with Bulk Simulations . . . . .                             | 71         |
| <b>5</b> | <b>Subband Macroscopic Models</b>                                      | <b>74</b>  |
| 5.1      | The Model . . . . .  | 74         |
| 5.2      | The Quantum Correction Model . . . . .                                 | 77         |
| 5.3      | Comparison with Device-SMC . . . . .                                   | 81         |
| 5.3.1    | Long Channel Device . . . . .  | 81         |
| 5.3.2    | Short Channel Devices . . . . .  | 82         |
| 5.4      | SRS in Macroscopic Models . . . . .                                    | 86         |
| 5.5      | Subband versus Bulk . . . . .  | 87         |
| <b>6</b> | <b>Material Investigations</b>   | <b>90</b>  |
| 6.1      | Higher-Order Parameter Extraction . . . . .                            | 90         |
| 6.1.1    | Silicon-Germanium . . . . .  | 90         |
| 6.1.2    | Gallium Arsenide . . . . .   | 95         |
| <b>7</b> | <b>Summary and Conclusion</b>  | <b>99</b>  |
|          | <b>Bibliography</b>  | <b>101</b> |
|          | <b>Own Publications</b>  | <b>113</b> |
|          | <b>Curriculum Vitae</b>  | <b>115</b> |



---

# List of Symbols

---

## Notation

|   |     |   |
|---|-----|---|
| $x$   | ... | Scalar                                  |
| $\mathbf{x}$  | ... | Vector                                  |
| $\text{tr}(E)$                                      | ... | Trace of the matrix $E$                 |
|   |     |   |
| $\mathbf{x} \cdot \mathbf{y}$                       | ... | Scalar (in) product                     |
| $\mathbf{x} \times \mathbf{y}$                      | ... | Vector (ex) product                     |
| $\mathbf{x} \otimes \mathbf{y}$                     | ... | Tensor product                          |
|   |     |   |
| $\partial_t(\cdot)$                                 | ... | Partial derivative with respect to $t$  |
| $\nabla$  | ... | Nabla operator                          |
| $\nabla x$  | ... | Gradient of $x$                         |
| $\nabla \cdot \mathbf{x}$                           | ... | Divergence of $\mathbf{x}$              |
| $\nabla^2 \mathbf{x}$                               | ... | <i>Laplace</i> operator of $\mathbf{x}$ |
|   |     |   |
| $\langle\langle \cdot \rangle\rangle$               | ... | Statistical average                     |
| $\langle \cdot \rangle$                             | ... | Normalized statistical average          |
|   |     |   |
| $f(\mathbf{r}, \mathbf{k}, t)$                      | ... | Distribution function                   |
| $f_w(\mathbf{r}, \mathbf{k}, t)$                    | ... | Wigner distribution function            |
| $\langle\langle \cdot \rangle\rangle_{\text{coll}}$ | ... | Collision operator                      |
| $\mathcal{H}$                                       | ... | <i>Hamiltonian</i> operator             |
| $s_\alpha$  | ... | Carrier charge sign                     |
| $\delta$  | ... | <i>Dirac</i> delta                      |
|   |     |   |
| $\{ \cdot, \cdot \}$                                | ... | <i>Poisson</i> bracket                  |

## Physical Quantities

| Symbol              | Unit  | Description                                    |
|---------------------|---|--|
| $\mathcal{E}$       | eV  | Energy   |
| $\mathcal{E}_f$     | eV  | <i>Fermi</i> energy                            |
| $\mathcal{E}_{c,v}$ | eV  | Conduction and valence band edge               |
| $\epsilon$          | AsV <sup>-1</sup> m <sup>-1</sup>               | Dielectric permittivity                        |
| $\varphi$           | V   | Electrostatic potential                        |
| $\tilde{\varphi}$   | V   | Effective electrostatic potential              |
| $\mathbf{k}$        | m <sup>-1</sup>                                 | Wave number vector                             |
| $\mathbf{v}$        | m s <sup>-1</sup>                               | Carrier velocity                               |
| $n$                 | m <sup>-3</sup>                                 | Electron density                               |
| $N_{\text{inv}}$    | m <sup>-2</sup>                                 | Inversion layer density                        |
| $N_{\text{dep}}$    | m <sup>-2</sup>                                 | Depletion layer density                        |
| $\tau_0$            | s   | Momentum relaxation time                       |
| $\tau_1$            | s   | Energy relaxation time                         |
| $\tau_2$            | s   | Energy flux relaxation time                    |
| $\tau_4$            | s   | Second-order energy relaxation time            |
| $\mu_0$             | m <sup>2</sup> V <sup>-1</sup> s <sup>-1</sup>  | Electron mobility                              |
| $\mu_1$             | m <sup>2</sup> V <sup>-1</sup> s <sup>-1</sup>  | Energy flux mobility                           |
| $\mu_2$             | m <sup>2</sup> V <sup>-1</sup> s <sup>-1</sup>  | Second-order energy flux mobility              |
| $E_{\text{eff}}$    | V/m   | Effective field                                |
| $m^*$               | kg  | Effective mass                                 |
| $m_1^*$             | kg  | Longitudinal effective mass                    |
| $m_t^*$             | kg  | Transversal effective mass                     |
| $D$                 | eV <sup>-1</sup> m <sup>-3</sup>                | Density of states                              |
| $\psi$              | m <sup>-3/2</sup>                               | Three-dimensional wavefunction                 |
| $\mathcal{H}_R$     | eV  | <i>Hamilton</i> operator of the channel system |
| $\sigma$            | eV  | Coupling matrix                                |
| $\sigma^\dagger$    | eV  | Conjugate complex form of $\sigma$             |
| $\Sigma$            | eV  | Self-energy                                    |
| $I$                 | A   | Ballistic current                              |
| $\mathbf{F}$        | N   | Generalized Force                              |
| $\mathbf{E}$        | Vm <sup>-1</sup>                                | Electric field                                 |
| $w_0$               | m <sup>-3</sup>                                 | Zeroth moment                                  |
| $w_1$               | eV m <sup>-3</sup>                              | Second moment                                  |
| $w_2$               | eV <sup>2</sup> m <sup>-3</sup>                 | Fourth moment                                  |
| $w_3$               | eV <sup>3</sup> m <sup>-3</sup>                 | Sixth moment                                   |
| $\mathbf{V}_0$      | s <sup>-1</sup> m <sup>-2</sup>                 | First moment                                   |
| $\mathbf{V}_1$      | eV s <sup>-1</sup> m <sup>-2</sup>              | Third moment                                   |
| $\mathbf{V}_2$      | eV <sup>2</sup> s <sup>-1</sup> m <sup>-2</sup> | Fifth moment                                   |

## LIST OF SYMBOLS

---

|                     |            |  |
|---------------------|------------|--|
| $R$                 | $s^{-1}$   | Net recombination rate                                     |
| $T_L$               | K          | Lattice temperature  |
| $T_n$               | K          | Electron temperature                                       |
| $A$                 | 1          | Dimension factor   |
| $\beta$             | 1          | Kurtosis   |
| $\Gamma$            | $s^{-1}$   | Scattering rate  |
| $\Theta$            | K          | Second-order temperature                                   |
| $\psi_n$            | $m^{-3/2}$ | Three-dimensional wavefunction of the unprimed valley      |
| $\psi_{n'}$         | $m^{-3/2}$ | Three-dimensional wavefunction of the primed valley        |
| $\psi_{n''}$        | $m^{-3/2}$ | Three-dimensional wavefunction of the double primed valley |
| $\mathcal{E}_n$     | eV         | Subbands of the unprimed valley                            |
| $\mathcal{E}_{n'}$  | eV         | Subbands of the primed valley                              |
| $\mathcal{E}_{n''}$ | eV         | Subbands of the double primed valley                       |
| $\Delta_r$          | m          | Displacement   |

## Constants

|         |     |                                    |  |
|---------|-----|------------------------------------|--|
| $h$     | ... | <i>Planck's constant</i> ,         | $6.6260755 \times 10^{-34}$ J s              |
| $\hbar$ | ... | Reduced <i>Planck's constant</i> , | $\hbar/(2\pi)$                               |
| $k_B$   | ... | <i>Boltzmann's constant</i> ,      | $1.3806503 \times 10^{-23}$ JK <sup>-1</sup> |
| $q$     | ... | Elementary charge,                 | $1.6021892 \times 10^{-19}$ C                |
| $m_0$   | ... | Electron mass,                     | $9.1093897 \times 10^{-31}$ kg               |

---

# List of Figures

---

|      |  |    |
|------|--|----|
| 2.1  | Hierarchy of transport models . . . . .  | 4  |
| 2.2  | Quantum confinement in a MOSFET structure . . . . .  | 7  |
| 2.3  | For increasing subbands the difference between the energy eigenvalues decreases and converge to zero for an infinite number of energy-eigenstates. In this limit the subband system becomes a bulk system. . . . .   | 8  |
| 2.4  | Conduction band and the first two wavefunctions of a thin film SOI MOSFET for different gate voltages. For increasing gate voltages the wavefunctions are shifted towards the interface. . . . .   | 8  |
| 2.5  | <i>Fermi–Dirac</i> distribution function for 0 K, 300 K, 500 K, and the limit $k_B T \ll \mathcal{E} - \mathcal{E}_f$ is demonstrated. In this limit, the <i>Fermi–Dirac</i> function can be approximated by a <i>Maxwell</i> distribution function. . . . . | 10 |
| 2.6  | Scattering event from one trajectory to another in phase space. Scattering events, which are assumed to happen instantly, change the carrier’s momentum, while the position is not affected (after [1]). . . . .   | 12 |
| 2.7  | Energy ellipsoids of the first conduction band within the first <i>Brillouin</i> zone of silicon (after [2]). . . . .  | 14 |
| 2.8  | Unprimed and primed subband ladders . . . . .  | 16 |
| 2.9  | Populations of the first two subbands in the unprimed, primed, and double primed valleys versus lateral field in a UTB SOI MOSFET test device. Relative occupations are shifted to higher subbands in each valley for higher fields. . . . .                 | 17 |
| 2.10 | Velocities of the first and second subband of the unprimed, primed, and double primed valleys as well as the average total velocity versus lateral electric field. . . . .   | 17 |
| 2.11 | The electron concentration of a single gate SOI MOSFET has been calculated classically, quantum-mechanically, together with the quantum correction models MLDA, <i>Van Dort</i> , and the improved MLDA (after [3]). . . . .                                 | 23 |

LIST OF FIGURES

---

2.12 Kurtosis for a 100 nm  $n^+nn^+$  structure calculated with the MC method. In the channel the kurtosis is lower than one, which means that the heated *Maxwellian* overestimates the carrier distribution function, while the *Maxwellian* underestimates the carrier distribution in the drain. . . . . 31

2.13 Ratio between the sixth moment obtained from three-dimensional bulk MC simulation and the analytical closure relation (2.124) of the six moments model for different values of  $c$  (see left part). The maximum peak at point B of the ratio as a function of the lattice temperature is shown on the right. . . . . 32

2.14 Distribution function at point B for lattice temperatures of 200 K, 300 K, and 400 K. The high energy tail of the carrier distribution function decreases for high lattice temperatures. . . . . 32

2.15 The ratio of the six moments model obtained from two-dimensional *Subband Monte Carlo* data with the analytical 2D closure relation of the six moments model for different  $c$  is presented. As can be observed is for the 2D case as well the best value. . . . . 33

2.16  $H_1, H_2$ , and  $H_3$  as functions of the energy with an effective field of 950 kV/cm. For low energies, the non-parabolicity factors approach unity. The non-parabolicity factors have been calculated out of *Subband Monte Carlo* simulations. . . . . 34

2.17 Flowchart of a MC Simulation (after [1]) . . . . . 36

2.18  $Y_{10}$  and  $Y_{11}$  in polar coordinates . . . . . 39

2.19 A comparison of the low and high-field mobility as a function of the doping in the bulk calculated with the SHE method and the drift-diffusion model. In the SHE simulation, only the first *Legendre* polynomial has been taken into account. . . . 41

2.20 The velocity profile of an  $n^+nn^+$  structure calculated with a device MC simulation and with a SHE simulator taking 1, 5, 9, and 15 *Legendre* polynomials (LP) into account. . . . . 41

3.1 Carrier mobility  $\mu_0$ , energy flux mobility  $\mu_1$ , and second-order energy flux mobility  $\mu_2$  versus driving field for different doping concentrations. For fields higher than 100 kV/cm, the mobilities are independent of the doping concentration, while for low fields the values of the mobilities of the low doping case is high compared to high doping concentrations. . . . . 44

3.2 Energy-relaxation time  $\tau_1$  and second-order energy relaxation time  $\tau_2$  extracted from bulk MC simulations as a function of the kinetic energy for different bulk dopings. For very high energies, the relaxation times decrease due to the increase of optical phonon scattering. . . . . 45

3.3 Bulk velocity of electrons as a function of the driving field  $E_{\text{abs}}$  for a doping of  $10^{14} \text{ cm}^{-3}$ ,  $10^{16} \text{ cm}^{-3}$ , and  $10^{18} \text{ cm}^{-3}$ . In the low field regime, the electron velocity for high dopings is lower than the velocity of the low dopings, while the value of the velocity converges for high fields. . . . . 45

## LIST OF FIGURES

---

|      |   |    |
|------|---|----|
| 3.4  | Output currents for different $n^+nn^+$ structures calculated with DD, ET, and SM models. As a reference, SHE simulations are used. For 1000 nm, all models predict the same current, while the DD model underestimates the current for a channel length of 100 nm. . . . .   | 47 |
| 3.5  | Relative error of the current calculated with the DD, ET, and the SM model as a function of the channel length. A voltage of 1 V has been applied. While the ET and SM model is below 7.5 %, the DD model approaches to 16 % at a channel length of 100 nm. . . . .   | 47 |
| 3.6  | Velocity profiles of a 50 nm, 100 nm, and 200 nm long $n^+nn^+$ structure calculated with the MC method are presented after [4]. The velocity overshoot at the beginning of the lowly doped n-region is clearly visible. . . . .  | 48 |
| 3.7  | Carrier temperature $T_n$ as a function of the driving field in a homogeneous bulk simulation carried out with fullband MC. For lower fields, the carrier temperature is a function of $E^2$ , while for high fields, the temperature is a linear function of the driving field. . . . .  | 49 |
| 3.8  | Evolution of the distribution function inside an $n^+nn^+$ structure. The mixture of hot and cold electrons is expressed by the high-energy tail of the carrier distribution function. . . . .  | 50 |
| 3.9  | Kurtosis calculated for different source and drain doping concentrations in an $n^+nn^+$ structure with a channel length of 100 nm. The maximum peak of the kurtosis for high doping concentrations is very high compared to the low doping case. . . . .   | 51 |
| 3.10 | Carrier temperature $T_n$ together with second-order temperature $\Theta$ for a 1000 nm and a 60 nm device. A field of 50 kV/cm has been assumed. While in the long channel device a <i>Maxwellian</i> can be used, the high-energy tail in the short channel device in the drain region increases. . . . .   | 52 |
| 3.11 | Distribution function at point D of Fig. 3.8 for 40 nm, 60 nm, 80 nm, and 100 nm channel devices. As can be observed, the high-energy tail for increasing channel lengths decrease. . . . .   | 53 |
| 3.12 | Kurtosis $\beta$ and the carrier temperature for electric fields of 5 kV/cm, 20 kV/cm, and 50 kV/cm through a 100 nm channel $n^+nn^+$ device (the value of the fields in the upper left part is calculated at point A). For high fields, the kurtosis increases at the beginning of the drain region, which means that the high-energy tail of the distribution function is becoming very important. In the right upper part, the carrier temperature profile for different electric fields is shown. The kurtosis exceeds unity, while the carrier temperature drops down. The velocity profile for fields of 5 kV/cm and 50 kV/cm is shown on the lower part. For low fields, all models yield the same velocity profiles, which is an indication that the heated Maxwellian can be used. For high fields, a significant deviation of the velocity profiles can be observed. . . . . | 54 |

## LIST OF FIGURES

---

|      |  |    |
|------|--|----|
| 3.13 | The impact ionization rate is calculated with MC, the DD, ET, and the SM model for a 200 nm and a 50 nm structure. Due to the better modeling of the distribution function in the SM model, the results are closer to the MC data than the DD and the ET model (after [5]). . . . .  | 55 |
| 3.14 | Evolution of the carrier velocity profiles for decreasing channel lengths calculated with the DD, ET, and the SM model. The velocities are compared to the results obtained from SHE simulations. While the maximum velocity of the DD model is the saturation velocity $v_{\text{sat}}$ , the spurious velocity overshoot at the end of the channel in the ET and the SM model is clearly visible. The velocity overshoot at the beginning of the channel can be quantitatively identified at the 100 nm device in the ET and the SM model. . . . . | 56 |
| 3.15 | Velocity profile calculated with ET model and MC data. Due to the MC closure in the ET model for the fourth order moment and due to the improved modeling of the transport parameters, the spurious velocity overshoot at the end of the channel disappears (after [6]). . . . .   | 57 |
| 3.16 | Output currents of a 80 nm and a 40 nm channel length $n^+nn^+$ structure calculated with the DD, ET, SM, and SHE model. The ET model overestimates the current at 40 nm, while the SM model yields the most accurate result. . . . .  | 57 |
| 3.17 | Relative error in the current of the DD, ET, and the SM model for an $n^+nn^+$ structure in the channel range from 100 nm down to 40 nm. While the relative error of the SM model is below 6 %, the error of the DD and the ET model is at -30 % and 40 % for a channel length of 40 nm, respectively. . . . .   | 58 |
| 4.1  | Principle data flow of the parameter extraction for higher-order transport models. While transport is treated in the SMC code, the influence of the confinement perpendicular to the oxide interface is carried out by the <i>Schrödinger-Poisson</i> solver. . . . .  | 60 |
| 4.2  | Carrier velocity as a function of the driving field for different inversion layer concentrations. Due to surface roughness scattering, the carrier velocity decreases for increasing inversion layer concentrations. The maximum velocity is below the saturation velocity of bulk Si. . . . .   | 61 |
| 4.3  | The effective mobility as a function of the effective field [7]. For increasing bulk doping and for low inversion layer concentrations <i>Coulomb</i> scattering is the main scattering process, while for increasing $N_{\text{inv}}$ phonon scattering becomes more important. . . . .   | 62 |
| 4.4  | Higher-order mobilities as a function of the inversion layer concentration $N_{\text{inv}}$ for different lateral fields. For high fields the difference of the mobilities decreases. For low fields in a bulk MOSFET the carrier mobility is equal to the measurement data of Takagi. . . . .   | 63 |
| 4.5  | Conduction band edge as a function of the position for different inversion layer concentrations. For high $N_{\text{inv}}$ , the carriers are closer to the interface and hence they are more affected by surface roughness scattering than for low $N_{\text{inv}}$ . . . . .   | 64 |

## LIST OF FIGURES

---

|      |   |    |
|------|---|----|
| 4.6  | Conduction band and wavefunctions of a UTB SOI MOSFET for different electric fields. Both the wavefunctions and subbands are shifted with increasing lateral electric fields. The conduction band edge is affected by the change in the subband occupations. . . . .  | 64 |
| 4.7  | Influence of surface roughness scattering on $\mu_0$ , $\mu_1$ , and $\mu_2$ as a function of the lateral field for different $N_{\text{inv}}$ . For low fields, surface roughness scattering has a strong impact, while for high fields the mobilities are unaffected by SRS. . . . .  | 65 |
| 4.8  | Ratio between the mobilities neglecting and considering SRS for high and low $N_{\text{inv}}$ values as a function of the lateral field. For low $N_{\text{inv}}$ , the mobilities are unaffected. The carrier mobility is more affected by SRS than the higher-order mobilities. . .   | 66 |
| 4.9  | Ratio of the momentum relaxation time $\tau_0$ and energy flux relaxation time $\tau_3$ for different $N_{\text{inv}}$ as a function of the driving field. Surface roughness scattering influences $\tau_0$ more than $\tau_3$ , especially for high inversion layer concentrations. . .  | 67 |
| 4.10 | Influence of surface roughness scattering on the electron velocities for different $N_{\text{inv}}$ . For decreasing $N_{\text{inv}}$ , SRS loses the influence on the carrier velocity. Due to non-parabolic bands and quantization, the velocity is below the saturation velocity of the bulk. . . . .  | 67 |
| 4.11 | Influence of surface roughness scattering on $\tau_1$ and $\tau_2$ as a function of the kinetic energy of the carriers for different $N_{\text{inv}}$ . Due to the elastic scattering nature of SRS, the relaxation times are not affected by SRS. . . . .  | 68 |
| 4.12 | Energy relaxation time (left side) and the second-order relaxation time (right side) as a function of the inversion layer concentration for different lateral electric fields. For a field of 50 kV/cm and high $N_{\text{inv}}$ , $\tau_1$ and $\tau_2$ increase in contrast to high-fields, where the energy relaxation time remain constant. . . . . | 68 |
| 4.13 | First subband occupation of the unprimed, primed, and double primed valleys as a function of the inversion layer concentration for fields of 50 kV/cm and 100 kV/cm. Due to the light mass of the unprimed valley in transport direction, the subband occupation number is higher than in the other valleys. . . . .                                    | 69 |
| 4.14 | Mobilities of the unprimed, primed, and double primed valleys, and total average mobility as a function of the channel thickness. At about 3 nm, there is a maximum in the total mobility. This is the point where the mobility of the unprimed valley is already high while the carrier mobility of the remaining valleys is low. .                    | 70 |
| 4.15 | Populations of the unprimed, primed, and double primed valleys as functions of the channel thickness. . . . .   | 70 |
| 4.16 | Carrier, energy-flux, and second-order energy flux mobility of SMC and bulk MC simulations. The mobilities obtained by bulk simulations are higher than in subband simulations. For high fields, the mobilities from subband simulations yield the same value as from bulk simulations. . . . .   | 71 |
| 4.17 | Comparison of the energy relaxation time and second-order energy relaxation time using 2D SMC data and 3D bulk MC data. For high energies both simulations converge to the same value. . . . .  | 72 |

---



## LIST OF FIGURES

---

|      |  |    |
|------|--|----|
| 4.18 | Comparison of the carrier temperature using 2D SMC data and 3D bulk MC data. Due to higher phonon scattering in the 2D case the temperature is lower than in the 3D case. . . . .  | 73 |
| 4.19 | Subband occupations as functions of the subband ladders in the unprimed, primed, and double primed valleys for electric fields of 1 kV/cm and 100 kV/cm. For high fields, the subband ladders in the primed and double primed valleys are occupied. . . . .  | 73 |
| 5.1  | The SP-SMC loop describes the transport of a two-dimensional electron gas in an inversion layer. After convergency is reached, the device simulator utilizes the extracted parameters to characterize transport through the channel of the whole device. . . . .   | 75 |
| 5.2  | Effective field profile throughout the whole device for several bias points. With the effective fields and the SMC tables, higher-order transport parameters can be modeled as a function of the effective field. . . . .  | 76 |
| 5.3  | Energy relaxation time and second-order relaxation time for different effective fields as a function of the kinetic energy of the carriers. For high carrier energies, the relaxation times of the different inversion layers yield the same value. . . . .  | 76 |
| 5.4  | Carrier and higher-order mobilities for different effective fields as a function of the lateral field. For high fields the mobilities converge to the same value. . . . .  | 77 |
| 5.5  | Second-order temperature $\theta = \beta T_n$ , carrier temperature $T_n$ , and kurtosis $\beta$ for different SOI MOSFETs with channel lengths of 100 nm, 60 nm, and 40 nm. For decreasing channel lengths the kurtosis increases due to the increase of the high energy tail of the distribution function. . . . .                       | 78 |
| 5.6  | Temperature and second-order temperature profiles for different drain voltages. For the low drain voltage case, the second-order temperature yields a similar result compared to the carrier temperature, while a significant deviation between $\theta$ and $T_n$ especially in the drain region can be observed for high fields. . . . . | 79 |
| 5.7  | Capacity versus gate voltages for devices with 40 nm, 60 nm, and 80 nm gate lengths calculated with the <i>Schrödinger-Poisson</i> solver and with the calibrated quantum correction model. For a gate voltage used in most simulations of 1.3 V both simulators yield the same result. . . . .  | 80 |
| 5.8  | Output characteristics of a 40 nm channel length UTB SOI MOSFET calculated with the DD, ET, SM models and, as a reference, with DSMC data. As can be observed, the SM model delivers a current very close to the SMC current. Neglecting the quantum correction model increases the output current of the macroscopic models. . . . .      | 80 |
| 5.9  | Output current of 1000 nm and 100 nm channel devices calculated with the DD, ET, and SM model are compared to the output current obtained by DSMC simulations. For the 1000 nm device, the results of all models converge. . . . .   | 81 |
| 5.10 | Output current of a 30 nm channel length device calculated with the DD, ET, SM models, and with the SMC method. The SM model predicts the most accurate result, while ET overestimates and DD underestimates the current, respectively. . . . .  | 82 |

---

## LIST OF FIGURES

---

|      |  |    |
|------|--|----|
| 5.11 | Evolution of the velocity profiles of a UTB SOI MOSFET with a channel length of 30 nm for drain voltages of $V_d = 0.2$ V, $V_d = 0.4$ V, $V_d = 0.6$ V, and $V_d = 0.8$ V. The spurious velocity overshoot, especially in the ET model is clearly visible for drain voltages of 0.8 V. The SM model predicts most accurate results. . . . . | 83 |
| 5.12 | Output current at $V_d = 1$ V as a function of the channel length. A significant increase in the current of the ET model at channel lengths below 80 nm can be observed, while the current from the DD model is below the current of the DSMC. The SM model yields the most accurate current. . . . .  | 84 |
| 5.13 | Relative error as a function of the channel length of the DD, ET, and the SM models. The error of the ET model increases rapidly for devices with a channel length below 80 nm where even the DD model becomes better. The SM model is the most accurate model for short channel devices. . . . .  | 84 |
| 5.14 | Transit frequencies as a function of the channel length. A significant increase of the frequency in the ET model at channel lengths below 80 nm can be observed, while the frequency from the DD model is below the frequency of the DSMC. The SM model yields the most accurate result. . . . .   | 85 |
| 5.15 | Relative error of the transit frequencies as a function of the channel length of the DD, ET, and the SM models. The error of the DD model is higher than the error of the current (see Fig. 5.13), while the SM model is here as well the most accurate model. . . . .   | 85 |
| 5.16 | Carrier and higher-order mobilities for a 40 nm channel length device. The influence of SRS at the beginning of the channel is stronger than at the end. . . . .   | 86 |
| 5.17 | Carrier temperature $T_n$ and second-order temperature $\Theta$ calculated once with MC tables considering SRS and neglecting SRS, respectively. As can be seen $T_n$ and $\Theta$ are unaffected by SRS. . . . .  | 87 |
| 5.18 | Output characteristics of a 40 nm channel length SOI MOSFET calculated with the DD, ET, and the SM model using SMC data with SRS and SMC data without SRS. . . . .   | 88 |
| 5.19 | Velocity profile of a 40 nm channel length SOI MOSFET computed with the two-dimensional DD, ET, and SM model neglecting SRS in the subband MC tables and with the 3D macroscopic models using fullband MC tables. . . . .  | 88 |
| 5.20 | Output characteristics of a 40 nm channel length SOI MOSFET calculated once with the 2D macroscopic models using SMC data without SRS and with their 3D counterpart using fullband MC data. . . . .  | 89 |
| 6.1  | Carrier mobility and higher-order mobilities for a 10 % and 40 % Ge composition, respectively as a function of the lateral electric field. Ge has got a deep influence on the mobilities for low fields, while for high-fields the influence of Ge on the mobilities decreases. . . . .  | 91 |

## LIST OF FIGURES

---

|      |  |    |
|------|--|----|
| 6.2  | Low field carrier mobility together with higher-order mobilities as a function of the Ge composition. The carrier mobility fits the data from [8] quite well. The minimum of the mobilities is at 40 %, while a high increase of the mobility values can be observed for Ge composition greater than 80 % . . . . .                              | 92 |
| 6.3  | The energy relaxation time (left) and the second-order relaxation time (right) for a Ge mole fraction of 10 % and 40 % as a function of the carrier energy. For the 10 % Ge case the relaxation times are lower than for the 40 % Ge case. . . . .   | 92 |
| 6.4  | Carrier velocities for different doping concentrations as a function of the electric field and for different Ge compositions. For high fields the velocities are independent of the doping concentrations, while the velocities for low Ge compositions are higher than for the 40 % case. . . . .   | 93 |
| 6.5  | Kurtosis for a 100 nm $n^+nn^+$ structure for Si and SiGe. In the channel region the kurtosis of SiGe is higher than in Si, while the kurtosis of Si exceeds the one of SiGe at the beginning of the drain region. . . . .   | 94 |
| 6.6  | Sixth moment obtained by MC simulations divided by the expression from equation (2.124) for different values of $c$ . The value 2.7 is also a very good choice in SiGe and is even improved compared to Si. . . . .  | 94 |
| 6.7  | Carrier mobility and higher-order mobilities for GaAs as a function of the lateral electric field. The values of the mobilities are very high with respect to the ones for Si. . . . .   | 95 |
| 6.8  | Energy relaxation time and the second-order relaxation time for GaAs obtained for different doping concentrations as a function of the kinetic energy. The energy relaxation time has its maximum at 100 meV, while the shape of the second-order energy relaxation time is completely different compared to the energy relaxation time. . . . . | 96 |
| 6.9  | The carrier velocity for different doping concentrations as a function of the driving field. For a field of 5 kV/cm the carrier velocity has its maximum, while for high fields the velocity decreases. . . . .  | 97 |
| 6.10 | $\Gamma$ - and L-valleys of GaAs are shown. For low fields the carriers are in the light hole $\Gamma$ -valley, while for high-fields the carriers are in the upper heavy hole valleys, decreasing the carrier velocity (after [9]). . . . .   | 97 |
| 6.11 | Kurtosis profile of the $n^+nn^+$ structure with a channel length of 100 nm of GaAs and Si. The kurtosis at the end of the channel is lower in GaAs than in Si, while the kurtosis of GaAs is beyond Si at the beginning of the drain region. . . . .  | 98 |
| 6.12 | Sixth moment obtained by MC simulations divided by the analytical expression from equation (2.124) for different values of $c$ . The lower-order moments for equation (2.124) have been taken from MC simulations. Note that $c = 2.7$ is also a good choice in GaAs. . . . .  | 98 |

'Start by doing what is necessary, then do what is possible, and suddenly you are doing the impossible.'

Francis of Assisi

# Chapter 1

---

## Introduction

---

WITH THE INVENTION of the microchip the digital revolution was initiated, which has deeply influenced human society. One of the consequences is the increase of interdependence of economics, politics or telecommunications, which are the cornerstones of globalization.

Life is getting faster due to the fact that nowadays almost everyone has a cell phone, a computer, and is an internet user. The demand for more calculation performance of electronic devices, especially in computational science, but also in daily life, constantly increases due to programs requiring more cpu power and memory.

Therefore, to speed up microchips, a tremendous downscaling of metal-oxide-semiconductor field-effect transistors (MOSFET) into the sub-micrometer regime has been maintained. *Gordon Moore*, a founder of Intel Corporation claimed in the year 1965 [10,11] that the transistors on a chip double every eighteen months. This statement is known as *Moore's law* and it has turned out to be valid for the last four decades. Furthermore, this downscaling trend seems to hold as well for the coming decades as predicted and institutionalized by the International Technology Road-map for Semiconductors (ITRS) [12]. Another way to make chips faster is to use alternative semiconductor materials and substrates. It was reported in [13] that by considering a substrate under the active region of a bulk MOSFET improves the performance up to 25 % to 30 %. Thus, silicon-on-insulator technology (SOI) reduces the power consumption, which has a strong impact on the life time of batteries. An advanced further development of SOI MOSFETs is to reduce not only the channel length, but also the body of the MOSFET, which results in the ultra thin body (UTB) SOI MOSFET.

Powerful simulation tools have been developed to investigate characteristics of such advanced devices. It has proved to be a good investment. They have become prerequisites for verification of device specifications before starting their production. An efficient way to describe important device quantities such as the output characteristics is to solve a system of partial differential-equations based on the semi-classical *Boltzmann's* transport equation. Numerical simulation of carrier transport dates back to the famous work of *Scharfetter* and *Gummel* [14], who proposed a robust discretization scheme of the drift-diffusion model, which is still in use today [15]. The typical drift-diffusion model just takes the ohmic and diffusive part of carrier transport into account, which is not very satisfying for small devices, where carrier heating plays an important role. A further development was proposed by the work of *Stratton* [16] in the year 1962, who

takes the first four moments of *Boltzmann's* transport equation into account and approximates the scattering operator by a microscopic relaxation time. The so called hydrodynamic transport model retains the carrier temperature, which makes it possible to describe non-local effects as the velocity overshoot. However, it was reported in several papers [17–19], that for decreasing channel lengths even the hydrodynamic model after *Stratton* becomes more and more inaccurate. To increase the accuracy within macroscopic models for decreasing channel lengths, higher-order transport models which go beyond the *Stratton* model, have been developed.

The three dimensional bulk case was successfully investigated by *Grasser* [20,21] using the first six moments of *Boltzmann's* transport equation. However, the carriers in a UTB SOI MOSFET, which is a very promising device candidate to prove the scaling path up to the end of the ITRS road map, are strongly affected by quantization and surface roughness scattering. Due to the quantum confinement, energy subbands occur in the inversion layer and one has to deal with a two-dimensional electron gas. For an accurate description of these very scaled devices, it is very important to investigate the behavior of higher-order transport models within inversion layers, which has not been done satisfactorily yet.

This thesis characterizes the behavior of macroscopic transport models up to the sixth order for both situations: The 3D bulk case and the 2D quantized inversion layer case and is organized as follows:

**Chapter 2** is devoted to the theory of transport modeling starting with an overview of existing transport models. A brief introduction into quantum transport is given, describing just the main ideas behind the models. The main focus is put on the semi-classical transport based on *Boltzmann's* transport equation. A detailed derivation of macroscopic transport models as the drift-diffusion, the energy transport as well as the six moments model are presented. Furthermore, as a benchmark to macroscopic models, the Monte Carlo method and the Spherical Harmonics Expansion approach are explained.

In **Chapter 3**, a three dimensional bulk study of macroscopic transport models is carried out. For comparative studies, results of both the Monte Carlo method and the Spherical Harmonics Expansion approach serve as a reference. The validity of higher-order macroscopic models within the 3D bulk regime is highlighted.

**Chapter 4** characterizes higher-order transport parameters with the developed self-consistent subband Monte Carlo simulator in a highly quantized system of the inversion layer channel of a UTB SOI MOSFET. The impact of inversion layer effects is scrutinized. Furthermore, a comparison with the 3D bulk system is carried out.

A further extension based on the subband Monte Carlo simulator explained in **Chapter 4** is shown in **Chapter 5**. The method to treat higher-order transport in the inversion layer of a whole device is demonstrated and compared to device subband MC simulations.

material study concerning the behavior of higher-order transport parameters in semiconductor alloys as SiGe and GaAs is given in **Chapter 6**.

Finally, **Chapter 7** gives a summary and conclusions.

'Plans are nothing; Plans are everything'

Dwight D. Eisenhower

## Chapter 2

---

# Theory of Transport Modeling

---

THE FUNDAMENTAL equation of semi-classical transport is *Boltzmann's* transport equation (BTE). A common transport model, which can be easily derived from BTE is the drift-diffusion model, which is the workhorse of today's Technology Computer Aided Design (TCAD) tools. However, driven by *Moore's* law, the device dimensions of modern semiconductors decrease into the deca-nanometer regime following that the drift-diffusion model gets more and more inaccurate. A solution is to use more sophisticated models based on BTE like the Monte Carlo approach (MC) [22–25]. The disadvantage of the MC technique is its high computational effort due to the statistical approach and hence rather less suitable for engineering applications. However, the results obtained from the MC simulation method are often in a good agreement with the experiment [1] and frequently used as a benchmark for other simpler models.

For engineering purposes, higher-order macroscopic models based on the method of moments such as the hydrodynamic, six moments, or even higher-order models are adequate approaches for modeling sub-microscopic devices [21]. A detailed discussion will follow in the sequel.

Another promising approach for solving the BTE is the method of spherical harmonics [26]. The underlying idea is to expand the distribution function into spherical harmonics and exploit the orthogonality of the basis (see Section 2.4.5).

Since the BTE is a semi-classical equation including both *Newton* mechanics and the quantum mechanical scattering operator, transport models, as explained above, are only valid in a certain regime, where quantum effects like source to drain tunneling play only a negligible role (see Fig. 2.1) [27–29].

In order to cover the range of gate lengths below 10 nm, where source to drain tunneling plays an important role, several quantum mechanical approaches have been developed. The *Landauer-Büttiker* approach is valid in a ballistic regime, where the carriers are not affected by scattering [30]. This approach is based on a generalization of the conduction characterized by the transmission and reflection of the carriers. However, in general, transport models in the deca-nanometer regime are based on the fundamental equation of quantum mechanics, the *Schrödinger* equation (see Fig. 2.1).

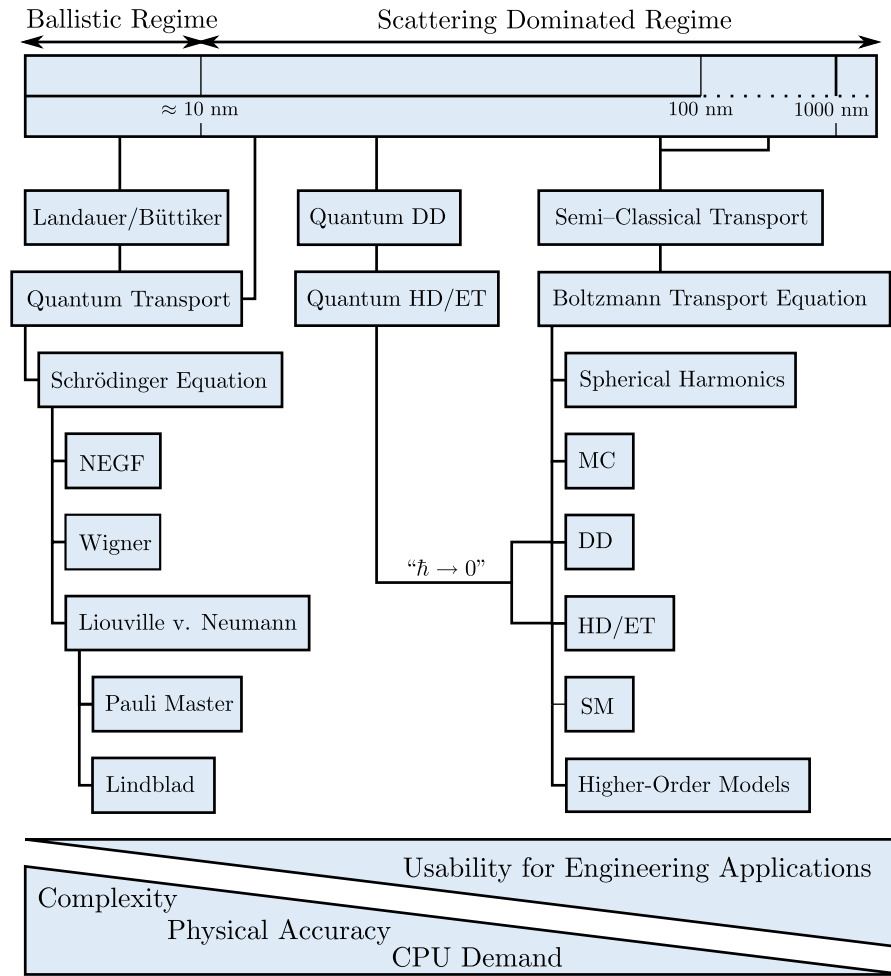


Figure 2.1: Hierarchy of transport models

The non-equilibrium *Green's* function (NEGF) formalism is a powerful method to handle open quantum systems [31]. The method can be used both in a ballistic and a scattering dominated regime (see Section 2.3.1). If the mean free path of the carriers is smaller than the device size, the system is in a scattering dominated regime, while if the mean free path is longer than the device the system can be described ballistically.

Other quantum approaches are based on a MC solution of the *Wigner* equation [32]. The advantage, compared to NEGF is that the methods comprise the coordinates and the momentum as the degree of freedom. In the NEGF method, the additional degree of freedom is the energy. In the classical limit of *Wigner* Monte Carlo, the results converge to the Monte Carlo results based on the BTE. A drawback of the *Wigner* equation is that the equation is not positive definite. In literature, this is known as the negative-sign problem [33]. This method can be used as well in the ballistic as in the scattering dominated regime.

The so called *Pauli Master* equation is derived from the *Liouville von Neumann* equation. The *Liouville von Neumann* equation describes the quantum evolution of the density matrix and forms the fundamental equation for the *Pauli* master equation. The *Pauli* master equation is a frequently used model of irreversible processes in simple quantum systems and can be used in

the ballistic and in the scattering dominated regions [34, 35].

The *Lindblad* master equation, the last point of the mentioned quantum models in Fig. 2.1, is the most general form of the *Liouville von Neumann* equation. It characterizes the non-unitary evolution of the density matrix. The elements of the density matrix are trace preserving and positive [36–38].

Other methods to cover gate lengths below the semi-classical regime are quantum macroscopic transport models. These models as the quantum drift-diffusion model or the quantum hydrodynamic model can be derived from the *Schrödinger* equation using the so called *Madelung* transformation [39]. A discussion will follow in Section 2.3.3.

All models have *Poisson's* equation in common, which describes the electrostatics of the system. For a new simulation strategy, it is also important to investigate the underlying material and to compare the simulation results with measurement data.

## 2.1 Basic Equations

The basic equations of quantum and classical device simulations, namely *Poisson's* equation, the *Schrödinger* equation, and the BTE with its solution, the distribution function, are derived and discussed in this section.

### 2.1.1 Derivation of *Poisson's* Equation

*Poisson's* equation is the basic equation of electrostatics [40, 41]. It can be derived inserting the definition of the electric field  $\mathbf{E}$

$$\mathbf{E} = -\nabla_{\mathbf{r}}\varphi, \quad (2.1)$$

into the second *Maxwell* equation

$$\nabla_{\mathbf{r}} \cdot \mathbf{D} = \rho. \quad (2.2)$$

Here,  $\varphi$  denotes the electrostatic potential,  $\rho$  represents the charge density, and  $\mathbf{D}$  is the electric displacement field defined as

$$\mathbf{D} = \epsilon\mathbf{E}. \quad (2.3)$$

Combining equation (2.1) with (2.2) yields *Poisson's* equation

$$\nabla_{\mathbf{r}} \cdot (\epsilon\nabla_{\mathbf{r}}\varphi) = -\rho, \quad (2.4)$$

whereby  $\rho$  can be expressed as

$$\rho = q(p - n + N_a - N_d). \quad (2.5)$$

$p$ , and  $n$  denote the holes and the electron concentration, respectively, whereas  $N_a$  and  $N_d$  are the concentration of acceptors and donors [42]. Inserting (2.5) into (2.4) yields

$$\nabla_{\mathbf{r}} \cdot (\epsilon\nabla_{\mathbf{r}}\varphi) = -q(p - n + N_a - N_d). \quad (2.6)$$

A complete description of transport within a device is achieved solving *Poisson's* equation self-consistently with the appropriate formulation of carrier transport within the semiconductor.



### 2.1.2 Schrödinger-Poisson System

In classical physics, the evolution in time and space of an ensemble of particles can be characterized using *Newton's* law. As described at the beginning of the chapter, transport below a gate length of 10nm cannot be treated anymore with classical physics. In the nanometer regime, particles must be described by their wave functions  $\psi(\mathbf{r}, t)$ , which can be derived from the time-dependent single particle *Schrödinger* equation [43]

$$\left(-\frac{\hbar^2}{2m}\nabla^2 + V(\mathbf{r})\right)\psi(\mathbf{r}, t) = i\hbar\partial_t\psi(\mathbf{r}, t). \quad (2.7)$$

The *Schrödinger* equation characterizes a particle moving in a region under the influence of the potential energy  $V(\mathbf{r})$  [44]. A solution strategy is a separation ansatz of the wavefunction into a time  $T(t)$  and space  $\phi(\mathbf{r})$  component

$$\psi(\mathbf{r}, t) = \phi(\mathbf{r})T(t). \quad (2.8)$$

With this separation, equation (2.7) can be decoupled into a time-dependent

$$i\hbar\partial_t T(t) = \alpha T(t) \quad (2.9)$$

and a space-dependent part

$$\left(-\frac{\hbar^2}{2m}\nabla^2 + V(\mathbf{r})\right)\phi(\mathbf{r}) = \alpha\phi(\mathbf{r}), \quad (2.10)$$

whereby  $\alpha$  denotes the energy eigenvalue. For a free particle ( $V(\mathbf{r}) = 0$ ), plain waves are the solution of the time-independent *Schrödinger* equation.

The quantum mechanical current density is defined as [45]

$$\mathbf{J} = \frac{\hbar}{2im} \left( \psi^\dagger(\mathbf{r}, t)\nabla_{\mathbf{r}}\psi(\mathbf{r}, t) - \psi^\dagger(\mathbf{r}, t)\psi(\mathbf{r}, t) \right), \quad (2.11)$$

with  $\psi^\dagger(\mathbf{r}, t)$  as the transposed conjugate complex form of  $\psi(\mathbf{r}, t)$ .

However, the situation is more complex in real semiconductors. Here, the band structure together with the electrostatic energy  $V(\mathbf{r}) = q\varphi$  as described in Section 2.1.1 plays an important role. Fig. 2.2 shows a cross-section of a typical p-type MOSFET device under inversion [46]. Due to the applied gate voltage, the conduction band forms a potential well. Therefore, the so called quantum confinement occurs, if the carriers in bound states cannot propagate to infinity. Hence, the potential well forms a boundary condition. Within this well, discrete energy levels, the so called energy subbands occur, which will be discussed in Section 2.2. Due to the quantum confinement, the carriers cannot move in the direction perpendicular to the interface, and therefore carrier transport is just in the two-dimensional plane parallel to the oxide [47]. For increasing lateral fields the carriers can go beyond the last occupied subband and become a three-dimensional carrier gas. This can be explained as follows:

Assuming a triangular potential, which is an analytical approximation for the inversion layer, the wavefunctions are the well known *Airy* functions, whereas the energy eigenvalues can be expressed as [48]

$$\mathcal{E}_i = c \left( i - \frac{1}{4} \right)^{2/3}, \quad (2.12)$$

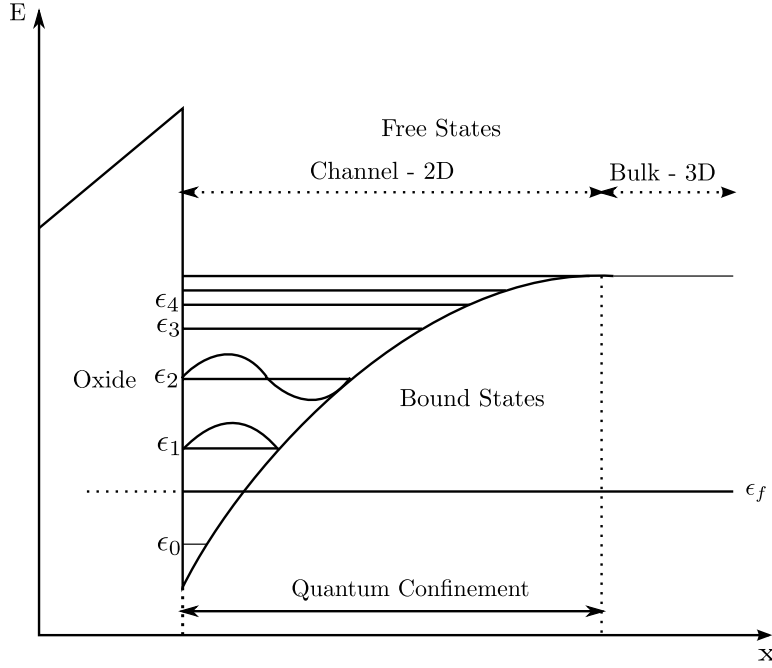


**Figure 2.2:** Quantum confinement in a MOSFET structure

with  $c$  as a constant and  $i$  is the number of the  $i$ th subband. The difference between the  $i$ th and the  $(i - 1)$ th subband can be written as

$$\mathcal{E}_i - \mathcal{E}_{i-1} = c \left( \left( i - \frac{1}{4} \right)^{2/3} - \left( (i - 1) - \frac{1}{4} \right)^{2/3} \right). \quad (2.13)$$

This difference as a function of the number of subbands is visualized in Fig. 2.3. For increasing number of subbands the energy gap decreases. Furthermore for an infinite number of energy eigenvalues this gap converges to zero. Thus, the subband system is transformed into a bulk system for an infinite number of subbands.

In order to correctly describe energy eigenvalues and wavefunctions in a device, the *Schrödinger* equation has to be solved self-consistently with *Poisson's* equation [2, 49]. The starting point for solving the system is a potential distribution, which leads to charge neutrality. Inserting the potential into the *Schrödinger* equation, one obtains the initial energy eigenvalues  $\mathcal{E}_l$  and wavefunctions  $\phi(\mathbf{r})$  for the quantum mechanical carrier concentration defined as

$$n(\mathcal{E}_c(\mathbf{r}), \mathcal{E}_f) = N_{\text{gv}} \sum_l \frac{1}{1 + \exp\left(\frac{\mathcal{E}_l - \mathcal{E}_f}{k_B T_n}\right)} |\phi(\mathbf{r})|^2.$$

Here,  $N_{\text{gv}}$  denotes the effective density of states

$$N_{\text{gv}} = 2g_v, \quad (2.14)$$

with  $g_v$  as the degeneracy of the system.

The next step is a recalculation of the potential by *Poisson's* equation followed by new wavefunctions and energy eigenvalues. These steps are performed in a loop until the update is below

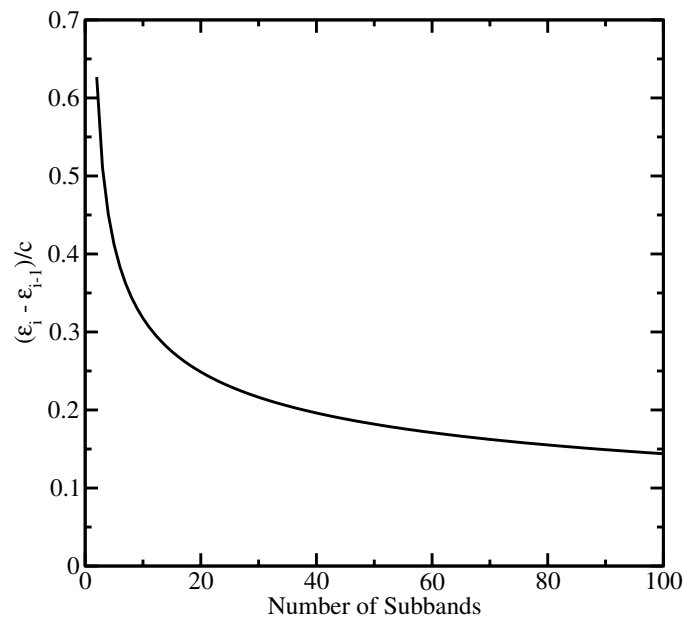


**Figure 2.3:** For increasing subbands the difference between the energy eigenvalues decreases and converge to zero for an infinite number of energy-eigenstates. In this limit the subband system becomes a bulk system.

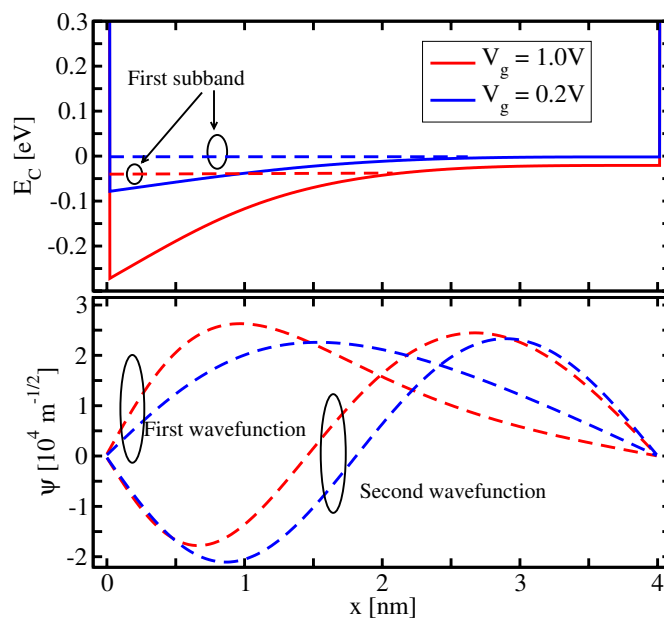


**Figure 2.4:** Conduction band and the first two wavefunctions of a thin film SOI MOSFET for different gate voltages. For increasing gate voltages the wavefunctions are shifted towards the interface.

a certain limit, thus convergency is reached. Results from a *Schrödinger-Poisson* solver are presented in Fig. 2.4 [50].

Here, the first energy subband together with two wavefunctions for different gate voltages as a function of the channel thickness are highlighted. Due to the shift of the wavefunctions to the oxide for high gate voltages, the carriers are strongly localized. Therefore, the impact of interface effects as surface roughness scattering for high gate voltages is very strong.

### 2.1.3 Boltzmann's Transport Equation

The basic equation of macroscopic transport description, the BTE, is derived using fundamental principles of statistical mechanics. The first part concerns the discussion of the solution of the BTE, whereas the second part is devoted to its derivation.

#### 2.1.3.1 The Distribution Function

The carrier distribution function  $f(\mathbf{r}, \mathbf{k}, t)$  is the solution of the BTE [1].  $f(\mathbf{r}, \mathbf{k}, t)$  is the probability of the number of particles having approximately the momentum  $\hbar\mathbf{k}$  near the position  $\mathbf{r}$  in phase space and time  $t$ . Taking *Pauli's* exclusion principle into account, the thermal equilibrium distribution function is the *Fermi-Dirac* function (equilibrium solution of the BTE)

$$f(\mathcal{E}) = C \frac{1}{\exp\left(\frac{\mathcal{E} - \mathcal{E}_f}{k_B T}\right) + 1}, \quad (2.15)$$

with  $C$  as a normalization factor, whereas  $\mathcal{E}_f$  is the *Fermi* energy. Fig. 2.5 shows the *Fermi-Dirac* function for 0 K, 300 K, and 500 K. For 0 K, the *Fermi-Dirac* function can be written as a step function  $\theta(\mathcal{E}_f - \mathcal{E})$ . Hence, all states are fully occupied below  $\mathcal{E}_f$ . For increasing temperatures, states above  $\mathcal{E}_f$  can be occupied, which results in a smoother transition. The energy range of the transition region is  $k_B T$  (see Fig. 2.5). If the relation

$$k_B T \ll (\mathcal{E} - \mathcal{E}_f) \quad (2.16)$$

is fulfilled, the *Fermi-Dirac* distribution function can be approximated by the *Maxwell* distribution function

$$f(\mathcal{E}) = C \exp\left(-\frac{\mathcal{E} - \mathcal{E}_f}{k_B T}\right). \quad (2.17)$$

The *Maxwell* distribution function neglects *Pauli's* exclusion principle. Therefore, the validity is limited to lowly doped, non-degenerate semiconductors.

#### 2.1.3.2 Diffusion Approximation

An important approximation used in the derivation of macroscopic transport models (see Section 2.4.3) is the *diffusion approximation*, which will be discussed here.

Every distribution function can be split into a symmetric  $f_s$  and an anti-symmetric  $f_a$  part as

$$f = f_s + f_a. \quad (2.18)$$

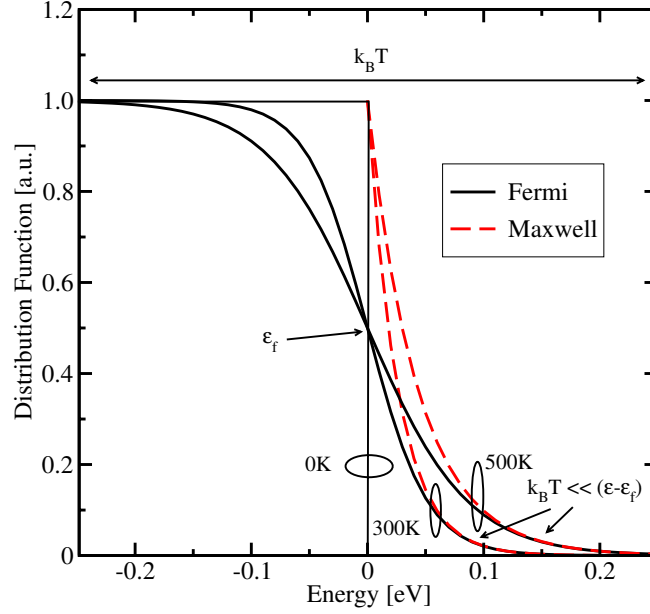


**Figure 2.5:** *Fermi–Dirac* distribution function for 0 K, 300 K, 500 K, and the limit  $k_B T \ll \mathcal{E} - \mathcal{E}_f$  is demonstrated. In this limit, the *Fermi–Dirac* function can be approximated by a *Maxwell* distribution function.

Within the *diffusion approximation* it is assumed that the displacement of the distribution function is small, which means that  $f_a$  is much smaller than  $f_s$  [51]. One of the consequences of this approximation is that only the diagonal elements of the average tensorial product of for instance the momentum

$$\hbar^2 \langle \mathbf{k} \otimes \mathbf{k} \rangle = n \iiint_{-\infty}^{\infty} \mathbf{k} \otimes \mathbf{k} f_s \, dk_x \, dk_y \, dk_z, \quad (2.19)$$

contribute, while the off diagonal elements can be neglected, due to symmetry reasons. The average operation used in equation (2.19) is the normalized statistical average and will be described in Section 2.4.3.

In general, the average energy of the carriers can be decomposed into

$$\langle \mathcal{E} \rangle = \langle \mathcal{E} \rangle_{\text{kin}} + \langle \mathcal{E} \rangle_{\text{therm}}, \quad (2.20)$$

where  $\langle \mathcal{E} \rangle_{\text{kin}}$  is the kinetic energy part and  $\langle \mathcal{E} \rangle_{\text{therm}}$  is the thermal energy part of the average carrier energy. Within the *diffusion approximation* the kinetic part of equation (2.20) is neglected.

### 2.1.3.3 Derivation of Boltzmann’s Transport Equation

The *Boltzmann’s* transport equation is derived from a fundamental principle of classical statistical mechanics, the *Liouville* theorem [52, 53]. The proposition asserts that the many particle

distribution function  $f(r_1, \dots, r_n, k_1, \dots, k_n, t)$  along phase-space trajectories  $\Gamma_i$  is constant for all times  $t$  [54]. With the total derivation of the many particle distribution function, the *Liouville* theorem can be expressed as

$$\frac{df}{dt} = \partial_t f + \sum_{i=1}^n \left( \frac{dr_i}{dt} \partial_{r_i} f + \frac{dk_i}{dt} \partial_{k_i} f \right) = 0. \quad (2.21)$$

Due to the *Hamilton* equations

$$\frac{d\mathbf{r}}{dt} = \nabla_{\mathbf{p}} \mathcal{H} \quad \text{and} \quad \frac{d\mathbf{p}}{dt} = -\nabla_{\mathbf{r}} \mathcal{H}, \quad (2.22)$$

and the *Poisson* bracket defined as

$$\{r, k\} = \sum_{i=1}^s (\partial_{r_i} r \partial_{k_i} \mathcal{H} - \partial_{k_i} r \partial_{r_i} \mathcal{H}), \quad (2.23)$$

the *Liouville* equation (2.21) can be written in a very compact form as

$$\partial_t f + \{f, \mathcal{H}\} = 0. \quad (2.24)$$

Equation (2.24) has to be solved in the  $\mathbb{R}^{2dM} \times \mathbb{R}$  space, where  $M$  is the number of particles and  $d$  is a dimension factor. The initial condition is defined as

$$f(r, k, 0) = f(r_0, k_0), \quad (r, k) \in \mathbb{R}^{2dM}. \quad (2.25)$$

$M$  is naturally very large and therefore the solution of (2.24) is very expensive.

To derive a lower-dimensional equation, *Vlasov* introduced a single particle *Liouville* equation with a force  $\mathbf{F}_{\text{eff}}$  [55]

$$\partial_t f(\mathbf{r}, \mathbf{k}, t) + \nabla_{\mathbf{p}} \mathcal{H} \nabla_{\mathbf{r}} f(\mathbf{r}, \mathbf{k}, t) + \mathbf{F}_{\text{eff}} \nabla_{\mathbf{p}} f(\mathbf{r}, \mathbf{k}, t) = 0. \quad (2.26)$$

Many-particle physics is taken into account in *Vlasov's* equation through the force  $\mathbf{F}_{\text{eff}}$  and the assumption that the probability to occupy a state along phase trajectories is constant. The force can be split into an external and a long-range interaction force. However, the main disadvantage of *Vlasov's* equation is that it does not provide a description of strong short-range forces such as scattering of particles with other particles or with the crystal. So, an extended *Vlasov* equation must be formulated to treat these important transport effects. Introducing the scattering operator  $Q_{\text{coll}}(f)$ , the balance equation for the distribution function must fulfill the conservation equation

$$\frac{df(\mathbf{r}, \mathbf{k}, t)}{dt} = Q_{\text{coll}}(f). \quad (2.27)$$

Hence, scattering allows particles to jump from one trajectory to another (see Fig. 2.6). With the full derivative of the distribution function and equation (2.22), the *Boltzmann's* transport equation (2.27) can be finally expressed in the common form as

$$\partial_t f + \nabla_{\mathbf{p}} \mathcal{H} \nabla_{\mathbf{r}} f - \nabla_{\mathbf{r}} \mathcal{H} \nabla_{\mathbf{p}} f = Q_{\text{coll}}(f). \quad (2.28)$$

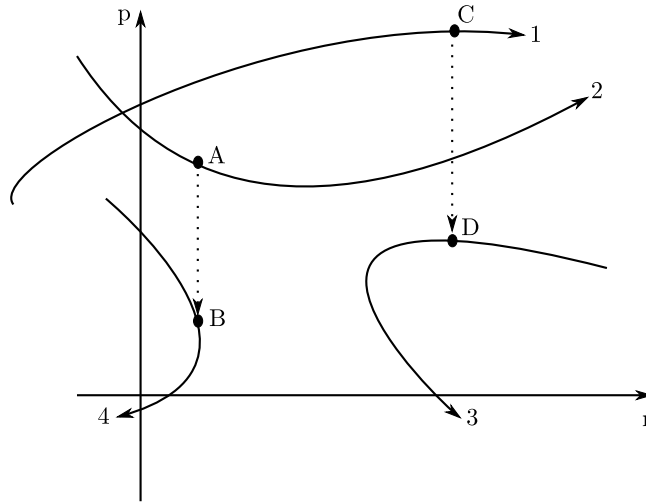


**Figure 2.6:** Scattering event from one trajectory to another in phase space. Scattering events, which are assumed to happen instantly, change the carrier's momentum, while the position is not affected (after [1]).

Equation (2.28) is a semi-classical equation containing *Newton* mechanics on the left side, and the quantum mechanical scattering operator on the right side. Still, it remains to formulate an expression for the scattering operator  $Q_{\text{coll}}$ . There exist many strategies for modeling the scattering operator [4, 16]. To develop solution strategies for the semi-classical differential equation, it is important to discuss the underlying limitations and assumptions of the BTE:

- The original many particle problem is replaced by a one particle problem with an appropriate potential. Due to the *Hartree-Fock* approximation [56], the contribution of the surrounding electrons to this potential is approximated by a charge density. Furthermore, the short range electron–electron interaction cannot be described. However, the potential of the surrounding carriers is treated by the electric field self-consistently.
- The distribution function  $f(\mathbf{r}, \mathbf{k}, t)$  is a classical concept due to the negligence of *Heisenberg's* uncertainty principle. The distribution function specifies both the position and the momentum at the same time.
- Due to the uncertainty principle, the mean free path of the particles must be longer than the mean *De Broglie* wavelength.
- Semi-classical treatment of carriers as particles obey *Newton's* law.
- Collisions are assumed to be binary and to be instantaneous in time and local in space.

It is important to have these limitations in mind, while deriving transport models based on the BTE. However, as has been reported in many publications [57–60], models based on the BTE give good results in the scattering dominated regime. Thus, it is a good starting point for simpler macroscopic transport models such as the drift-diffusion, the hydrodynamic, or even higher-order models.

## 2.2 Band Structure

The focus of this section is put on the band structure of bulk silicon and the occurrence of subbands. Furthermore, results are presented, which show the influence of the band structure on the transport properties.

### 2.2.1 Bulk

Carriers in a crystal are moving in a periodic potential energy  $V_{\text{periodic}}(\mathbf{r})$ . Due to this periodic potential, the solution of the time-independent *Schrödinger* equation

$$\left(-\frac{\hbar^2}{2m}\nabla^2 + V_{\text{periodic}}(\mathbf{r})\right)\phi(\mathbf{r}) = \mathcal{E}\phi(\mathbf{r}), \quad (2.29)$$

are the so called *Bloch* waves expressed as [61, 62]

$$\psi_{\mathbf{k}}(\mathbf{k}, \mathbf{r}) = u_{\mathbf{k}}(\mathbf{r}) \exp(i\mathbf{k}\mathbf{r}). \quad (2.30)$$

The boundary condition

$$u_{\mathbf{k}}(\mathbf{r} + a) = u_{\mathbf{k}}(\mathbf{r}) \quad (2.31)$$

must hold, with  $a$  as the lattice constant. Inserting the *Bloch* waves (2.30) into equation (2.29) the *Schrödinger* equation can be written as

$$\left(\frac{1}{m}\left(\frac{\hbar}{i}\nabla_{\mathbf{r}} + \hbar\mathbf{k}\right)^2 + V_{\text{periodic}}(\mathbf{r})\right)u_{\mathbf{k}} = \mathcal{E}(\mathbf{k})u_{\mathbf{k}}. \quad (2.32)$$

The so called  $\mathbf{k} \cdot \mathbf{p}$  method gives approximate solutions to (2.32) [63, 64]. Several other methods such as pseudo-potential calculations [65, 66], tight binding [67], *Hartree-Fock* [68], and density functional theory [69] have been proposed to calculate the full band structure within the first *Brillouin* zone.

If the band structure is already given,  $\mathcal{E}(\mathbf{k})$  can be expanded around the band edge minimum into a *Taylor* series as

$$\mathcal{E}(\mathbf{k}) = \mathcal{E}(0) + \partial_{\mathbf{k}}\mathcal{E}(\mathbf{k})|_{\mathbf{k}=0}\mathbf{k}_l + \frac{1}{2}\partial_{\mathbf{k}_l}\partial_{\mathbf{k}_m}(\mathcal{E}(\mathbf{k}))|_{\mathbf{k}=0}\mathbf{k}_l\mathbf{k}_m. \quad (2.33)$$

Here the *Taylor* series is truncated after the second derivative. The energy minimum is assumed at  $\mathbf{k} = 0$  following that the term with the first derivative can be neglected. Thus the energy can be expressed as

$$\mathcal{E}(\mathbf{k}) - \mathcal{E}(0) = \frac{1}{2}\partial_{\mathbf{k}_l}\partial_{\mathbf{k}_m}(\mathcal{E}(\mathbf{k}))\mathbf{k}_l\mathbf{k}_m. \quad (2.34)$$

With a comparison between equation (2.34) and the energy dispersion relation

$$\mathcal{E}(\mathbf{k}) = \frac{\hbar\mathbf{k}^2}{2m}, \quad (2.35)$$



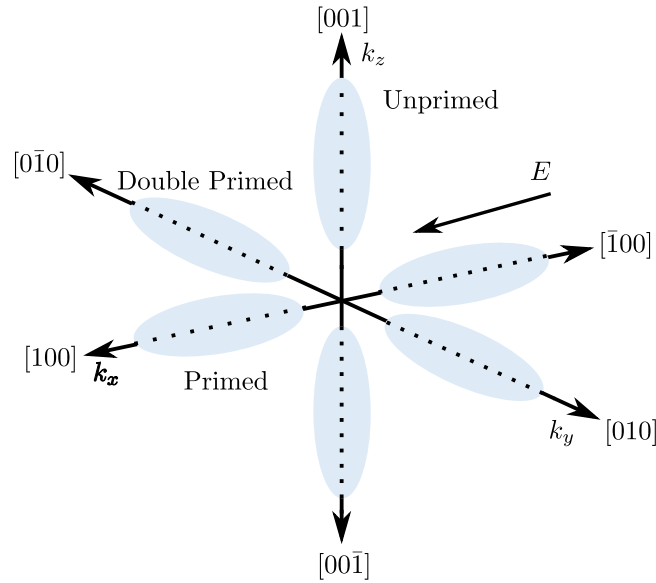


**Figure 2.7:** Energy ellipsoids of the first conduction band within the first *Brillouin* zone of silicon (after [2]).

the inverse effective mass tensor can be written as

$$\frac{1}{m_{lm}^*} = \frac{1}{\hbar^2} \partial_{k_l} \partial_{k_m} \mathcal{E}(\mathbf{k}) . \quad (2.36)$$

So electrons in a crystal can be assumed as free particles with a direction dependent mass. For silicon, the effective mass yields [44]

$$\frac{1}{m_{lm}^*} = \begin{pmatrix} \frac{1}{m_x} & 0 & 0 \\ 0 & \frac{1}{m_y} & 0 \\ 0 & 0 & \frac{1}{m_z} \end{pmatrix} . \quad (2.37)$$

Furthermore, the effective mass of cubic semiconductors depends on the crystallographic orientation of the applied field. With the so called longitudinal mass or heavy hole mass  $m_1^*$  and the transversal mass or light hole mass  $m_t^*$ , the energy dispersion relation can be defined as

$$\mathcal{E}(\mathbf{k}) = \frac{\hbar^2}{2} \left( \frac{k_l^2}{m_1^*} + \frac{k_t^2}{m_t^*} \right) . \quad (2.38)$$

Equation (2.38) is a band with ellipsoidal constant energy surfaces as depicted in Fig. 2.7. These are the six valleys of the first conduction band of silicon.

Due to the truncation after the second-order derivative of the *Taylor* series, the effective mass approximation is only valid for low fields. Thus, the assumption of parabolic bands is not valid anymore for high fields. With the introduction of a non-parabolicity factor  $\alpha$ , as proposed by Kane [47, 70, 71], the parabolic dispersion relation (2.35) can be rewritten into a first order correction

$$\mathcal{E}(1 + \alpha\mathcal{E}) = \frac{\hbar^2}{2} \left( \frac{k_l^2}{m_1^*} + \frac{k_t^2}{m_t^*} \right) . \quad (2.39)$$

A direct consequence of the band structure is the density of states, which describes the energetical density of electronic states per volume [1]

$$D(\mathcal{E}) = \frac{1}{V} \sum_{\mathbf{k}'} \delta(\mathcal{E} - \mathcal{E}(\mathbf{k})). \quad (2.40)$$

In the parabolic band approximation the density of states for one, two, and three-dimensions reads as

$$D_{1D}(\mathcal{E}) = \frac{2m^*}{\pi\hbar} \frac{1}{\sqrt{2m^*\mathcal{E}}}, \quad D_{2D}(\mathcal{E}) = \frac{m^*}{\pi\hbar^2}, \quad \text{and} \quad D_{3D}(\mathcal{E}) = \frac{m^*\sqrt{2m^*\mathcal{E}}}{\pi^2\hbar^3}. \quad (2.41)$$

For the non-parabolic dispersion relation (2.39) the density of states can be formed as

$$D_{1D}(\mathcal{E}) = \frac{2m^*}{\pi\hbar} \frac{1}{\sqrt{2m^*\mathcal{E}}}, \quad D_{2D}(\mathcal{E}) = \frac{m^*}{\pi\hbar^2} (1 + 2\alpha\mathcal{E}), \quad \text{and} \quad (2.42)$$

$$D_{3D}(\mathcal{E}) = \frac{m^*\sqrt{2m^*\mathcal{E}}}{\pi^2\hbar^3} \sqrt{(1 + \alpha\mathcal{E})(1 + 2\alpha\mathcal{E})}. \quad (2.43)$$

Note that in the two-dimensional case for non-parabolic bands the density of states is energy dependent, whereas for a parabolic band structure the density of states is energy independent. Equation (2.39) is valid up to energies of 1 eV [1]. Therefore, to model high-field transport, a more sophisticated description has to be found. One possibility, which is used in this work, is to calculate non-parabolic factors as a post processing step from *Monte Carlo* simulations. This procedure will be explained in Section 2.4.3.

### 2.2.2 Subbands

In Section 2.1.2, an introduction of the *Schrödinger–Poisson* loop including inversion layer effects has been given. In real devices within the crystallographic orientation [001], the valley, which has its longitudinal mass perpendicular to the interface surface, gives rise to a ladder of subbands, the so called unprimed valley, whereas the other valleys give rise to an other, higher lying ladder in the primed and double primed valleys [72]. It has been pointed out in [47] that by inserting the mass tensor (2.37) into the *Schrödinger* equation, the energy dispersion relation of the orientation [001] can be described as

$$\mathcal{E}(k_x, k_y) = \mathcal{E}_i + \frac{\hbar^2}{2} \left( \frac{1}{m_x} k_x^2 + \frac{1}{m_y} k_y^2 \right), \quad (2.44)$$

with  $z$  as the quantization direction.  $\mathcal{E}_i$  is the bottom energy of the  $i$ th subband. Equation (2.44) represents constant energy-parabolas above  $\mathcal{E}_i$ , the so called subband ladders. Inserting the corresponding longitudinal mass or the transversal mass of the valley into equation (2.44), one yields the subband ladders of the unprimed, primed, and double primed valleys, respectively.

Fig. 2.8 shows the subband ladders of the unprimed and primed valleys. Since the double primed and the primed valleys have the same energy subband values, due to the identical quantization mass, only the primed ladders are visualized. Due to the fact that the energy is inversely proportional to the quantization mass the energies of the primed ladders are higher than the ones from the unprimed ladders [73]. The quantization mass of the unprimed and primed

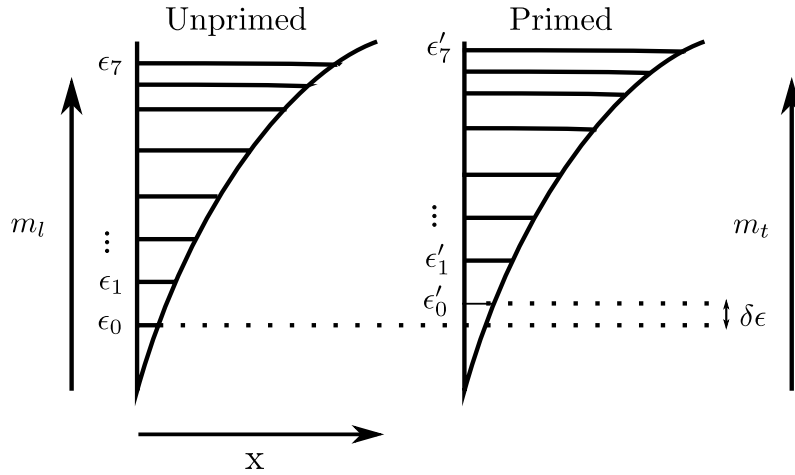


**Figure 2.8:** Unprimed and primed subband ladders

valleys are  $m_l^*$  and  $m_t^*$ , respectively. The subband occupations within high fields have got a strong influence on the carrier transport properties as demonstrated in Fig. 2.9 and Fig. 2.10

In Fig. 2.9, the subband occupation as a function of the driving field of an example device is presented. Carriers gain kinetic energy, which results in a re-occupation of higher subband ladders. Due to this re-occupation for high fields, the carrier wavefunctions are shifted within the inversion layer, which inherently affects the overlap integral of the scattering operator. Furthermore, the subband ladder reconfiguration leads to a variation of the spatial distribution function of the electrons, which itself has an impact on the shape of the potential well that forms the inversion channel.

The carrier velocity of the first and the second subband is displayed in Fig. 2.10. Due to different conduction masses in transport direction of each valley as well as a strong occupation of the primed valley in the high field regime (see Fig. 2.9), the total velocity is lower than in the unprimed and double primed valley [50]. A detailed discussion about subbands is given in [47].

## 2.3 Quantum Transport

An introduction of the most common quantum transport models, namely the non-equilibrium *Green's* function method, the *Wigner* Monte Carlo technique, and quantum macroscopic models is given, followed by a discussion of quantum correction models suitable for semi-classical models.

### 2.3.1 Non-Equilibrium *Green's* Function Method

The non-equilibrium *Green's* function (NEGF) is a very powerful technique to describe open systems fully quantum mechanically.

This method has been extensively used in modeling nanoscale transistors and is an efficient way of computing quantum effects in devices as subband quantization, tunneling, and quantum reflections. It is exact in the ballistic regime. Recently scattering processes have been included, which, however, requires considerable computational power. Furthermore NEGF al-

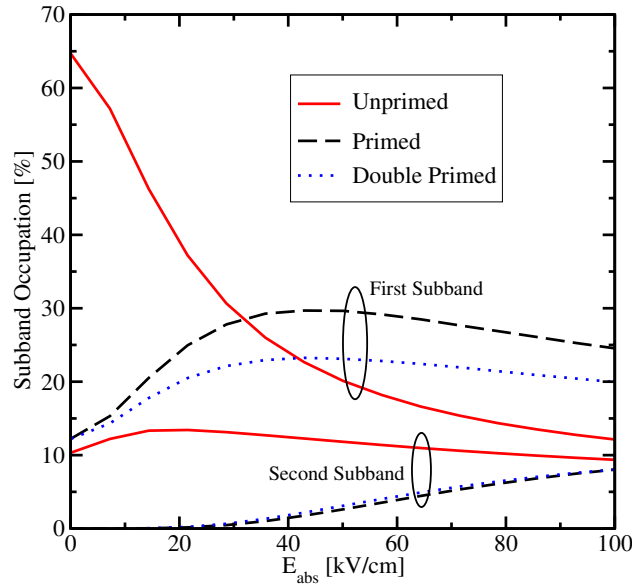


**Figure 2.9:** Populations of the first two subbands in the unprimed, primed, and double primed valleys versus lateral field in a UTB SOI MOSFET test device. Relative occupations are shifted to higher subbands in each valley for higher fields.

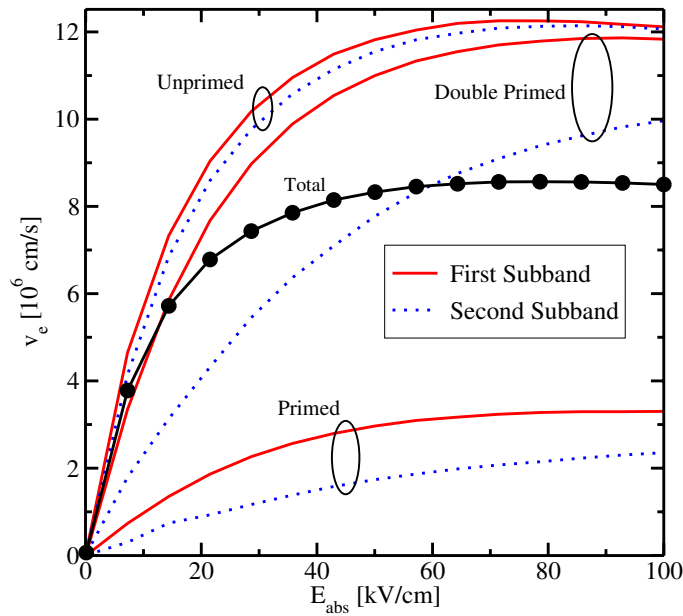


**Figure 2.10:** Velocities of the first and second subband of the unprimed, primed, and double primed valleys as well as the average total velocity versus lateral electric field.

allows to study the time evolution of a many-particle open quantum system. The many-particle information about the system is set into self-energies, which are parts of the equations of motion for the *Green's* functions. *Green's* functions can be calculated from perturbation theory [74]. The NEGF technique is a sophisticated method to determine the properties of a many-particle system both in thermodynamic equilibrium as well as in non-equilibrium situations. In the sequel, a description of the quantum transport method for the single particle model is given. For open systems with a coupling to a reservoir, the *Hamiltonian*, which describes the quantum system, can be expressed as [31, 75]

$$\begin{pmatrix} \mathcal{H} & \sigma \\ \sigma^\dagger & \mathcal{H}_R \end{pmatrix}, \quad (2.45)$$

with  $\mathcal{H}$  and  $\mathcal{H}_R$  as the *Hamilton* operators of the contact and the channel respectively, and  $\sigma$  denoting the coupling matrix. Hence, the *Schrödinger* equation of the channel–contact system can be written as [76]

$$\mathcal{E} \begin{pmatrix} \psi \\ \phi \end{pmatrix} = \begin{pmatrix} \mathcal{H} & \sigma \\ \sigma^\dagger & \mathcal{H}_R \end{pmatrix} \begin{pmatrix} \psi \\ \phi \end{pmatrix}. \quad (2.46)$$

Here,  $\psi$  and  $\phi$  are the wavefunctions of the channel and the contact, respectively. The *Green's* function equation is defined as

$$(\hat{\mathcal{I}}\mathcal{E} - \mathcal{H})G = \hat{\mathcal{I}} \quad (2.47)$$

and therefore the corresponding *Green's* function to (2.46) can be expressed as [31]

$$\begin{pmatrix} G & G_{dR} \\ G_{Rd} & G_{RR} \end{pmatrix} = \begin{pmatrix} \mathcal{E}\hat{\mathcal{I}} - \mathcal{H} & -\sigma \\ -\sigma^\dagger & \mathcal{E}\hat{\mathcal{I}} - \mathcal{H}_R \end{pmatrix}^{-1}, \quad (2.48)$$

where  $G_{dR}$  and  $G_{Rd}$  describe the coupling between device and the reservoir, whereas  $G_{RR}$  is the *Green's* function of the reservoir itself. The retarded *Green's* function  $G$  can be written as

$$G = (\mathcal{E}\hat{\mathcal{I}} - \mathcal{H} - \Sigma(\mathcal{E}))^{-1}. \quad (2.49)$$

$\Sigma$  is the energy dependent self-energy and describes the interaction between the device and the reservoir [77–79]. Thus, the advantage of the self-energy is that it reduces the *Green's* function of the reservoir to the dimension of the device *Hamiltonian*. The self-energy can be obtained as

$$\Sigma = \sigma G \sigma^\dagger, \quad (2.50)$$

and is usually determined iteratively. The spectral function  $A$  can be written as

$$A = i(G(\mathcal{E}) - G^\dagger(\mathcal{E})). \quad (2.51)$$

$A/2\pi$  is the matrix form of the density of states  $D(\mathcal{E})$ . Finally, the density matrix can be expressed as

$$\rho = \frac{1}{2\pi} \int_0^\infty f(\mathcal{E} - \mathcal{E}_f) A(\mathcal{E}) d\mathcal{E}, \quad (2.52)$$

which provides the charge distribution in the channel.  $f$  is the *Fermi* distribution function as explained in Section 2.1.3.1 and  $\mathcal{E}_f$  is the *Fermi* energy.

Assuming that the device is being connected to two contacts with different *Fermi* energies and hence also different *Fermi* functions, the current in the ballistic regime can be obtained as [78]

$$I = -\frac{2q}{h} \int_0^{\infty} T(\mathcal{E}) d\mathcal{E} (f(\mathcal{E}_{f1}) - f(\mathcal{E}_{f2})). \quad (2.53)$$

$T(\mathcal{E})$  is the transmission coefficient indicating the probability, that an electron with the energy  $\mathcal{E}$  can travel from the source to the drain and is defined as

$$T(\mathcal{E}) = \text{tr}(\Gamma_1 A_2) = \text{tr}(\Gamma_2 A_1) \quad (2.54)$$

with

$$\Gamma_{1,2} = i \left( \Sigma_{1,2} - \Sigma_{1,2}^\dagger \right) \quad (2.55)$$

as the coupling of the channel to the reservoir.

### 2.3.2 Wigner Monte Carlo

The MC technique is a well established and accurate numerical method to solve the BTE. Due to the similarities between the *Wigner* equation written as [80, 81]

$$\partial_t f_w - \nabla_{\mathbf{p}} \mathcal{H} \nabla_{\mathbf{r}} f_w - q(E - \nabla_{\mathbf{r}} V_w(\mathbf{r})) \nabla_{\mathbf{p}} f_w = Q_{\text{coll}}(f_w) \quad (2.56)$$

and the BTE (see equation (2.28)), it is tempting to solve the *Wigner* equation with the MC technique [33, 82, 83] as well.  $V_w(\mathbf{r})$  denotes an external *Wigner* potential. The *Wigner* function  $f_w$  can be derived from the density matrix expressed by the *Liouville von Neumann* equation using the *Wigner–Weyl* transformation [84]. With the *Fourier* transformation of the product of wavefunctions at two points [85], the *Wigner* function can be expressed as

$$f_w(\mathbf{r}, \mathbf{k}, t) = \frac{1}{\pi^3} \int_{-\infty}^{\infty} \psi(\mathbf{r} - \mathbf{r}', t) d\mathbf{r} \psi^*(\mathbf{r} + \mathbf{r}', t) e^{2i\mathbf{r}'\mathbf{k}}. \quad (2.57)$$

The *Wigner* function is a quantum mechanical description in phase-space, which is, however no longer positive definite. Hence, it cannot be regarded as a distribution function directly, but observables need to be derived from it. In the literature this is known as the negative-sign problem [86, 87].

An important feature of this so called phase-space approach is the ability of expressing quantum-mechanical expectation values in the same way as it is done in classical statistical mechanics. Furthermore, the *Wigner* equation can be used as a base for quantum macroscopic transport models as the quantum drift-diffusion or the quantum hydrodynamic model using the method of moments.

### 2.3.3 Quantum Macroscopic Models

Quantum macroscopic models can be derived from a fluid dynamical view using the *Madelung* transformation for the wave function  $\psi$  defined as [39]

$$\psi = \sqrt{n} \exp\left(\frac{imS}{\hbar}\right), \quad (2.58)$$

The *Madelung* transformation states that the wave function can be decomposed in its amplitude  $\sqrt{n}$  and phase  $S$ , whereby the amplitude is defined as the square root of the particle density.  $i$  is referred here to the complex number  $\sqrt{-1}$ , whereas  $m$  denotes the carrier mass. Since the electron density of a single state is defined as [39]

$$n_i = |\psi_i|^2, \quad (2.59)$$

and the density is by definition positive, the *Madelung* transformation makes only sense as long as  $n > 0$  is valid [53].

Quantum macroscopic models can be derived from the *Wigner* equation as well using the method of moments. Since macroscopic transport models based on the BTE are derived using the method of moments (see Section 2.4.1), only the derivation of quantum macroscopic models using the *Madelung* transformation is pointed out here. Inserting equation (2.58) into equation (2.11), the current density  $\mathbf{J}$  can be written as

$$\mathbf{J} = -qn\nabla_r S. \quad (2.60)$$

The phase  $S$  of equation (2.58) can be interpreted as a velocity potential. Inserting equation (2.58) into the *Schrödinger* equation (2.7) yields

$$i\hbar\partial_t \left( \sqrt{n} \exp\left(\frac{imS}{\hbar}\right) \right) = -\frac{\hbar^2}{2m} \nabla^2 \left( \sqrt{n} \exp\left(\frac{imS}{\hbar}\right) \right) - qV(\mathbf{r}) \left( \sqrt{n} \exp\left(\frac{imS}{\hbar}\right) \right).$$

Dividing equation (2.61) with  $\exp\left(\frac{imS}{\hbar}\right)$  leads to

$$i\hbar \left( \partial_t(\sqrt{n}) + \sqrt{n} \left( \frac{im}{\hbar} \right) \partial_t S \right) = -\frac{\hbar^2}{2m} \left( \nabla^2 \sqrt{n} + \frac{2im}{\hbar} \nabla_r \sqrt{n} \nabla_r S - \frac{m^2}{\hbar^2} \sqrt{n} (\nabla_r S)^2 \right. \\ \left. + \frac{im}{\hbar} \sqrt{n} \nabla^2 S \right) - qV(\mathbf{r})\sqrt{n}. \quad (2.61)$$

With the imaginary part, one can obtain the particle conservation equation as

$$\partial_t n = -2\sqrt{n} \nabla_r \cdot (\sqrt{n} \nabla_r S) - n \nabla^2 S = -\nabla_r \cdot (n \nabla_r S) = -\frac{1}{q} \nabla_r \cdot \mathbf{J}, \quad (2.62)$$

$$\partial_t n + \frac{1}{q} \nabla_r \cdot \mathbf{J} = 0. \quad (2.63)$$

The real part yields

$$\partial_t S = \frac{\hbar^2}{2m^2} \frac{\nabla^2 \sqrt{n}}{\sqrt{n}} - \frac{1}{2} (\nabla_r S)^2 + \frac{q}{m} V(\mathbf{r}). \quad (2.64)$$

With the gradient and a multiplication of (2.64) with  $-qn$ , one obtains the quantum conservation equation of the current

$$\partial_t \mathbf{J} - \frac{1}{q} \nabla_r \left( \frac{\mathbf{J} \otimes \mathbf{J}}{n} \right) + \frac{q^2}{m} n \nabla_r V(\mathbf{r}) + \frac{\hbar^2 q}{2m^2} n \nabla_r \left( \frac{\nabla^2 \sqrt{n}}{\sqrt{n}} \right) = 0. \quad (2.65)$$

Equations (2.63) and (2.65) are referred to as the quantum hydrodynamic equations [39]. With “ $\hbar \rightarrow 0$ ”, the quantum conservation equation (2.65) turns into the classical current conservation equation. The advantage of this method is that in two or three space dimensions fluid-dynamical models are numerical cheaper compared to the *Schrödinger* equation. Furthermore, boundary conditions can be more easily applied compared to the *Schrödinger* formulation. However, the dispersive character of the quantum hydrodynamic transport system implies that the solution may develop high frequency oscillations, which are localized in regions not a priori known. Therefore, the numerical simulations with quantum hydrodynamic models require an extremely high number of grid points, which leads to unnecessarily time consuming computations [88].

### 2.3.4 Quantum Correction Models

Since transport parameters as for instance the carrier mobility of modern semiconductor devices are strongly influenced by quantum mechanical effects, it is essential to take quantum correction models within classical simulations into account. Several quantum correction models based on different approaches have been proposed, which influence the electrostatics of the system.

The quantum correction model *modified local density approximation* (MLDA) [89] is based on a local correction of the effective density of states  $N_c$  near the gate oxide as

$$N_c = N_{c,0} \left( 1 - \exp \left( - \frac{(z + z_0)^2}{\chi^2 \lambda_{\text{thermal}}^2} \right) \right) \quad \text{with} \quad \lambda_{\text{thermal}} = \frac{\hbar}{\sqrt{2mk_B T}}. \quad (2.66)$$

$N_{c,0}$  is here the classical effective density of states with  $\chi$  as a fitting parameter.  $z$  is the distance from the interface,  $z_0$  is the tunneling distance, and  $\lambda_{\text{thermal}}$  denotes the thermal wavelength. The correction term of equation (2.66) can be calculated from the quantum mechanical expression of the particle density as stated in [90]. The advantage of the MLDA procedure is that no solution variable is used in the correction term. Therefore, the model can be implemented as a preprocessing step and has only a minor impact on the overall CPU time [91]. However, this approach is based on the field-free *Schrödinger* equation. The method loses its validity for high-fields. An improved MLDA technique has been suggested in [92, 93]. A heuristic wavelength parameter has been introduced as

$$\lambda'_{\text{thermal}}(z, N_{\text{eff}}, T) = \chi(z, N_{\text{eff}}, T) \lambda_{\text{thermal}}(T), \quad (2.67)$$

where  $N_{\text{eff}}$  is defined as the net doping  $N_{\text{eff}} = N_a - N_d$  with  $\chi(z, N_{\text{eff}}, T)$  as a fit factor. As pointed out in [92], the improved MLDA can now cover the important case of high fields perpendicular to the interface. The fit parameters have been matched with the results of a self-consistent *Schrödinger–Poisson* solver. The model is calibrated for bulk MOSFET structures. However, the MLDA method is only valid for devices with one oxide. Therefore, a characterization of quantization in DG MOSFETs is not possible.



A quantum correction technique to cover such devices is presented in [94]. The idea behind this model is as follows: The strong quantization perpendicular to the interface can be well approximated with an infinite square well potential. The eigenstates within the quantization region are estimated using an analytical approach. This assumption allows to determine a quantum correction potential which modifies the band edge to reproduce the quantum mechanical carrier concentration.

In [95], the correction is carried out by a better modeling of the conduction band edge as

$$\mathcal{E}_c = \mathcal{E}_{\text{class}} + \frac{13}{9} F(z) \Delta\mathcal{E}_g \quad \text{with} \quad \Delta\mathcal{E}_g \approx \beta \left( \frac{\kappa_{\text{Si}}}{4qk_{\text{B}}T} \right)^{1/3} |E_{\perp}|^{2/3}. \quad (2.68)$$

$\mathcal{E}_{\text{class}}$  is the classical band edge energy, the correction  $F$  is a function of the distance to the interface, and  $E_{\perp}$  is the electric field perpendicular to the interface. The value of the proportionality factor can be determined from the shift of the long-channel threshold voltage as explained in [95].

Fig. 2.11 shows the electron concentration calculated for a single gate SOI MOSFET classically, quantum mechanically, and with the quantum correction models MLDA, the model after [95], and the *improved modified local density approximation* (IMLDA) [92]. A gate voltage of 1 V has been applied, and the quantum electron concentration has been calculated using a *Schrödinger–Poisson* solver [2]. As can be observed, the electron concentration obtained from the IMLDA model fit the quantum mechanical simulation quite well compared to the other approaches. Therefore, the IMLDA model is used in this work to cover quantum effects in the classical device simulations.

## 2.4 Semi-Classical Transport

The main focus of this work is set on macroscopic transport models based on the BTE. First, the method to derive higher-order macroscopic models is described followed by a detailed derivation. Since the models must be benchmarked to other solution techniques of the BTE [96,97], a short introduction of the *Monte Carlo* method and the *Spherical Harmonics Expansion* approach is presented.

### 2.4.1 Method of Moments

On an engineering level, a very efficient way to find approximate solutions of the BTE is the method of moments. In order to formulate a set of balance and flux equations coupled with *Poisson's* equation, one has to multiply the BTE with a set of weight functions and integrate over  $\mathbf{k}$ -space.

An arbitrary number of equations can be derived, each containing information from the next-higher equation. Hence, there exists more moments than equations. Therefore, one has to truncate this equation hierarchy in order to get a fully defined equation-system. The assumption to close the system and to express the highest moment with the lower moments is called closure relation. The closure relation estimates the information of the higher-order moments and thus determines the accuracy of the system. For instance, in the case of the drift-diffusion model,

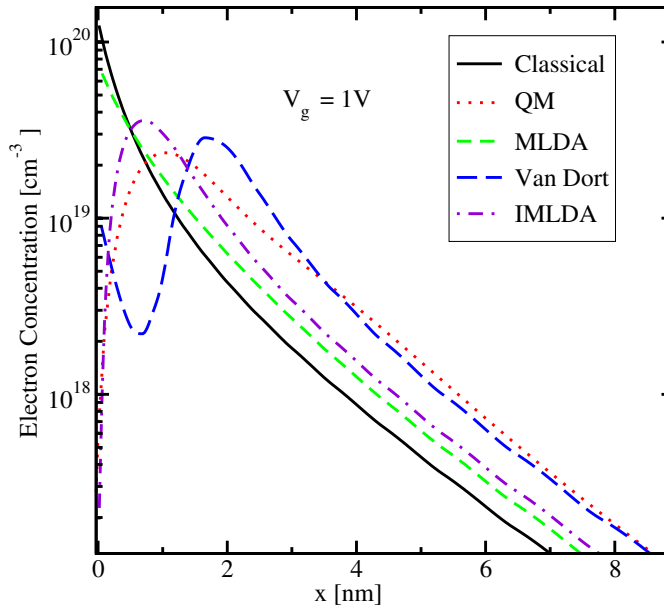


**Figure 2.11:** The electron concentration of a single gate SOI MOSFET has been calculated classically, quantum-mechanically, together with the quantum correction models MLDA, *Van Dort*, and the improved MLDA (after [3]).

the electrons are assumed to be in thermal equilibrium ( $T_n = T_L$ ) with the lattice [1]. There exist several theoretical approaches to cover the closure problem [98], like the maximum entropy principle [99–101] in the sense of extended thermodynamics.

The idea of the maximum entropy principle is that a large number of collisions is necessary to relax the carrier energies to their equilibrium, while the momentum, heat flow, and anisotropic stresses relax within a shorter time. Therefore, an intermediate state arises, where the fluid is in its own thermal equilibrium. This can be called *partial thermal equilibrium*. All transport parameters are zero except for the carrier temperature  $T_n$ . Another important assumption is that the entropy density and the entropy flux do not depend on the relative velocity of the electron gas. With the *partial thermal equilibrium*, closure relations can be found which are exactly those obtained with a shifted *Maxwellian*. A heated *Maxwellian* is used here as a closure for the hydrodynamic transport model and by the introduction of the kurtosis, the six moments model will be closed. A detailed description is given in the sequel.

To get physically reasonable equations, the weight functions are chosen as the powers of increasing orders of the momentum. The moments in one, two, and three dimensions, respectively, are defined as

$$x_{jd}(\mathbf{r}_d) = \frac{2}{(2\pi)^d} \int_{-\infty}^{\infty} X_{jd}(\mathbf{r}_d, \mathbf{k}_d) f_d(\mathbf{r}_d, \mathbf{k}_d, t) d^d k = n \langle X_{jd}(\mathbf{k}_d) \rangle = \langle\langle X_{jd}(\mathbf{k}_d) \rangle\rangle. \quad (2.69)$$

$x_j(\mathbf{r})$  denotes the macroscopic values together with the microscopic counterpart  $X_j(\mathbf{k})$ , where  $f_d(\mathbf{r}_d, \mathbf{k}_d, t)$  is the time dependent distribution function in the six-dimensional phase space.

$d$  is linked to the one, two, and three-dimensional electron gas ( $d = 1$ ,  $d = 2$ , or  $d = 3$ ), whereas  $n$  represents the carrier density.

For the sake of clarity, during the derivation of macroscopic transport models the dimension indices are neglected. Multiplying the BTE with the even scalar-valued weights  $X = X(\mathbf{r}, \mathbf{k})$  and integrating over  $\mathbf{k}$ -space

$$\int X \partial_t f \, d^3 \mathbf{k} + \int X \mathbf{v} \nabla_{\mathbf{r}} f \, d^3 \mathbf{k} + \int X \mathbf{F} \nabla_{\mathbf{p}} f \, d^3 \mathbf{k} = \langle\langle \partial_t X \rangle\rangle_{\text{coll}}, \quad (2.70)$$

yields the general conservation equations. In the following derivations, the distribution  $f(\mathbf{r}, \mathbf{k}, t)$ , the group velocity  $\mathbf{v}(\mathbf{k}, \mathbf{r})$ , and the generalized force  $\mathbf{F}(\mathbf{k}, \mathbf{r})$  are denoted as  $f, \mathbf{v}$ , and  $\mathbf{F}$ .

The first term on the left side of equation (2.70) leads to

$$\int X \partial_t f \, d^3 \mathbf{k} = \partial_t \int X f \, d^3 \mathbf{k} = \partial_t \langle\langle X \rangle\rangle, \quad (2.71)$$

whereas the second term yields

$$\int X \mathbf{v} \nabla_{\mathbf{r}} f \, d^3 \mathbf{k} = \int \nabla_{\mathbf{r}} (X \mathbf{v} f) \, d^3 \mathbf{k} - \int X f \nabla_{\mathbf{r}} \mathbf{v} \, d^3 \mathbf{k} - \int \mathbf{v} f \nabla_{\mathbf{r}} X \, d^3 \mathbf{k} \quad (2.72)$$

and the third term

$$\int X \mathbf{F} \nabla_{\mathbf{p}} f \, d^3 \mathbf{k} = \int \nabla_{\mathbf{p}} (X \mathbf{F} f) \, d^3 \mathbf{k} - \int X \nabla_{\mathbf{p}} \mathbf{F} f \, d^3 \mathbf{k} - \int \mathbf{F} \nabla_{\mathbf{p}} X f \, d^3 \mathbf{k}. \quad (2.73)$$

Using Gauss' theorem and assuming that all surface integrals over the border of the Brillouin-Zone are equal to zero [102], the first term on the right side of equation (2.73) vanishes. Inserting  $\mathbf{F} = -\nabla_{\mathbf{r}} \mathcal{H}$  and  $\mathbf{v} = \nabla_{\mathbf{p}} \mathcal{H}$  with the Hamilton function  $\mathcal{H}$  given as

$$\mathcal{H} = \pm \mathcal{E}_{c,v}(\mathbf{r}) + s_{\alpha} q \varphi + \mathcal{E}(\mathbf{k}, \mathbf{r}) = \mathcal{E}(\mathbf{k}, \mathbf{r}) + s_{\alpha} q \tilde{\varphi}(\mathbf{r}), \quad (2.74)$$

with  $s_{\alpha} = -1$  for electrons and  $s_{\alpha} = 1$  for holes, into equation (2.72) and (2.73) respectively, leads to the BTE expressed by the averages of the even scalar-valued moment

$$\partial_t \langle\langle X \rangle\rangle + \nabla_{\mathbf{r}} \langle\langle \mathbf{v} X \rangle\rangle - \langle\langle \mathbf{v} \nabla_{\mathbf{r}} X \rangle\rangle - \langle\langle \mathbf{F} \nabla_{\mathbf{p}} X \rangle\rangle = \langle\langle \partial_t X \rangle\rangle_{\text{coll}}. \quad (2.75)$$

Finally, the equation reads

$$\partial_t \langle\langle X \rangle\rangle + \nabla_{\mathbf{r}} \langle\langle \mathbf{v} X \rangle\rangle - \langle\langle \mathbf{v} \nabla_{\mathbf{r}} X \rangle\rangle + \langle\langle \nabla_{\mathbf{r}} \mathcal{E} \nabla_{\mathbf{p}} X \rangle\rangle + s_{\alpha} q \langle\langle \nabla_{\mathbf{p}} X \rangle\rangle \nabla_{\mathbf{r}} \tilde{\varphi} = \langle\langle \partial_t X \rangle\rangle_{\text{coll}}. \quad (2.76)$$

Furthermore, the BTE for the odd vector-valued moments can be transformed analogously

$$\begin{aligned} \partial_t \langle\langle \mathbf{X} \rangle\rangle + \nabla_{\mathbf{r}} \langle\langle \mathbf{v} \otimes \mathbf{X} \rangle\rangle - \langle\langle \mathbf{v} \nabla_{\mathbf{r}} \otimes \mathbf{X} \rangle\rangle + \langle\langle \nabla_{\mathbf{r}} \mathcal{E} \nabla_{\mathbf{p}} \otimes \mathbf{X} \rangle\rangle + s_{\alpha} q \langle\langle \nabla_{\mathbf{p}} \otimes \mathbf{X} \rangle\rangle \nabla_{\mathbf{r}} \tilde{\varphi} \\ = \langle\langle \partial_t \mathbf{X} \rangle\rangle_{\text{coll}}. \end{aligned} \quad (2.77)$$

Equations (2.76) and (2.77) are the starting points for the derivations of the conservation equations and fluxes of macroscopic transport models.

### 2.4.2 Modeling of the Scattering Operator

In order to get an analytical expression for the right hand side of equations (2.76) and (2.77) several approaches have been suggested in [16, 103]. In this work, the macroscopic relaxation time approximation after *Bløtebjerg* [104] is used to approximate the scattering operator of the BTE

$$\langle\langle \partial_t X \rangle\rangle_{\text{coll}} = -\frac{\langle\langle X \rangle\rangle - \langle\langle X_0 \rangle\rangle}{\tau_X(f)}. \quad (2.78)$$

$\tau_X(f)$  is the macroscopic relaxation time for the weight function  $X$ .  $\langle\langle X_0 \rangle\rangle$  is the average weight function in equilibrium. Since the relaxation time  $\tau_X(f)$  depends on the distribution function, equation (2.78) is not an approximation. With

$$\tau_X \neq \tau_X(f) \quad (2.79)$$

equation (2.78) turns into the macroscopic relaxation time approximation. Therefore, the relaxation times depends only on the moments of the distribution function. For the odd moments, the approximation yields

$$\langle\langle \partial_t \mathbf{X} \rangle\rangle_{\text{coll}} \approx -\frac{\langle\langle \mathbf{X} \rangle\rangle - \langle\langle \mathbf{X}_0 \rangle\rangle}{\tau_{\text{odd}}} = -\frac{\mathbf{x}}{\tau_{\text{odd}}}, \quad (2.80)$$

and for the even moments one obtains

$$\langle\langle \partial_t X \rangle\rangle_{\text{coll}} \approx -\frac{\langle\langle X \rangle\rangle - \langle\langle X_0 \rangle\rangle}{\tau_{\text{even}}} = -\frac{x - x_0}{\tau_{\text{even}}}. \quad (2.81)$$

The subscript odd and even is linked to whether the moment is even or odd.

### 2.4.3 Macroscopic Transport Models

A hierarchy of macroscopic transport models based on the equations (2.76) and (2.77) can be derived using the method of moments described above [105]. The first three even scalar valued moments are defined as the powers of the energy  $\mathcal{E}(\mathbf{r}, \mathbf{k})$

$$X^{\text{even}} = (\mathcal{E}^0, \mathcal{E}^1, \mathcal{E}^2), \quad (2.82)$$

and the first three odd vector valued moments are defined as

$$X^{\text{odd}} = (\mathbf{p}\mathcal{E}^0, \mathbf{p}\mathcal{E}^1, \mathbf{p}\mathcal{E}^2). \quad (2.83)$$

In order to obtain the particle balance equation and the current equation, one has to insert the zeroth moment  $\mathcal{E}^0$  and the first moment  $\mathbf{p}\mathcal{E}^0$  into equation (2.76) and (2.77), respectively. While in the particle balance equation the particle current remains as an unknown variable, the particle current equation comprises the average kinetic energy. With a heated *Maxwellian* and the diffusion approximation the powers of the average energy assuming a parabolic band structure can be expressed by the carrier temperature as

$$\langle\langle \mathcal{E}^i \rangle\rangle^{1D} = \frac{(2i-1)!!}{2^i} (k_B T_n)^i, \quad \langle\langle \mathcal{E}^i \rangle\rangle^{2D} = i! (k_B T_n)^i, \quad \text{and} \quad \langle\langle \mathcal{E}^i \rangle\rangle^{3D} = \frac{(2i+1)!!}{2^i} (k_B T_n)^i \quad (2.84)$$

for the one, two, and three-dimensional electron gas, respectively. For instance, the average energy ( $i = 1$ ) for the 3D case can be written as

$$\langle\langle \mathcal{E} \rangle\rangle = \frac{3}{2} k_B T_n. \quad (2.85)$$

The drift-diffusion model is closed by the assumption of local thermal equilibrium, thus the carrier temperatures are set to the lattice temperature. The energy balance equation is introduced taking the second moment  $\mathcal{E}$  into account, where the energy flux remains as an unknown term. The third moment  $\mathbf{v}\mathcal{E}$  describes exactly this energy flux. The transport model considering these first four moment equations is called the hydrodynamic transport model [4]. By considering additional moments  $\mathcal{E}^2$  and  $\mathbf{p}\mathcal{E}^2$ , leads to the second-order temperature balance equation and to the second-order temperature flux. The so called six moments model is closed by introducing the kurtosis  $\beta$  describing the deviation of the current distribution function from the *Maxwell* distribution function [106].

The assumptions made during the derivation of the transport model are specified as follow:

- Non-parabolic band structure
- Product ansatz for the kinetic energy
- Isotropic band structure
- Tensor valued parameters are approximated by their traces
- Macroscopic relaxation time approximation
- Diffusion approximation
- Homogeneous materials

Furthermore, the averages of the microscopic quantities are defined as  $w_i = \langle \mathcal{E}^i \rangle$  and  $\mathbf{V}_i = \langle \mathbf{v}\mathcal{E}^i \rangle$ . In the case of the six moments model,  $i$  is defined in the range  $i \in [0, 2]$ . A detailed derivation and discussion of these models follows in the next section. An important objective here is to point out the model limitations.

### 2.4.3.1 Drift-Diffusion Transport Model

Inserting the zeroth moment into equation (2.76) yields the particle balance equation

$$\underbrace{\partial_t \langle\langle \mathcal{E}^0 \rangle\rangle}_{(1)} + \underbrace{\nabla_{\mathbf{r}} \langle\langle \mathbf{v}\mathcal{E}^0 \rangle\rangle}_{(2)} - \underbrace{\langle\langle \mathbf{v}\nabla_{\mathbf{r}}\mathcal{E}^0 \rangle\rangle}_{(3)} + \underbrace{\langle\langle \nabla_{\mathbf{r}}\mathcal{E}\nabla_{\mathbf{p}}\mathcal{E}^0 \rangle\rangle}_{(4)} + \underbrace{s_{\alpha q} \langle\langle \nabla_{\mathbf{p}}\mathcal{E}^0 \rangle\rangle \nabla_{\mathbf{p}}\tilde{\varphi}}_{(5)} = -R. \quad (2.86)$$

Since  $\mathcal{E}^0$  depends neither on  $\mathbf{r}$  or  $\mathbf{p}$ , one can omit the third, the fourth, and the fifth term of equation (2.86) to obtain

$$\partial_t (nw_0) + \nabla_{\mathbf{r}} (n\mathbf{V}_0) = -R. \quad (2.87)$$

Inserting the first moment  $\mathbf{p}\mathcal{E}^0$  into equation (2.77), the particle flux is obtained. The time derivation terms of the fluxes are neglected, since the relaxation time is in the order of picoseconds, which ensures quasi-stationary behavior even for today's fastest signals [20, 107].

$$\underbrace{\nabla_{\mathbf{r}}\langle\langle\mathbf{v}\otimes\mathbf{p}\mathcal{E}^0\rangle\rangle}_{(1)} - \underbrace{\langle\langle\mathbf{v}\nabla_{\mathbf{r}}\otimes\mathbf{p}\mathcal{E}^0\rangle\rangle}_{(2)} + \underbrace{\langle\langle\nabla_{\mathbf{r}}\mathcal{E}\nabla_{\mathbf{p}}\otimes\mathbf{p}\mathcal{E}^0\rangle\rangle}_{(3)} + \underbrace{s_{\alpha}q\langle\langle\nabla_{\mathbf{p}}\otimes\mathbf{p}\mathcal{E}^0\rangle\rangle\nabla_{\mathbf{r}}\tilde{\varphi}}_{(4)} = -\frac{\langle\langle\mathbf{p}\mathcal{E}^0\rangle\rangle}{\tau_0}, \quad (2.88)$$

where  $\tau_0$  is the momentum relaxation time. Due to the assumption of an isotropic band structure and in the diffusion limit, the non-diagonal elements of the tensors of equation (2.88) vanish. Hence, the tensor of the first part (1) of equation (2.88) can be approximated as the trace divided by the dimension factors of the system. Multiplying (1) with tensorial non-parabolicity factors  $H_i$ , one obtains

$$\nabla_{\mathbf{r}}\langle\langle\mathbf{v}\otimes\mathbf{p}\mathcal{E}^0\rangle\rangle \approx \frac{1}{d}\nabla_{\mathbf{r}}\langle\langle\text{tr}(\mathbf{v}\otimes\mathbf{p})\hat{\mathbf{I}}\rangle\rangle = AH_1\nabla_{\mathbf{r}}(nw_1) \quad (2.89)$$

with  $A$  as a dimension factor.  $A$  can be calculated considering the dimension of the system and the prefactors of the average energy assuming a parabolic bandstructure and a *Maxwell* distribution function. For instance, in the case of the three-dimensional electron gas the value of  $A$  can be derived as

$$\langle\langle\mathbf{v}\otimes\mathbf{p}\mathcal{E}^0\rangle\rangle \approx \frac{1}{3}\langle\langle\text{tr}(\mathbf{v}\otimes\mathbf{p})\hat{\mathbf{I}}\rangle\rangle = \frac{2}{3}H_1\frac{3}{2}nk_{\text{B}}T_n. \quad (2.90)$$

$A$  is equal to  $2/3$ . The average energy has been considered according to equation (2.85). For the one and two-dimensional electron gas the values are  $A_1 = 2$  and  $A_2 = 1$ , respectively. In the sequel, the non-parabolic factors will be shown using Subband Monte Carlo (SMC) data for the two-dimensional electron gas.  $m_{n,p}^*$  represents the effective masses for electrons and holes respectively.

Based on the second assumption that the kinetic energy can be expressed using a product ansatz

$$\mathcal{E} = \nu\kappa(\mathbf{k}), \quad (2.91)$$

term (2) and (3) of (2.88) vanish. The fourth term of (2.88) can be written as

$$s_{\alpha}q\langle\langle\nabla_{\mathbf{p}}\otimes\mathbf{p}\rangle\rangle\nabla_{\mathbf{r}}\tilde{\varphi} \approx s_{\alpha}nqw_0\nabla_{\mathbf{r}}\tilde{\varphi}. \quad (2.92)$$

Putting all terms together, the particle flux equation yields

$$n\mathbf{V}_0 = -\frac{\mu_0}{q}H_1A\nabla_{\mathbf{r}}(nw_1) - s_{\alpha}n\mu_0w_0\nabla_{\mathbf{r}}\tilde{\varphi}. \quad (2.93)$$

There, the carrier mobility  $\mu_0$  is defined as  $\mu_0 = q\tau_0/m_{n,p}^*$ .

Together with *Poisson's* equation, the drift-diffusion (DD) model can be formulated as

$$\partial_t(nw_0) + \nabla_{\mathbf{r}}(n\mathbf{V}_0) = -R, \quad (2.94)$$

$$n\mathbf{V}_0 = -\frac{\mu_0}{q}H_1A\nabla_{\mathbf{r}}(nw_1) - s_{\alpha}n\mu_0w_0\nabla_{\mathbf{r}}\tilde{\varphi}. \quad (2.95)$$

As the closure relation, the *local thermal equilibrium approximation* has been assumed. The *local thermal equilibrium approximation* sets the carrier temperatures  $T_n$  equal to the lattice temperature  $T_L$ . Furthermore, with the assumption of a cold *Maxwell* distribution function, the highest moment  $w_1$  can be expressed as

$$w_1^{1D} = \frac{1}{2}k_B T_L, \quad w_1^{2D} = k_B T_L, \quad \text{and} \quad w_1^{3D} = \frac{3}{2}k_B T_L. \quad (2.96)$$

Due to the diffusion approximation the drift term of the average carrier energy is neglected.

### 2.4.3.2 Energy Transport Model

The Energy Transport (ET) model can be derived by inserting the first four moments  $\mathcal{E}^i$  and  $\mathbf{p}\mathcal{E}^i$  with  $i \in [0, 1]$  into equation (2.76) and (2.77), respectively. The energy balance equation can be obtained by the second moment  $\mathcal{E}$

$$\partial_t \langle \langle \mathcal{E} \rangle \rangle + \nabla_{\mathbf{r}} \langle \langle \mathbf{v} \mathcal{E} \rangle \rangle - \langle \langle \mathbf{v} \nabla_{\mathbf{r}} \mathcal{E} \rangle \rangle + \langle \langle \nabla_{\mathbf{r}} \mathcal{E} \nabla_{\mathbf{p}} \mathcal{E} \rangle \rangle + s_{\alpha} q \langle \langle \nabla_{\mathbf{p}} \mathcal{E} \rangle \rangle \nabla_{\mathbf{r}} \tilde{\varphi} = -n \frac{\langle \langle \mathcal{E} \rangle \rangle - \langle \langle \mathcal{E}_0 \rangle \rangle}{\tau_1}. \quad (2.97)$$

After a reformulation, equation (2.97) yields

$$\partial_t (n w_1) + \nabla_{\mathbf{r}} (n \mathbf{V}_1) + s_{\alpha} q n \mathbf{V}_0 \nabla_{\mathbf{r}} \tilde{\varphi} + n \frac{w_1 - w_{10}}{\tau_1} = 0. \quad (2.98)$$

$w_{10}$  is the equilibrium case of  $w_1$ , whereas  $\mathbf{V}_1$  is the energy flux, the next higher moment.  $\tau_1$  is known as the energy relaxation time. The energy flux can be derived inserting the third moment  $\mathbf{v}\mathcal{E}$  into equation (2.77)

$$\underbrace{\nabla_{\mathbf{r}} \langle \langle \mathbf{v} \otimes \mathbf{p} \mathcal{E} \rangle \rangle}_{(1)} - \underbrace{\langle \langle \mathbf{v} \nabla_{\mathbf{r}} \otimes \mathbf{p} \mathcal{E} \rangle \rangle}_{(2)} + \underbrace{\langle \langle \nabla_{\mathbf{r}} \mathcal{E} \nabla_{\mathbf{p}} \otimes \mathbf{p} \mathcal{E} \rangle \rangle}_{(3)} + \underbrace{s_{\alpha} q \langle \langle \nabla_{\mathbf{p}} \otimes \mathbf{p} \mathcal{E} \rangle \rangle \nabla_{\mathbf{r}} \tilde{\varphi}}_{(4)} = -\frac{\langle \langle \mathbf{p} \mathcal{E} \rangle \rangle}{\tau_3}. \quad (2.99)$$

The first term on the left side of equation (2.99) can be expressed as

$$\nabla_{\mathbf{r}} \langle \langle \mathbf{v} \otimes \mathbf{p} \mathcal{E} \rangle \rangle \approx \frac{1}{d} \nabla_{\mathbf{r}} \langle \langle \text{tr} (\mathbf{v} \otimes \mathbf{v} \mathcal{E}) \hat{\mathbf{I}} \rangle \rangle = A H_2 \nabla_{\mathbf{r}} (n w_2). \quad (2.100)$$

Using the tensorial identity  $\nabla_{\mathbf{x}} \otimes \mathbf{x} h(\mathbf{x}) = h(\mathbf{x}) \nabla_{\mathbf{x}} \otimes \mathbf{x} + \mathbf{x} \otimes \nabla_{\mathbf{x}} h(\mathbf{x})$ , the second term can be rewritten as

$$\langle \langle \mathbf{v} \nabla_{\mathbf{r}} \otimes \mathbf{p} \mathcal{E} \rangle \rangle = \langle \langle \mathbf{v} (\mathcal{E} \nabla_{\mathbf{r}} \otimes \mathbf{p} + \mathbf{p} \otimes \nabla_{\mathbf{r}} \mathcal{E}) \rangle \rangle, \quad (2.101)$$

and the third term as

$$\langle \langle \nabla_{\mathbf{r}} \mathcal{E} \nabla_{\mathbf{p}} \otimes \mathbf{p} \mathcal{E} \rangle \rangle = \langle \langle \nabla_{\mathbf{r}} \mathcal{E} (\mathcal{E} \nabla_{\mathbf{p}} \otimes \mathbf{p} + \mathbf{p} \otimes \nabla_{\mathbf{p}} \mathcal{E}) \rangle \rangle \approx \langle \langle \mathcal{E} \nabla_{\mathbf{r}} \mathcal{E} + \nabla_{\mathbf{r}} \mathcal{E} (\mathbf{p} \otimes \mathbf{v}) \rangle \rangle. \quad (2.102)$$

Combining equations (2.101) with (2.102) cancels each other. The fourth term on the left side of (2.99) can be approximated again with the above tensorial identity used in (2.100) as

$$s_{\alpha} q \langle \langle \nabla_{\mathbf{p}} \otimes \mathbf{p} \mathcal{E} \rangle \rangle \nabla_{\mathbf{r}} \tilde{\varphi} = s_{\alpha} q \langle \langle \mathcal{E} \nabla_{\mathbf{p}} \otimes \mathbf{p} + \mathbf{p} \otimes \nabla_{\mathbf{p}} \mathcal{E} \rangle \rangle \nabla_{\mathbf{r}} \tilde{\varphi} \quad (2.103)$$

$$= s_{\alpha} q n w_1 (1 + A H_1) \nabla_{\mathbf{r}} \tilde{\varphi}. \quad (2.104)$$

Collecting all terms together yields the energy flux

$$n\mathbf{V}_1 = -\frac{\mu_1}{q}H_2A\nabla_{\mathbf{r}}(nw_2) - s_\alpha n\mu_1(1 + AH_1)w_1\nabla_{\mathbf{r}}\tilde{\varphi}. \quad (2.105)$$

The energy flux mobility  $\mu_1$  is defined as  $\mu_1 = q\tau_3/m_{n,p}^*$ . Summarizing the derivation of the energy balance and the energy flux equation the ET transport model yields

$$\partial_t(nw_0) + \nabla_{\mathbf{r}}(n\mathbf{V}_0) = -R, \quad (2.106)$$

$$n\mathbf{V}_0 = -\frac{\mu_0}{q}H_1A\nabla_{\mathbf{r}}(nw_1) - s_\alpha n\mu_0w_0\nabla_{\mathbf{r}}\tilde{\varphi}, \quad (2.107)$$

$$\partial_t(nw_1) + \nabla_{\mathbf{r}}(n\mathbf{V}_1) + s_\alpha qn\mathbf{V}_0\nabla_{\mathbf{r}}\tilde{\varphi} + n\frac{w_1 - w_{10}}{\tau_1} = 0, \quad (2.108)$$

$$n\mathbf{V}_1 = -\frac{\mu_1}{q}H_2A\nabla_{\mathbf{r}}(nw_2) - s_\alpha n\mu_1(1 + AH_1)w_1\nabla_{\mathbf{r}}\tilde{\varphi}. \quad (2.109)$$

In order to close the system, a heated *Maxwellian* is assumed. The highest moment  $w_2$  for the one, two, and three-dimensional electron gas, respectively, can be written as

$$w_2^{1D} = \frac{3}{4}(k_B T_n)^2, \quad w_2^{2D} = 2(k_B T_n)^2, \quad \text{and} \quad w_2^{3D} = \frac{15}{4}(k_B T_n)^2. \quad (2.110)$$

Note that due to the diffusion approximation convective terms of the form  $\langle \mathbf{k} \rangle \otimes \langle \mathbf{k} \rangle$  and  $\langle \mathbf{k} \rangle \cdot \langle \mathbf{k} \rangle$  are neglected against terms of the form  $\langle \mathbf{k} \otimes \mathbf{k} \rangle$  and  $\langle \mathbf{k} \cdot \mathbf{k} \rangle$ . The consequence is that only the thermal energy  $k_B T_n$  is considered, whereas the drift energy term of the carrier energy is neglected.

### 2.4.3.3 Six Moments Transport Model

Adding the two next higher moments to the hydrodynamic transport model, the six moments (SM) transport model can be derived. Using the fourth moment  $\mathcal{E}^2$  in equation (2.76), the second-order energy balance equation is expressed as

$$\partial_t\langle\langle \mathcal{E}^2 \rangle\rangle + \nabla_{\mathbf{r}}\langle\langle \mathbf{v}\mathcal{E}^2 \rangle\rangle - \langle\langle \mathbf{v}\nabla_{\mathbf{r}}\mathcal{E}^2 \rangle\rangle + \langle\langle \nabla_{\mathbf{r}}\mathcal{E}\nabla_{\mathbf{p}}\mathcal{E}^2 \rangle\rangle + s_\alpha q\langle\langle \nabla_{\mathbf{p}}\mathcal{E}^2 \rangle\rangle\nabla_{\mathbf{r}}\tilde{\varphi} = -n\frac{\langle\langle \mathcal{E}^2 \rangle\rangle - \langle\langle \mathcal{E}_0^2 \rangle\rangle}{\tau_2}. \quad (2.111)$$

With  $\nabla_{\mathbf{r}}\mathcal{E}^2 = 2\mathcal{E}\nabla_{\mathbf{r}}\mathcal{E}$ , the second-order energy balance equation can be formulated as

$$\partial_t(nw_2) + \nabla_{\mathbf{r}}(n\mathbf{V}_2) - 2s_\alpha q\mathbf{V}_1\nabla_{\mathbf{r}}\tilde{\varphi} + n\frac{w_2 - w_{20}}{\tau_2} = 0. \quad (2.112)$$

The second-order energy flux equation can be obtained inserting the sixth moment  $\mathbf{v}\mathcal{E}^2$  into equation (2.77)

$$\underbrace{\nabla_{\mathbf{r}}\langle\langle \mathbf{v} \otimes \mathbf{p}\mathcal{E}^2 \rangle\rangle}_{(1)} - \underbrace{\langle\langle \mathbf{v}\nabla_{\mathbf{r}} \otimes \mathbf{p}\mathcal{E}^2 \rangle\rangle}_{(2)} + \underbrace{\langle\langle \nabla_{\mathbf{r}}\mathcal{E}\nabla_{\mathbf{p}} \otimes \mathbf{p}\mathcal{E}^2 \rangle\rangle}_{(3)} + \underbrace{s_\alpha q\langle\langle \nabla_{\mathbf{p}} \otimes \mathbf{p}\mathcal{E}^2 \rangle\rangle}_{(4)}\nabla_{\mathbf{r}}\tilde{\varphi} = -\frac{\mathbf{p}\mathcal{E}^2}{\tau_4}. \quad (2.113)$$



Each term on the left hand side of equation (2.113) is derived as in the case of the energy flux equation. The first term yields

$$\nabla_{\mathbf{r}} \langle \langle \mathbf{v} \otimes \mathbf{p} \mathcal{E}^2 \rangle \rangle \approx \frac{1}{d} \nabla_{\mathbf{r}} \langle \langle \text{tr} (\mathbf{v} \otimes \mathbf{p} \mathcal{E}^2) \hat{\mathbf{I}} \rangle \rangle = AH_3 \nabla_{\mathbf{r}} (nw_3), \quad (2.114)$$

while the second and the third term together can be neglected. The fourth term on the left-hand side of equation (2.113) yields

$$s_{\alpha} q \langle \langle \nabla_{\mathbf{p}} \otimes \mathbf{v} \mathcal{E}^2 \rangle \rangle \approx (1 + 2AH_2) nw_2 \nabla_{\mathbf{r}} \tilde{\varphi}. \quad (2.115)$$

Summarizing all contributions, the second-order energy flux can be written as

$$n \mathbf{V}_2 = -\frac{\mu_2}{q} H_3 A \nabla_{\mathbf{r}} (nw_3) - s_{\alpha} n \mu_2 (1 + 2AH_2) w_2 \nabla_{\mathbf{r}} \tilde{\varphi}. \quad (2.116)$$

The second-order energy flux mobility is defined as  $q\tau_4/m_{n,p}^*$ . The SM transport model can be now written as

$$\partial_t (nw_0) + \nabla_{\mathbf{r}} (n \mathbf{V}_0) = -R, \quad (2.117)$$

$$n \mathbf{V}_0 = -\frac{\mu_0}{q} H_1 A \nabla_{\mathbf{r}} (nw_1) - s_{\alpha} n \mu_0 w_0 \nabla_{\mathbf{r}} \tilde{\varphi}, \quad (2.118)$$

$$\partial_t (nw_1) + \nabla_{\mathbf{r}} (n \mathbf{V}_1) + s_{\alpha} q n \mathbf{V}_0 \nabla_{\mathbf{r}} \tilde{\varphi} + n \frac{w_1 - w_{10}}{\tau_1} = 0, \quad (2.119)$$

$$n \mathbf{V}_1 = -\frac{\mu_1}{q} H_2 A \nabla_{\mathbf{r}} (nw_2) - s_{\alpha} n \mu_1 (1 + AH_1) w_1 \nabla_{\mathbf{r}} \tilde{\varphi}, \quad (2.120)$$

$$\partial_t (nw_2) + \nabla_{\mathbf{r}} (n \mathbf{V}_2) + 2s_{\alpha} q \mathbf{V}_1 \nabla_{\mathbf{r}} \tilde{\varphi} + n \frac{w_2 - w_{20}}{\tau_2} = 0, \quad (2.121)$$

$$n \mathbf{V}_2 = -\frac{\mu_2}{q} H_3 A \nabla_{\mathbf{r}} (nw_3) - s_{\alpha} n \mu_2 (1 + 2AH_2) w_2 \nabla_{\mathbf{r}} \tilde{\varphi}. \quad (2.122)$$

In order to close the six moments model, the kurtosis, which is the deviation of the current distribution function from a heated *Maxwellian*, is introduced. For the one, two, and three-dimensional electron gas the kurtosis is defined as

$$\beta^{1D} = \frac{1}{3} \frac{w_2}{w_1^2}, \quad \beta^{2D} = \frac{1}{2} \frac{w_2}{w_1^2}, \quad \text{and} \quad \beta^{3D} = \frac{3}{5} \frac{w_2}{w_1^2}. \quad (2.123)$$

The factors 1/3, 1/2, and 3/5 in the 1D, 2D, and 3D case are normalization factors, respectively. For parabolic bands and a heated *Maxwellian* the kurtosis equals unity. In realistic devices the kurtosis is in the range [0.75, 3], which indicates a strong deviation from a heated *Maxwellian*. This is visualized in Fig. 2.12.

Here, the kurtosis of an  $n^+nn^+$  structure calculated with the 3D MC approach is shown. A driving field of 100 kV/cm in the middle of the channel has been applied. The kurtosis is

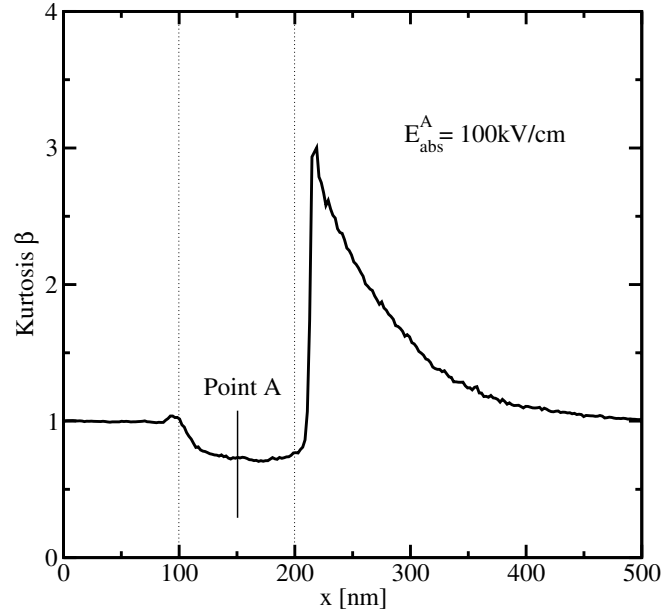


**Figure 2.12:** Kurtosis for a 100 nm  $n^+nn^+$  structure calculated with the MC method. In the channel the kurtosis is lower than one, which means that the heated *Maxwellian* overestimates the carrier distribution function, while the *Maxwellian* underestimates the carrier distribution in the drain.

equal to unity at the beginning of the device, which means that a heated *Maxwellian* is a good approximation for the carrier distribution function. In the channel the kurtosis is below unity. Therefore, the *Maxwellian* overestimates the carrier distribution function. In the drain region the carrier distribution function overestimates the *Maxwellian*. A detailed discussion about this deviation of the carrier distribution function from a *Maxwellian* is given in the next chapter. The closure relation for the six moments model can be finally written as

$$w_3^{1D} = \frac{15}{8} (k_B T_n)^3 \beta^c, \quad w_3^{2D} = 6 (k_B T_n)^3 \beta^c, \quad \text{and} \quad w_3^{3D} = \frac{105}{8} (k_B T_n)^3 \beta^c. \quad (2.124)$$

$c$  is a fit factor and it has been previously demonstrated [108, 109] that a value of 2.7 delivers good results for  $w_3$  in the source and in the channel regions. This is visible in the left part of Fig. 2.13. Here, the ratio between the sixth moment calculated with MC simulation and the analytical equations (2.124) for different  $c$  in a  $n^+nn^+$  structure is shown. As can be observed, a value of 2.7 provides the best result in the source and in the channel region, while the value 3.0 of  $c$  gives better results at the beginning of the drain region. Due to the better modeling of  $w_3$  with 2.7 in the source and in the channel region compared to  $c = 3.0$ , 2.7 is the exponent of choice.

On the right side of Fig. 2.13 the maximum peak of the ratio in point B (see the left part of Fig. 2.13) is shown as a function of the lattice temperature  $T_L$ . The maximum peak decreases, which means that the closure relation of the six moments model with  $c = 2.7$  is improved, especially in the drain region. The origin of this improvement for increasing  $T_L$  is a decrease of the high energy tail of the distribution function as pointed out in Fig. 2.14.

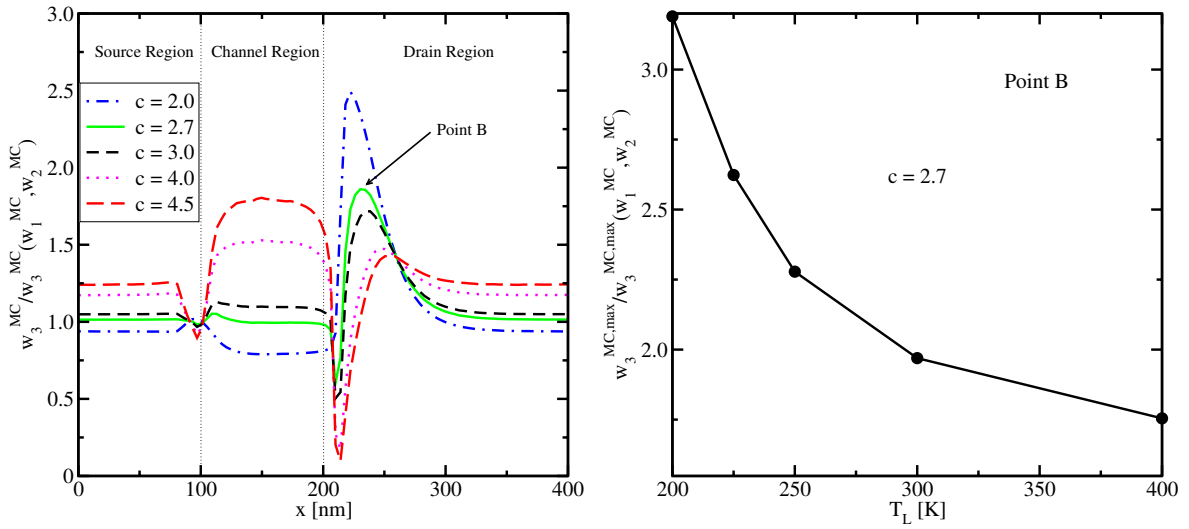


**Figure 2.13:** Ratio between the sixth moment obtained from three-dimensional bulk MC simulation and the analytical closure relation (2.124) of the six moments model for different values of  $c$  (see left part). The maximum peak at point B of the ratio as a function of the lattice temperature is shown on the right.

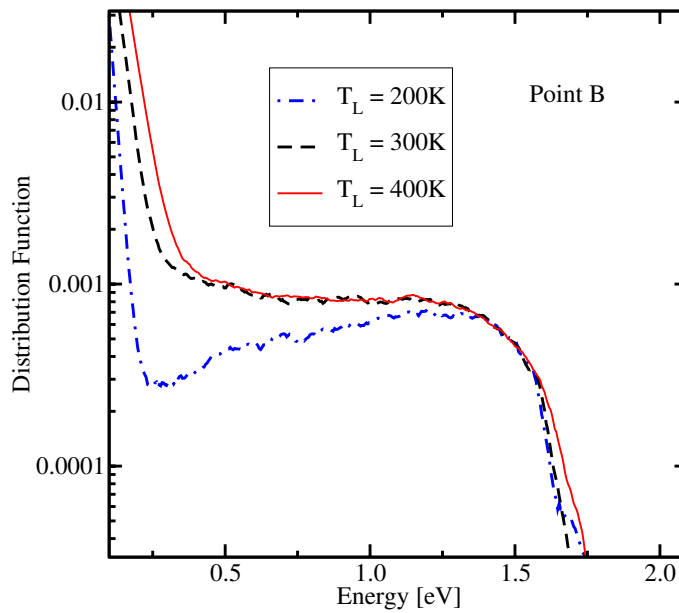


**Figure 2.14:** Distribution function at point B for lattice temperatures of 200 K, 300 K, and 400 K. The high energy tail of the carrier distribution function decreases for high lattice temperatures.

The ratio between the sixth moment and the 2D analytical expression from equation (2.124) as a function of the lower order moments from subband MC simulations through a SOI MOSFET

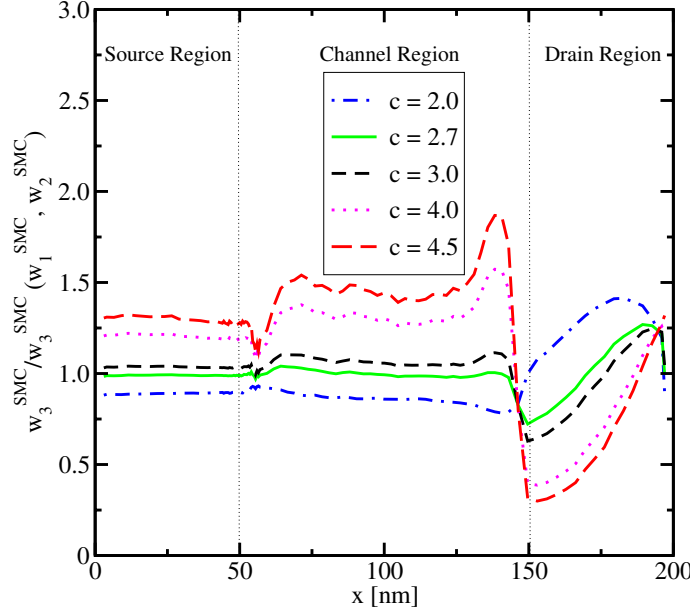


**Figure 2.15:** The ratio of the six moments model obtained from two-dimensional *Subband Monte Carlo* data with the analytical 2D closure relation of the six moments model for different  $c$  is presented. As can be observed is for the 2D case as well the best value.

with a channel length of 100 nm has been calculated in Fig. 2.15. As demonstrated in the 2D system the value 2.7 provides as well the best result.

All three non-parabolic factors are visualized in Fig. 2.16 using *Subband Monte Carlo* data. For low energies, the parabolic band approximation is valid, whereas for high-fields the non-parabolicity of the band structure must be taken into account. Finally, the derived macroscopic transport models can be generalized into one balance equation

$$\partial_t (nw_i) + \nabla_{\mathbf{r}} (n\mathbf{V}_i) + i s_{\alpha} q n \mathbf{V}_{i-1} \nabla_{\mathbf{r}} \tilde{\varphi} + n \frac{w_i - w_{i0}}{\tau_i} = 0, \quad (2.125)$$

and one flux equation

$$n\mathbf{V}_i = -n\mu_i H_{i+1} A \nabla_{\mathbf{r}} (nw_{i+1}) - s_{\alpha} n \mu_i (1 + iAH_i) w_i \nabla_{\mathbf{r}} \tilde{\varphi}. \quad (2.126)$$

For instance, in the case of the six moments model the index  $i$  is valid in the range  $i \in [0, 2]$  due to the incorporation of each three conservation and flux equations.

#### 2.4.3.4 Transport Parameter Modeling

It is challenging to model transport parameters as the mobilities  $\mu_0, \mu_1, \mu_2$ , and the relaxation times  $\tau_1$  and  $\tau_2$ , since they all depend on the actual shape of the distribution function, on the scattering rates, and on the band structure. They therefore contain information on hot-carriers and non-parabolicity effects. Theoretical models for a characterization of these parameters

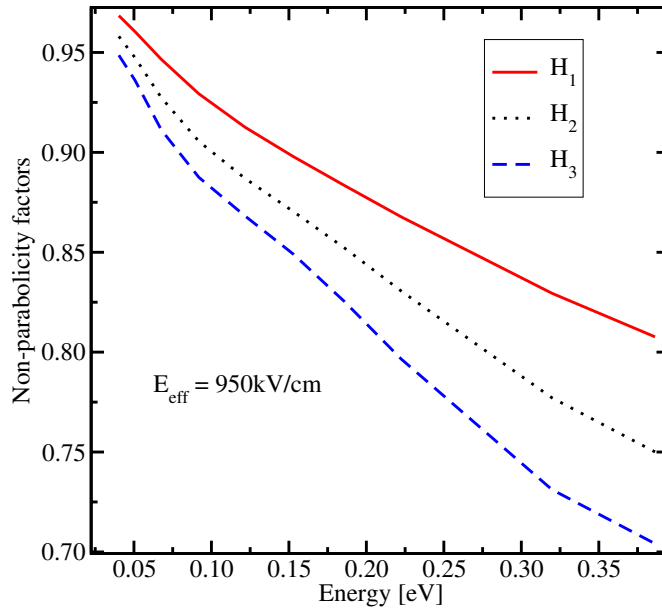


**Figure 2.16:**  $H_1, H_2$ , and  $H_3$  as functions of the energy with an effective field of 950 kV/cm. For low energies, the non-parabolicity factors approach unity. The non-parabolicity factors have been calculated out of *Sub-band Monte Carlo* simulations.

are often very complicated and simplified results are unsatisfying. For engineering purposes empirical models are often a better choice. A common assumption is that the effective carrier mobility is written as

$$\mu_0^{\text{LISF}} = \mu_0^{\text{LISF}} (\mu_0^{\text{LIS}} (\mu_0^{\text{LI}} (\mu_0^{\text{L}}))) , \quad (2.127)$$

with  $\mu_0^{\text{LISF}}$  as the mobility influenced by lattice scattering (index L), ionized impurity scattering (index I), surface scattering (index S), and carrier heating (index F). A very simple model to describe  $\mu_0^{\text{L}}$  is a power law ansatz. Empirical models for the characterization of the impact of ionized impurity and surface scattering on  $\mu_0$  can be found in [110] and [111], respectively.

The carrier mobility in the empirical mobility models are characterized by the electric field. But the mobilities depend on the distribution function and hence on the carrier energy rather than on the electric field as (for a parabolic band structure)

$$\mu_0 = \frac{q\tau_0(f)}{m^*} \approx \frac{q\tau_0(w)}{m^*} , \quad (2.128)$$

$$\mu_1 = \frac{q\tau_3(f)}{m^*} \approx \frac{q\tau_3(w)}{m^*} , \quad (2.129)$$

$$\mu_2 = \frac{q\tau_5(f)}{m^*} \approx \frac{q\tau_5(w)}{m^*} . \quad (2.130)$$

However, these simple empirical transport models did not deliver satisfactory results especially in the high field regime. Furthermore, a consistent comparison with other methods as for instance Monte Carlo simulations is difficult, because the transport model does not reproduce the Monte Carlo results in the homogeneous case [21].

In [112] a transport parameter model based on homogeneous fullband Monte Carlo tables has been introduced. Here, all higher-order transport parameters are extracted for different doping concentrations and for different driving forces. The transport parameters are then considered in the macroscopic transport models as a function of the average energy. Since all transport parameters are obtained from Monte Carlo simulations the transport models are free of fit parameters. Macroscopic models based on Monte Carlo data improves its counterpart models based on empirical models significantly, both in terms of numerical stability and in the agreement with Monte Carlo device simulations, as will be demonstrated in the next chapter.

#### 2.4.4 Monte Carlo Method

The Monte Carlo MC method is a statistical approach to solve the BTE equation [113–117]. The procedure does not aim at solving differential equations as described above, but to observe the trajectories of carriers as they move through a device under the influence of a driving field and scattering forces [1]. The method is illustrated in Fig. 2.17. The momentum of a particle is set as an initial condition. Pseudo-random numbers define the time of free flight of the particles as well as the scattering events. The simulation converges, when the statistical error of the quantities is under a certain limit. During convergence transport parameters like the carrier mobility or higher-order transport parameters can be extracted.

An advantage of this approach is that all kind of scattering mechanisms including for instance optical, acoustical phonon scattering and a general band structure can be modeled very precisely. Thus, the method is often used as a benchmark for computationally less expensive transport models. The disadvantage of this statistical approach is that the error bound of a quantity goes with  $1/\sqrt{N}$ , with  $N$  describing the number of random events. Therefore, with the increased accuracy of the factor  $\chi$ , the number of scattering events increases with  $\chi^2$  [118]. The consequence is that the simulation time increases as well. Therefore, for engineering applications, macroscopic transport models based on the method of moments, which are computationally much less expensive, are more suitable than the MC technique.

##### 2.4.4.1 Free Flight - Self Scattering

As displayed in Fig. 2.17, the free flight is an important part of the MC simulation. The coordinates of a moving particle in phase space with an applied electric field in  $x$  can be written as

$$\begin{aligned} p_x(t) &= p_x(0) - qE_x t, \\ p_y(t) &= p_y(0), \\ p_z(t) &= p_z(0), \end{aligned} \tag{2.131}$$

$$x(t) = x(0) - \frac{\mathcal{E}(t) - \mathcal{E}(0)}{qE_x},$$

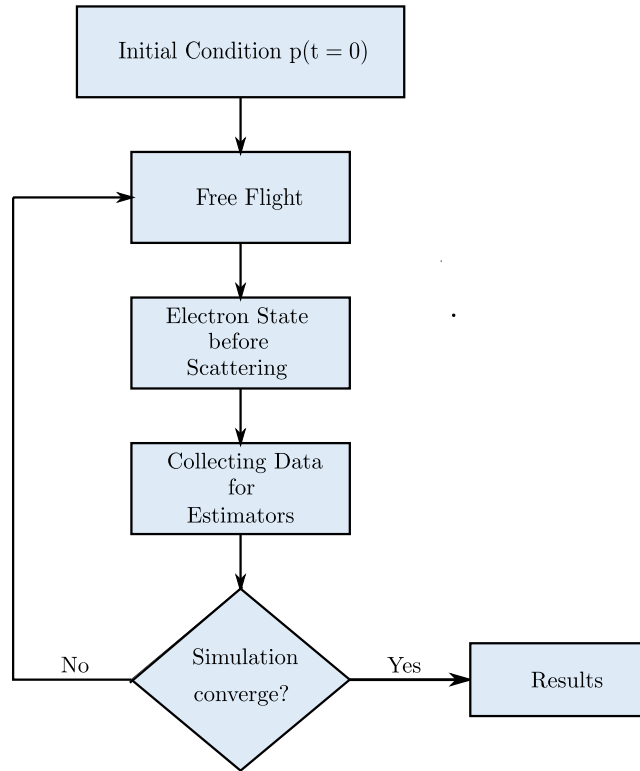


**Figure 2.17:** Flowchart of a MC Simulation (after [1])

$$y(t) = y(0) + \frac{p_y}{m_{n,p}^*} t, \quad (2.132)$$

$$z(t) = z(0) + \frac{p_z}{m_{n,p}^*} t.$$

$\mathcal{E}$  denotes the conduction band edge, whereas  $m_{n,p}^*$  is the effective mass of the electrons and holes, respectively. The scattering rates  $\Gamma$  of the carriers are indirectly proportional to the duration of the free flight [22]

$$\Gamma(\mathcal{E}) = \sum_{i=1}^k \frac{1}{\tau_i(\mathbf{p})}. \quad (2.133)$$

The sum includes all scattering mechanisms  $k$ , where the summation of  $\tau_i$  denotes the free flight. The probability of the carrier movement not being affected by the first collision between  $t$  and  $t + dt$  is the scattering rate times the probability that it survives until the time  $t$  [119]. For a random number generator that produces uniformly distributed numbers between  $u \in [0, 1]$ , the collision times can be expressed as [120]

$$t_{\text{coll}} = -\frac{1}{\Gamma_{\text{const}}} \ln(1 - u). \quad (2.134)$$

$\Gamma_{\text{const}}$  denotes a constant scattering rate and  $u$  are random numbers. Equation (2.134) is a very simple description of the free flight. In real semiconductor devices the scattering rates are energy

dependent. Hence, equation (2.134) must be rewritten to acknowledge this fact. This can be done by introducing the so called *self-scattering*  $\Gamma_{\text{self}}(\mathcal{E})$ . The  $\Gamma_{\text{self}}$  is defined as

$$\Gamma_{\text{self}}(\mathcal{E}) = \Gamma_0 - \Gamma(\mathcal{E}) . \quad (2.135)$$

Note that  $\Gamma_{\text{self}}$  is energy dependent. Finally, the total scattering rate ( $\Gamma_{\text{self}}(\mathcal{E}) + \Gamma(\mathcal{E})$ ) remains constant, so the simple equation (2.134) can be applied. It is important that the *self-scattering* does not influence the trajectories. Hence, the carriers momentum of a *self-scattering* event must be unchanged.

#### 2.4.4.2 Scattering Events

Equations (2.131) and (2.132) determine the free flight of the carriers in an electric field. The Monte Carlo method defines the correct scattering events as follows: After the free flight a new scattering event can be obtained in the range

$$\Gamma_{\text{before}}^{\text{Total}} \leq u < \Gamma^{\text{Total}} . \quad (2.136)$$

$\Gamma_{\text{before}}$  characterizes the total scattering rate according to equation (2.133) divided by the *self-scattering* rate before the scattering event.  $\Gamma^{\text{Total}}$  is defined via (2.133) divided by the *self-scattering* rate, whereas  $u$  is a uniform random number between 0 and 1. The relaxation times can be calculated via *Fermi's* golden rule [1]

$$S(\mathbf{p}, \mathbf{p}') = \frac{2\pi}{\hbar} |H_{\mathbf{p}'\mathbf{p}}|^2 \delta(\mathcal{E}(\mathbf{p}') - \mathcal{E}(\mathbf{p}) - \Delta\mathcal{E}) , \quad (2.137)$$

$$\frac{1}{\tau(\mathbf{p}_0)} = \sum_{\mathbf{p}' \uparrow} S(\mathbf{p}_0, \mathbf{p}') (1 - f(\mathbf{p}')) . \quad (2.138)$$

(2.138) is the rate at which carriers with a specific momentum  $\mathbf{p}_0$  and spin up scatter to any other state. In the sequel, the scattering at the interface based on (2.137) and (2.138) will be discussed, which is an important inversion layer effect.

As pointed out in [22], the scattering events calculated with the random procedure explained above are in very good agreement with the experiment.

#### 2.4.4.3 Fundamental Statistics

The Monte Carlo method allows to evaluate averages of microscopic quantities as defined in equation (2.69). Assuming an ensemble of  $N$  independent and identical particles, the estimation of an expected value based on an ensemble average can be expressed as [112, 121]

$$\langle x \rangle = \frac{1}{N} \sum_{j=1}^N w_j X(\gamma_j(t)) , \quad (2.139)$$

where  $\langle x \rangle$  is the macroscopic quantity and  $X$  is the corresponding microscopic counterpart.  $w$  is the statistical weight and  $\gamma_j$  denotes the state of the  $j$ th carrier. The weight  $w$  is defined as

$$0 \leq w_j \leq N \quad \text{and} \quad \sum_{j=1}^N w_j = N . \quad (2.140)$$



The Monte Carlo simulator used in this work, the so called *before-scattering* method is used [122]. Here, the averages are calculated at the end of the free flight. Hence, equation (2.139) is used right before the next scattering event. The relaxation times in a Monte Carlo simulator can be obtained as [123]

$$\tau_i = -n \frac{\langle \mathcal{E}^i \rangle - \langle \mathcal{E}_0^i \rangle}{\int \mathcal{E}^i Q_{\text{coll}}(f) d^3\mathbf{k}}. \quad (2.141)$$

$\mathcal{E}_0$  is the equilibrium energy. Only  $\mathcal{E}_0$  depends on the band structure. For the energy relaxation times, the equilibrium energy  $\mathcal{E}_0$  is defined as [123]

$$\langle \mathcal{E}_0 \rangle = \frac{\sum_{i=1}^3 Z_i m_i^{\frac{3}{2}} e^{-\frac{\mathcal{E}_i}{k_B T_n}} (\mathcal{E}_i p_0(T_n) + A k_B T_n p_1(T_n))}{\sum_{i=1}^3 Z_i m_i^{\frac{3}{2}} e^{-\frac{\mathcal{E}_i}{k_B T_n}} p_0(T_n)}. \quad (2.142)$$

$A$  is a dimension factor, whereas  $p_0(T_n)$  and  $p_1(T_n)$  are polynomials considering the non-parabolicity of the band structure [123]. The summation index  $i$  runs over all valleys in the material. In the case of silicon the index is in the range of 1 to 3. In a single valley, the equilibrium energy for three-dimensions can be calculated as

$$\langle \mathcal{E}_0 \rangle = \frac{3}{2} k_B T_n \frac{p_0(T_n)}{p_1(T_n)} \quad (2.143)$$

The mobilities for the six moments model can be obtained from the homogeneous macroscopic transport model as

$$\mu_0^d = \frac{V_0}{E}, \quad \mu_1^d = \frac{V_1}{E w_1 (1 + A H_1)}, \quad \text{and} \quad \mu_2^d = \frac{V_2}{E w_2 (1 + 2 A H_2)}. \quad (2.144)$$

$E$  is the electric field, the index  $d$  denotes the dimension of the electron gas, and in the numerators of equation (2.144), there are the odd moments of the BTE as explained in the previous section. Hence, the mobilities can be calculated as a post-processing step.

### 2.4.5 Spherical Harmonics Expansion

The *Spherical Harmonics Expansion* (SHE) procedure is a numerical method for solving the BTE. It gives approximate deterministic solutions of the BTE by an expansion of the distribution function  $f(\mathbf{r}, \mathbf{k}, t)$  in the  $\mathbf{k}$ -space into spherical harmonic functions  $Y_{lm}(\theta, \phi)$  [124]. As will be demonstrated the SHE procedure reproduces the results obtained from MC quite well with less computational effort.

Spherical harmonic functions are defined as [125, 126]

$$Y_{lm}(\theta, \phi) = \sqrt{\frac{2l+1}{4\pi} \frac{(l-m)!}{(l+m)!}} P_l^m(\cos(\theta)) e^{im\phi}, \quad (2.145)$$

with  $P_l^m(\cos(\theta))$  as the associated *Legendre* polynomial. The indices  $l$  and  $m$  are defined in the range  $l \in \{0, \infty\}$  and  $m \in \{-l, l\}$  respectively. Furthermore, the spherical harmonics are orthogonal,

$$\int_0^\pi \int_0^{2\pi} d\Omega Y_{lm}(\theta, \phi) Y_{l'm'}^*(\theta, \phi) = \delta_{l'l} \delta_{m'm}, \quad (2.146)$$

normalized and complex valued [127]. The second term with the primed indices of (2.146) is the conjugate complex term of  $Y_{lm}(\theta, \phi)$ , whereas  $d\Omega$  is defined as  $d\Omega = \sin \theta d\theta d\phi$ .

For instance the spherical harmonic functions  $Y_{00}$ ,  $Y_{10}$ ,  $Y_{11}$ , and  $Y_{20}$  can be expressed as

$$Y_{00} = \sqrt{\frac{1}{4\pi}}, \quad Y_{10} = -\sqrt{\frac{3}{8\pi}} \sin(\theta) e^{im\phi}, \quad Y_{11} = \sqrt{\frac{3}{4\pi}} \cos(\theta), \quad \text{and} \quad Y_{20} = \sqrt{\frac{5}{16\pi}} (3\cos^2(\theta) - 1). \quad (2.147)$$

$Y_{00}$  is a sphere, while  $Y_{10}$  and  $Y_{11}$  are visualized in Fig. 2.18.

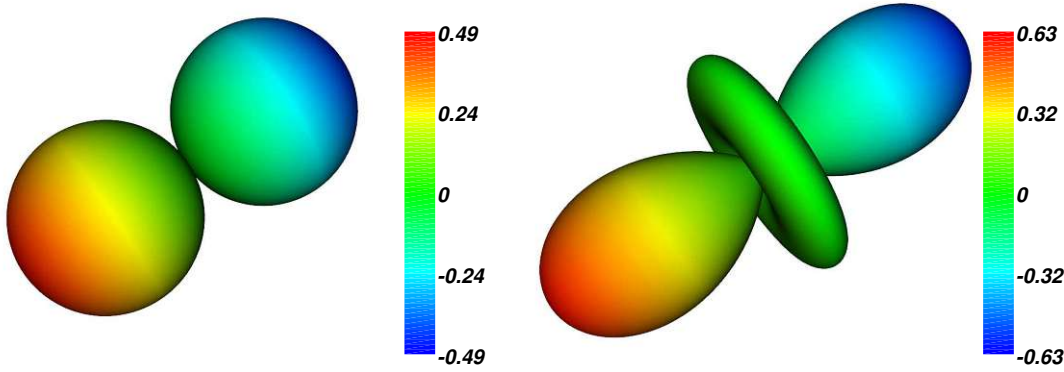


**Figure 2.18:**  $Y_{10}$  and  $Y_{11}$  in polar coordinates

Note that for rotational symmetry in the  $\phi$  direction, the spherical harmonic function is reduced to the associated *Legendre* polynomials.

The distribution function can be now expanded as

$$f(r, k) = \sum_{l=0}^{\infty} \sum_{m=-l}^l f_{lm}(r, k) Y_{lm}(\theta, \phi). \quad (2.148)$$

The coefficients  $f_{lm}(r, k)$  are given by

$$f_{lm}(r, k) = \int_0^{\pi} \int_0^{2\pi} d\Omega f(\theta, \phi) Y_{l'm'}^*(\theta, \phi). \quad (2.149)$$

The fluxes for a three-dimensional electron gas as defined in (2.83) can be now expressed as

$$n\mathbf{v}_i = \sum_{l=0}^{\infty} \sum_{m=-l}^l \int_0^{\pi} \int_0^{2\pi} d\Omega \mathbf{v} \mathcal{E}^i f_{lm}(\theta, \phi) Y_{lm}(\theta, \phi). \quad (2.150)$$

The next step is to apply the SHE method to the stationary BTE. For the sake of clarity, the transport direction of the carriers is assumed just along the  $z$  coordinate and a parabolic band structure is taken into account. Hence, the expansion (2.149) reduces to

$$f(z, k) = \sum_{l=0}^N f_l(z, k) P_l(\cos(\theta)), \quad (2.151)$$

where the angle  $\theta$  is specified by the direction of the electric field and the  $P_l(\cos(\theta))$  are the *Legendre* polynomials. Before substituting the distribution function with spherical harmonics, a variable transformation from  $k$ -space into  $\mathcal{E}$ -space is performed. The transformation into the  $\mathcal{E}$ -space has many advantages, e.g. in equilibrium, the distribution function is isotropic on equienergy surfaces [127]. Inserting the expansion (2.151) into the BTE, one can obtain the BTE expressed by the SHE [128, 129]. The first two lowest order expansions can be written as

$$l = 0 \Rightarrow \quad \partial_z f_1 - qE (\partial_{\mathcal{E}} f_1 + \Gamma_B f_1) = \frac{1}{v} (\partial_t f_0)_{\text{coll}}, \quad (2.152)$$

$$l = 1 \Rightarrow \quad \partial_z f_0 - 2\partial_z f_2 - qE (\partial_{\mathcal{E}} f_0 + 2\partial_{\mathcal{E}} f_2 + 3\Gamma_B f_2) = \frac{3}{v} (\partial_t f_1)_{\text{coll}}. \quad (2.153)$$

For  $N \rightarrow \infty$ , the result is an exact solution of the BTE. In Fig. 2.20, a velocity profile of an  $n^+nn^+$  structure calculated with a MC simulation and with SHE simulations taking several *Legendre* polynomials into account is shown. The result is different from the MC simulation considering just one *Legendre* polynomial, whereas for at least 9 polynomials, both simulations are in good agreement. Therefore, the SHE simulation is a good benchmark alternative to the Monte Carlo technique considering enough polynomials.

The question may arise about the relation of the SHE to macroscopic models as e.g. the drift-diffusion model. The answer to this question will be discussed in the following.

Assuming a homogeneous, stationary system with an applied electric field  $\mathbf{E}$ , the macroscopic relaxation time approximation on the right hand side of the BTE, parabolic bands, and the diffusion approximation [51], the BTE can be written as

$$-q\mathbf{E}\nabla_{\mathbf{p}}f = -\frac{f - f_0}{\tau_0}. \quad (2.154)$$

To derive an expression for the anti-symmetric part of the distribution function  $f_a$ , which is the important part for systems within non-equilibrium conditions, the distribution function  $f$  can be split into a symmetric part  $f_s$  and  $f_a$ . Due to the assumption of the diffusion approximation

$$f_s \gg f_a, \quad (2.155)$$

which states that the system is not very far away from equilibrium. The equation (2.154) can now be used to derive an expression for the anti-symmetric part  $f_a$  [1]

$$f_a = q\tau_0\mathbf{E}\nabla_{\mathbf{r}}f_0 = \frac{q\tau_0f_0}{k_B T_L}\mathbf{E}\mathbf{v} = \frac{q\tau_0\hbar}{k_B T_L m^*}f_0|\mathbf{E}||\mathbf{k}|P_1(\cos(\theta)). \quad (2.156)$$

Inserting equation (2.156) into (2.150) the drift term of the drift-diffusion model is obtained.

Hence, taking just the first *Legendre* polynomial of the SHE, in a homogeneous system within the low-field regime, the results of the SHE are equal to the results from drift-diffusion simulations.

In Fig. 2.19, the low-field and the high-field mobility calculated with a SHE simulator and a standard drift-diffusion model as a function of the doping concentration is shown. In the SHE simulator, only the first *Legendre* polynomial has been taken into account. The results of the two simulations show a very good agreement in the low-field regime, whereas the assumptions

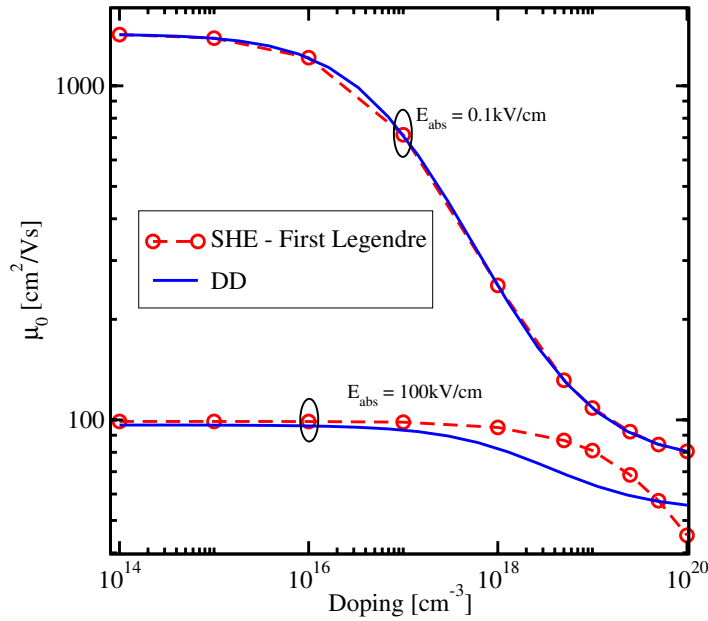


**Figure 2.19:** A comparison of the low and high-field mobility as a function of the doping in the bulk calculated with the SHE method and the drift-diffusion model. In the SHE simulation, only the first *Legendre* polynomial has been taken into account.

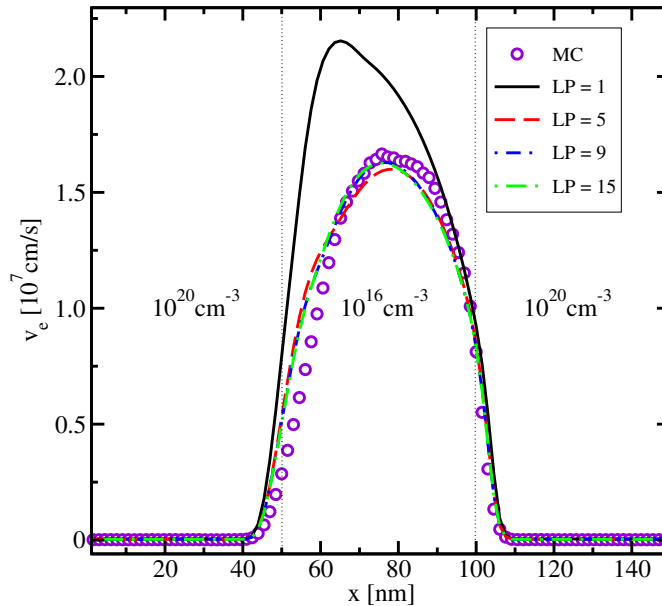


**Figure 2.20:** The velocity profile of an  $n^+nn^+$  structure calculated with a device MC simulation and with a SHE simulator taking 1, 5, 9, and 15 *Legendre* polynomials (LP) into account.

stated above are not valid anymore for high-fields. The situation changes taking more than one *Legendre* polynomial into account.

As demonstrated in Fig. 2.20, the SHE method is in very good agreement with MC simulations when at least 9 *Legendre* polynomials are considered. Due to the good agreement with MC simulations in short channel devices and to the shorter simulation time of the SHE method compared to MC, the SHE method is used as a reference solution for the derived three-dimensional higher-order macroscopic transport models in the next chapter.

*'Any sufficiently advanced technology is indistinguishable from magic.'*

Arthur C. Clarke

## Chapter 3

---

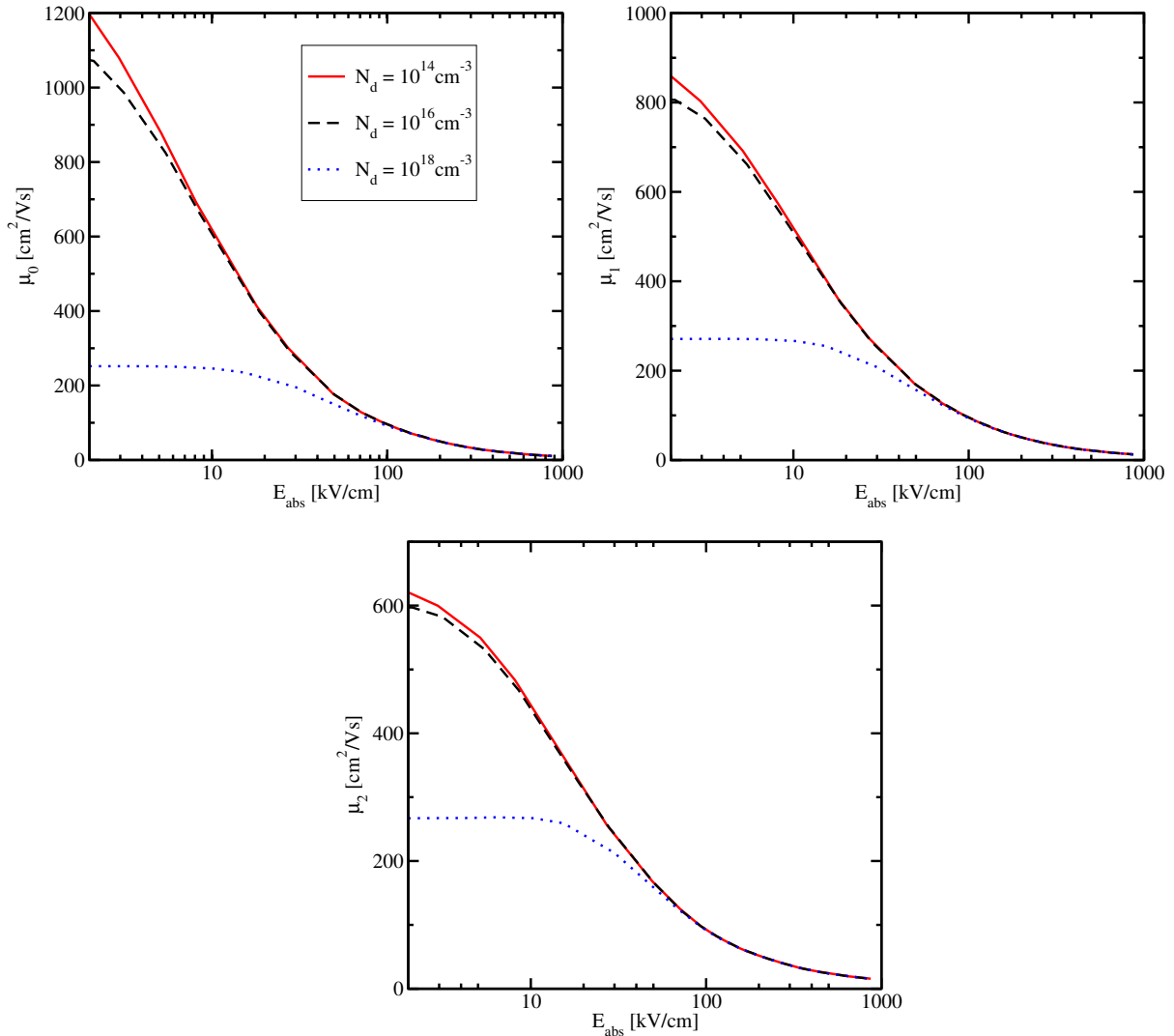
# The Three-Dimensional Electron Gas

---

**T**HIS CHAPTER investigates the validity of higher-order transport models on a series of the most popular test devices, one dimensional  $n^+nn^+$  structures. These topologies display similar features as a MOSFET and bipolar transistors like a distinctive velocity overshoot and a mixture of a hot and a cold distribution function in the drain region. Therefore, it is possible to study the basic behavior of macroscopic transport models for very small devices within  $n^+nn^+$  structures without the additional levels of complexity introduced by two-dimensional MOS devices [21, 130]. In order to consider the high-field case as accurately as possible, a transport model based on fullband MC tables is considered. The results of the MC based higher-order transport models are benchmarked against the SHE and MC simulations.

### 3.1 Table Based Macroscopic Transport Models

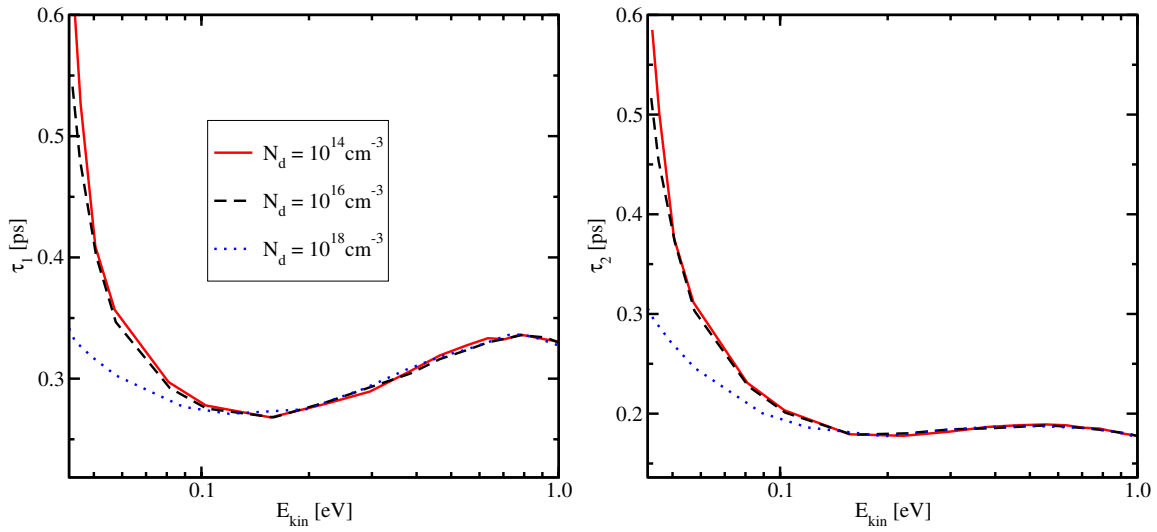
For an accurate description of higher-order transport models, it is important to model higher-order transport parameters with as few simplifying assumptions as possible [21, 131]. The fullband bulk MC tables with respect to different doping concentrations and different driving fields are used as a base for a parameter interpolation within macroscopic transport models [132]. Fullband structure of the material, scattering mechanisms such as phonon induced scattering are now inherently considered in the MC tables, and in the following also in the transport model. Hence, approximate methods for the transport parameter modeling e.g. the low field mobility model after [110] are replaced by the MC table based model. Furthermore, the transport parameters of three-dimensional simulations can be expressed as a function of the doping concentration and the driving force. The extracted bulk parameter-set needed for higher-order macroscopic transport models is displayed in Fig. 3.1 and Fig. 3.2. Here the carrier mobility  $\mu_0$  and higher-order mobilities  $\mu_1$  and  $\mu_2$  as a function of the electric field  $E_{\text{abs}}$  for different doping concentrations  $N_d$  are presented. As can be observed, for fields above 100 kV/cm the values of the mobilities are independent of the doping concentration, while for low fields and low doping concentrations, the carrier mobility is very high compared to low fields and high doping concentrations. The energy flux mobility and the second-order energy flux mobility are lower than the carrier mobility for low doping concentrations and low fields, while for low fields and high doping concentrations, the value of all three mobilities are comparable.



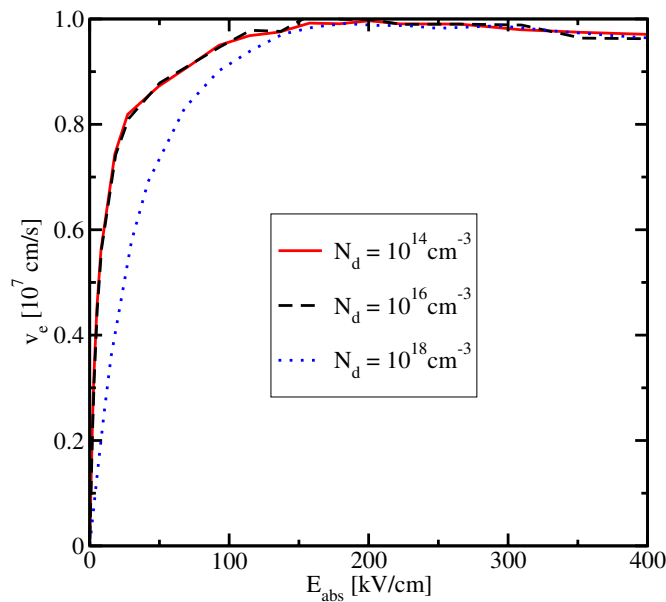
**Figure 3.1:** Carrier mobility  $\mu_0$ , energy flux mobility  $\mu_1$ , and second-order energy flux mobility  $\mu_2$  versus driving field for different doping concentrations. For fields higher than 100 kV/cm, the mobilities are independent of the doping concentration, while for low fields the values of the mobilities of the low doping case is high compared to high doping concentrations.

Fig. 3.2 presents the relaxation times  $\tau_1$  and  $\tau_2$  for different doping concentrations and as a function of the kinetic energy of the carriers. As can be seen, for high energies the relaxation times are doping independent and decrease due to the increase of optical phonon scattering. For high  $N_d$ , the MC simulations predict low relaxation times compared to low  $N_d$ .

The carrier velocity as a function of the lateral field and for different  $N_d$  is demonstrated in Fig. 3.3. The saturation velocity of Si is reached at a driving field of 150 kV/cm.



**Figure 3.2:** Energy-relaxation time  $\tau_1$  and second-order energy relaxation time  $\tau_2$  extracted from bulk MC simulations as a function of the kinetic energy for different bulk dopings. For very high energies, the relaxation times decrease due to the increase of optical phonon scattering.



**Figure 3.3:** Bulk velocity of electrons as a function of the driving field  $E_{\text{abs}}$  for a doping of  $10^{14} \text{ cm}^{-3}$ ,  $10^{16} \text{ cm}^{-3}$ , and  $10^{18} \text{ cm}^{-3}$ . In the low field regime, the electron velocity for high dopings is lower than the velocity of the low dopings, while the value of the velocity converges for high fields.



## 3.2 Device Studies

A study concerning the behavior of three-dimensional macroscopic transport models in long and short  $n^+nn^+$  test structures is given and compared to SHE and MC simulations. Short channel effects as the velocity overshoot, impact ionization, and the influence of hot electrons on the carrier distribution function are discussed.

### 3.2.1 Long Channel Devices

First, a study on the behavior of higher-order transport models in long channel devices is performed. The aim is to find a calibration point, where all macroscopic transport models together with the spherical harmonics approach, which is the reference simulator here, yield the same result. Thus,  $n^+nn^+$  structures with a channel length from 1000 nm down to 100 nm and with a doping profile of  $10^{20} \text{ cm}^{-3}$  and  $10^{16} \text{ cm}^{-3}$  have been investigated.

Fig. 3.4 shows the output currents of different  $n^+nn^+$  structures for channel lengths of 100 nm, 250 nm, and 1000 nm calculated with the DD, ET, SM and the SHE model.<sup>1</sup> As can be observed for a channel length of 1000 nm all models yield the same results with an error below 1% (see Fig. 3.5). While the error of the ET and SM model stays more or less constant below 2.5% for a channel length down to 250 nm, the error of the DD model continuously increases and reaches a value of  $-16\%$  for a channel length of 100 nm. While the inaccuracy of the ET model starts to increase below 250 nm, the SM model gives still results very close to SHE simulations. Therefore, simulating short channel devices with the DD model gives only poor results. However, for devices with a channel length of  $1 \mu\text{m}$ , the DD, ET, SM, and the SHE model predict the same current value with an error of below 1%. Hence, the calibration point is the 1000 nm channel device.

### 3.2.2 Short Channel Effects

Since the channel length is reduced to increase the operation speed and the number of components per chip, the so called short-channel effect arise [133]. The first short channel effect described here is the velocity overshoot.

#### 3.2.2.1 Velocity Overshoot

The velocity overshoot in short channel devices has been the object of many investigations [134–138]. The carrier velocity in most devices operating near room temperature and under modest bias condition is always limited by scattering. Carriers cannot go beyond a certain velocity. The maximum velocity observed in bulk silicon measurements is the saturation velocity  $v_{\text{sat}}$ . The value of  $v_{\text{sat}}$  is  $10^7 \text{ cm/s}$  [139]. However, as demonstrated in Fig. 3.6 for short channel devices the situation is different. As the channel length decreases, the electric field inside the device increases as well. Thus, the carriers will be accelerated without colliding with the lattice ( $T_n = T_L$ ) for at least a few pico seconds. Therefore, the random component of the carrier velocity induced by scattering events is small, which leads to a maximum drift velocity in the range of  $10^7 \text{ cm/s}$  to  $10^8 \text{ cm/s}$  [140]. This is known as the velocity overshoot.

<sup>1</sup>Thanks to Prof. Jungemann for providing his SHE simulator

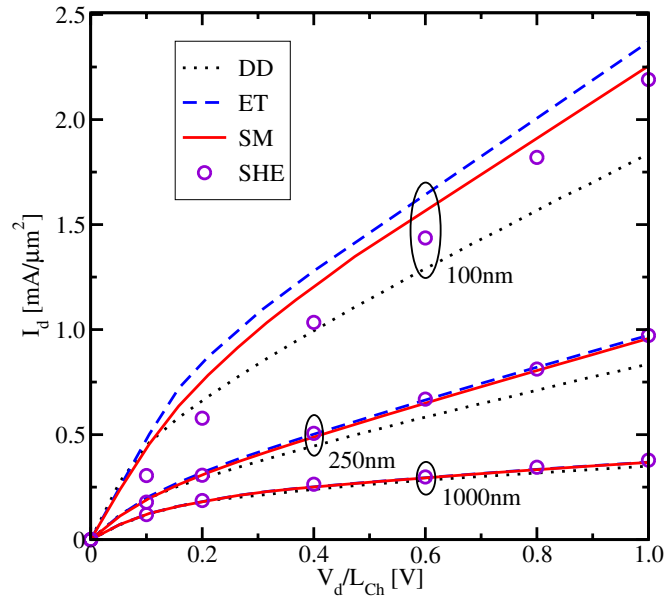


**Figure 3.4:** Output currents for different  $n^+n^+$  structures calculated with DD, ET, and SM models. As a reference, SHE simulations are used. For 1000 nm, all models predict the same current, while the DD model underestimates the current for a channel length of 100 nm.

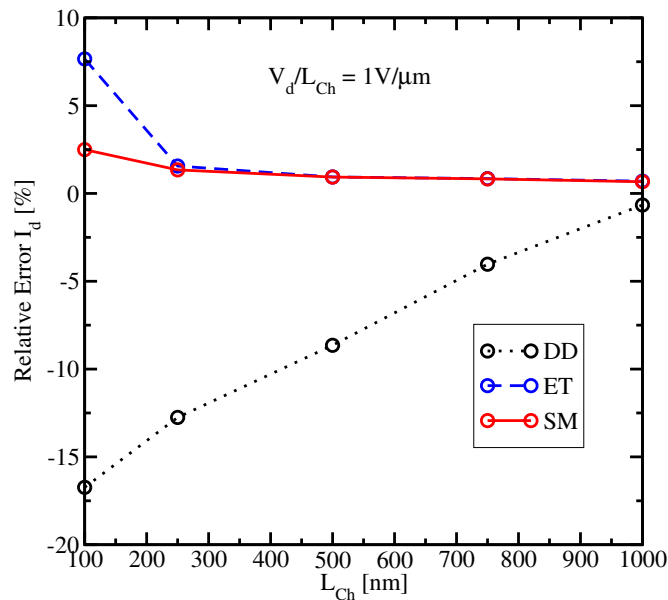


**Figure 3.5:** Relative error of the current calculated with the DD, ET, and the SM model as a function of the channel length. A voltage of 1 V has been applied. While the ET and SM model is below 7.5 %, the DD model approaches to 16 % at a channel length of 100 nm.

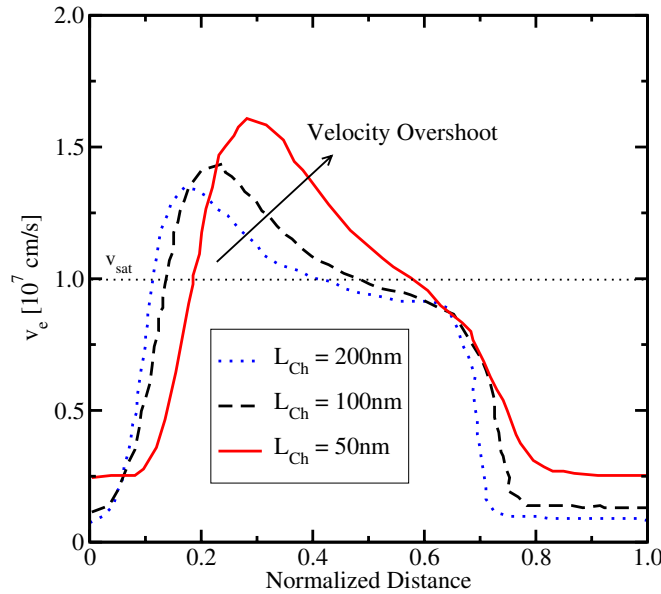


**Figure 3.6:** Velocity profiles of a 50 nm, 100 nm, and 200 nm long  $n^+nn^+$  structure calculated with the MC method are presented after [4]. The velocity overshoot at the beginning of the lowly doped  $n$ -region is clearly visible.

### 3.2.2.2 Hot Electrons

Hot electrons can enter the oxide, where they can be trapped, giving rise to oxide charging and can accumulate with time and degrade the device performance by increasing the threshold voltage and adversely affect the gate control on the drain current [133].

Therefore, an analytical expression within high fields for the carrier temperature  $T_n$  in a homogeneous and stationary bulk Si system is derived. Here, all spatial gradients in the transport models can be neglected. Hence, the energy balance equation (2.108) can be formulated as

$$-s_\alpha q n \mathbf{V}_0 \mathbf{E} + n \frac{w_1 - w_{10}}{\tau_1} = 0. \quad (3.1)$$

With

$$w_{10} = \frac{3}{2} k_B T_L \quad \text{and} \quad w_1 = \frac{3}{2} k_B T_n, \quad (3.2)$$

$T_n$  can be written as [4]

$$T_n = T_L + \frac{2}{3} \frac{q}{k_B} \tau_1 \mu_0 \mathbf{E}^2. \quad (3.3)$$

Note that only the drift term of the current

$$n \mathbf{V}_0 = s_\alpha n \mu_0 \mathbf{E} \quad (3.4)$$

has been inserted into the homogeneous energy balance equation. As has been pointed out,  $T_n$  is roughly proportional to the square of the electric field. In a certain high field regime,

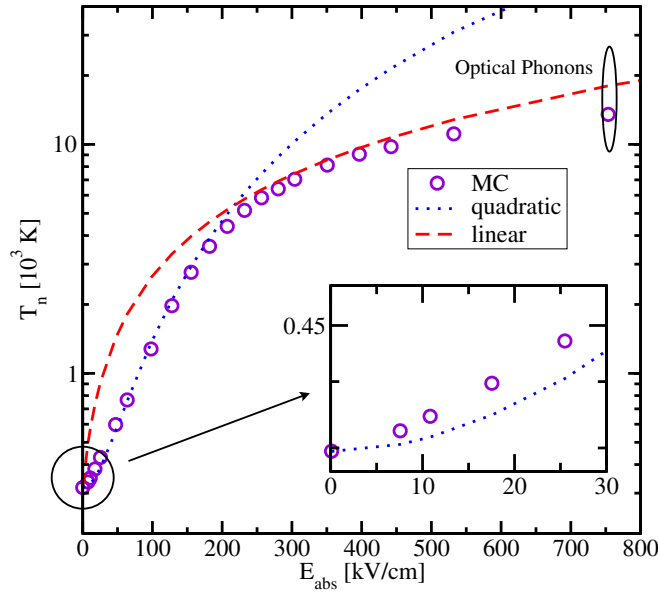


**Figure 3.7:** Carrier temperature  $T_n$  as a function of the driving field in a homogeneous bulk simulation carried out with fullband MC. For lower fields, the carrier temperature is a function of  $E^2$ , while for high fields, the temperature is a linear function of the driving field.

where optical phonons can be neglected, the energy relaxation time  $\tau_1$  is more or less constant (see Fig. 3.2). Note that optical phonon scattering is an inelastic process, which changes the energy relaxation time. In this special high field regime,  $\mu_0$  can be written as [140]

$$\mu_0 = \frac{v_{\text{sat}}}{E}, \quad (3.5)$$

and the temperature expression (3.3) can be described in terms of the saturation velocity  $v_{\text{sat}}$  as

$$T_n = T_L + \tau_{\text{const}} \frac{2q}{3k_B} v_{\text{sat}} E. \quad (3.6)$$

For electrons within the saturation velocity regime,  $T_n$  is a linear function of the electric field. In Fig. 3.7, the bulk carrier temperature as a function of the electric field calculated with the bulk fullband MC method is presented. In order to consider the whole band structure of Si fullband MC has been taken into account instead of the analytical SHE method. As pointed out, the quadratic dependence of the carrier temperature from the electric field is a good approximation for fields lower than 200 kV/cm, while for higher fields up to 450 kV/cm the linear approximation (3.6) can be used. However, for driving fields above 450 kV/cm the linear approximation breaks down due to optical phonon scattering, which changes  $\tau_1$ . Thus, the assumption that the energy relaxation time is constant is not valid anymore.

### 3.2.2.3 Hot and Cold Electrons

Carrier energy has got a deep impact on the distribution function. The so called high-energy tail at the beginning of the drain region, which is an expression of the coexistence of a hot electron

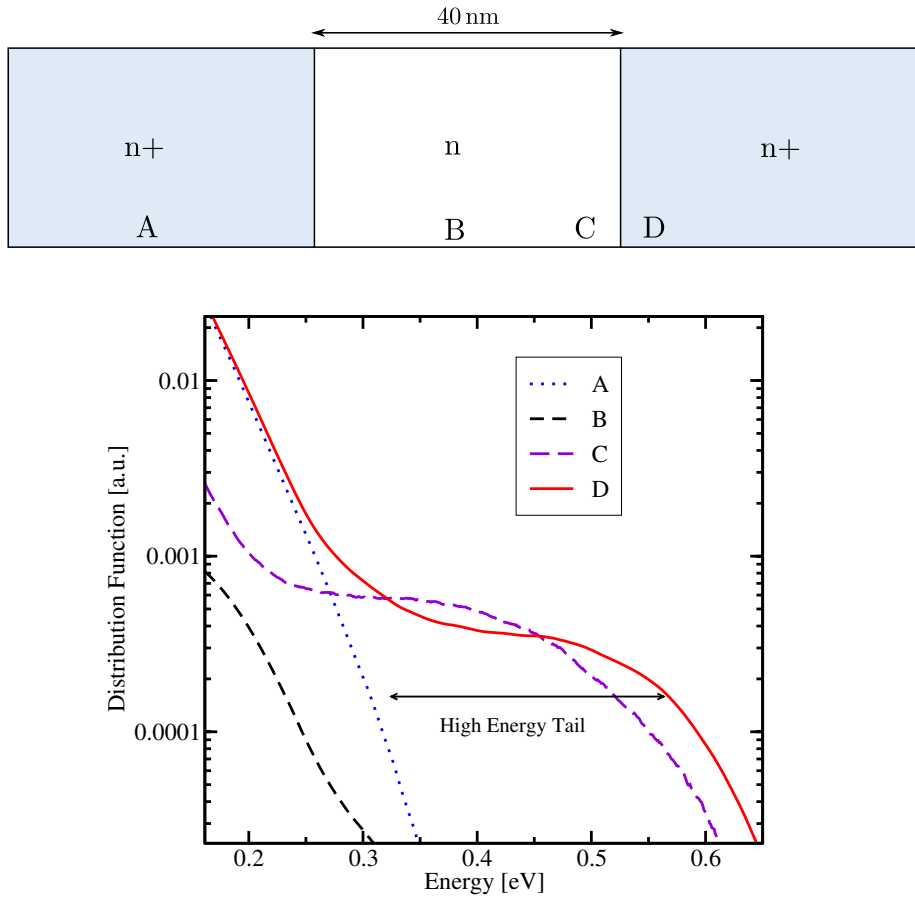


**Figure 3.8:** Evolution of the distribution function inside an  $n^+nn^+$  structure. The mixture of hot and cold electrons is expressed by the high-energy tail of the carrier distribution function.

population coming from the channel and the cold electron population from the drain region, is presented in Fig. 3.8. Here, the evolution of the distribution function through a  $n^+nn^+$  structure with a channel length of 40 nm and a doping profile of  $10^{20} \text{ cm}^{-3}$  and  $10^{16} \text{ cm}^{-3}$  is demonstrated. An electric field of 50 kV/cm in the middle of the channel has been assumed. The distribution function is calculated with the MC method. At point A a *Maxwellian* can be assumed as the carrier distribution function, while at point B the heated *Maxwellian* overestimates the carrier distribution function. In point D the high-energy tail occurs.

In [141], an analytical distribution function model has been developed, which goes beyond the assumption of a *Maxwellian* shape. The symmetric part of the distribution function is based on a mixture of a cold and a hot *Maxwellian* and can be expressed as [141]

$$f_s(\mathcal{E}) = A \left( \exp \left( - \left( \frac{\mathcal{E}}{a} \right)^b \right) + c \exp \left( - \frac{\mathcal{E}}{a_c} \right) \right) = A (f_h(\mathcal{E}) + c f_c(\mathcal{E})) . \quad (3.7)$$

The five parameters  $A$ ,  $a$ ,  $b$ ,  $c$ , and  $a_c$ , which describe the distribution function, must be determined and are calculated in that way that the distribution reproduces the first three even moments provided by the six moments model. Since the DD and the ET models exhibit only

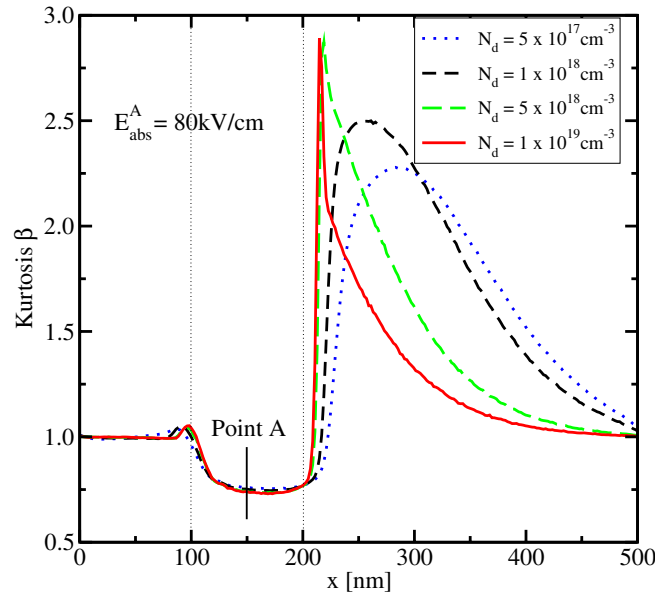


**Figure 3.9:** Kurtosis calculated for different source and drain doping concentrations in an  $n^+nn^+$  structure with a channel length of 100 nm. The maximum peak of the kurtosis for high doping concentrations is very high compared to the low doping case.

two and three equations, respectively, the SM model provides enough equations to calculate the five parameters. Of fundamental importance to this model is the kurtosis. The kurtosis gives the information to differentiate between the channel region and the drain region [141].

The kurtosis of an  $n^+nn^+$  structure with a 100 nm channel for different source and drain dopings is visualized in Fig. 3.9. There, a channel doping of  $10^{16} \text{ cm}^{-3}$  has been considered. As can be observed for low dopings, the maximum peak of the kurtosis is at 300 nm, compared to high dopings, where the maximum is at about 220 nm.

This can be explained as follows: Due to the higher concentration of cold electrons in the drain region of the high doped drain, the relaxation of hot carriers is faster than in the low doped drain region. Hence, the maximum peak of  $\beta$  in the high doping concentration case is 25 % higher than for low doping concentrations.

In Fig. 3.10, the second-order temperature  $\Theta$  defined as

$$\Theta = \beta T_n, \quad (3.8)$$

and the carrier temperature  $T_n$  for a short and a long channel devices are presented. For the long channel device, the hot distribution part of equation (3.7) can be neglected due to the small deviation of the second-order temperature  $\Theta$  from  $T_n$ . In short channel devices as the 60 nm device, an accurate modeling of the high-energy tail is very important as demonstrated in Fig. 3.11.

Here, carrier distribution functions of a 40 nm, 60 nm, 80 nm, and 100 nm channel devices at point D of Fig. 3.8 are shown. The distribution functions are calculated with the MC method.

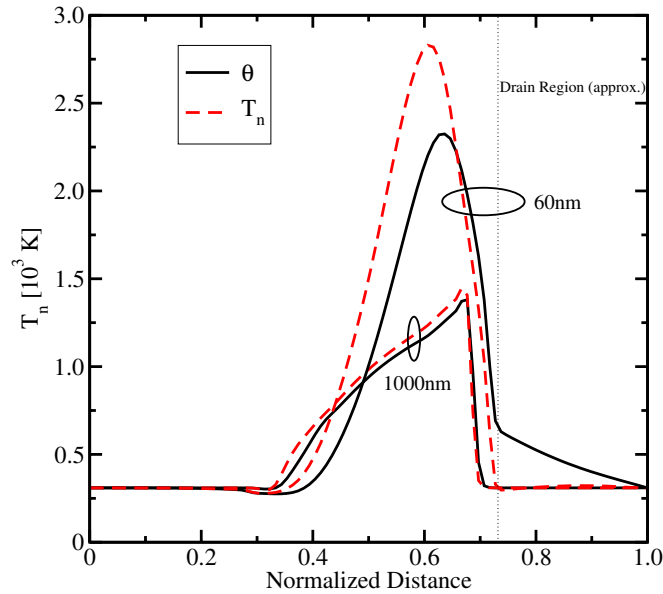


**Figure 3.10:** Carrier temperature  $T_n$  together with second-order temperature  $\Theta$  for a 1000 nm and a 60 nm device. A field of 50 kV/cm has been assumed. While in the long channel device a *Maxwellian* can be used, the high-energy tail in the short channel device in the drain region increases.

As pointed out for increasing channel lengths the high-energy tail decreases. Also high fields have got a strong influence on the kurtosis as shown in Fig. 3.12. Here, the kurtosis for 5 kV/cm, 20 kV/cm, and 50 kV/cm fields of a 100 nm channel length structure is demonstrated in the upper left part of Fig. 3.12. The electric field has been calculated in the middle of the channel at point A. As can be seen for low fields as 5 kV/cm, where the carrier temperature is low (see the upper right part) a heated *Maxwellian* can be used, while for 20 kV/cm an increase of the kurtosis at the beginning of the drain region is visible. A significant increase of the kurtosis can be observed for high fields.

The kurtosis starts to rise, when the maximum of the carrier temperature decreases to the equilibrium value. This is the region, where the hot electrons from the channel meet the large pool of cold electrons in the drain region. The distribution function has also a strong impact on the carrier velocity as pointed out in the lower part of Fig. 3.12. The ET transport model yields the same velocity profile in the low field regime as the SM model, which is also an indication that a *Maxwellian* is a good approximation within low fields. However, for high fields, the ET overestimates the velocity profile of the DD and the SM model, and has got a maximum at the end of the channel. A second velocity overshoot in the ET and in the SM model can be observed, which will be discussed in the next section.

### 3.2.2.4 Impact Ionization

Impact ionization especially occurs in n-channel MOSFETs, due to the high velocity of the electrons and high lateral fields. The electrons collide with Si atoms and generate electron hole pairs. Hence, the probability of impact ionization for electrons in a strong field is determined by the probability that the electrons will acquire the ionization energy of the atoms from the

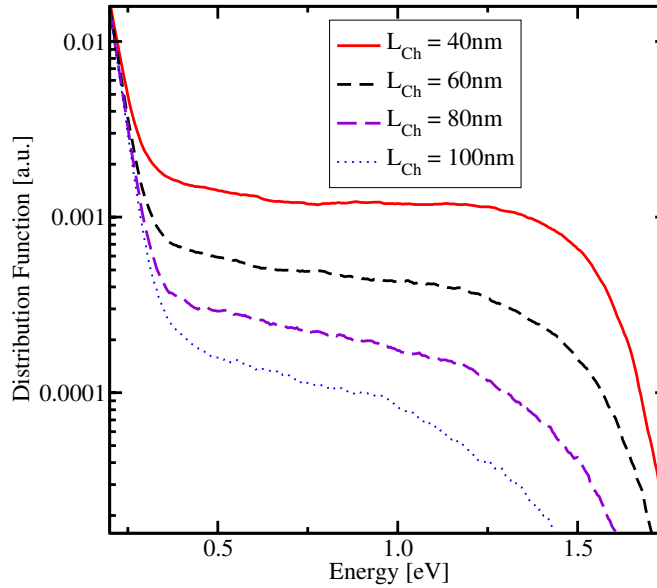


**Figure 3.11:** Distribution function at point D of Fig. 3.8 for 40 nm, 60 nm, 80 nm, and 100 nm channel devices. As can be observed, the high-energy tail for increasing channel lengths decrease.

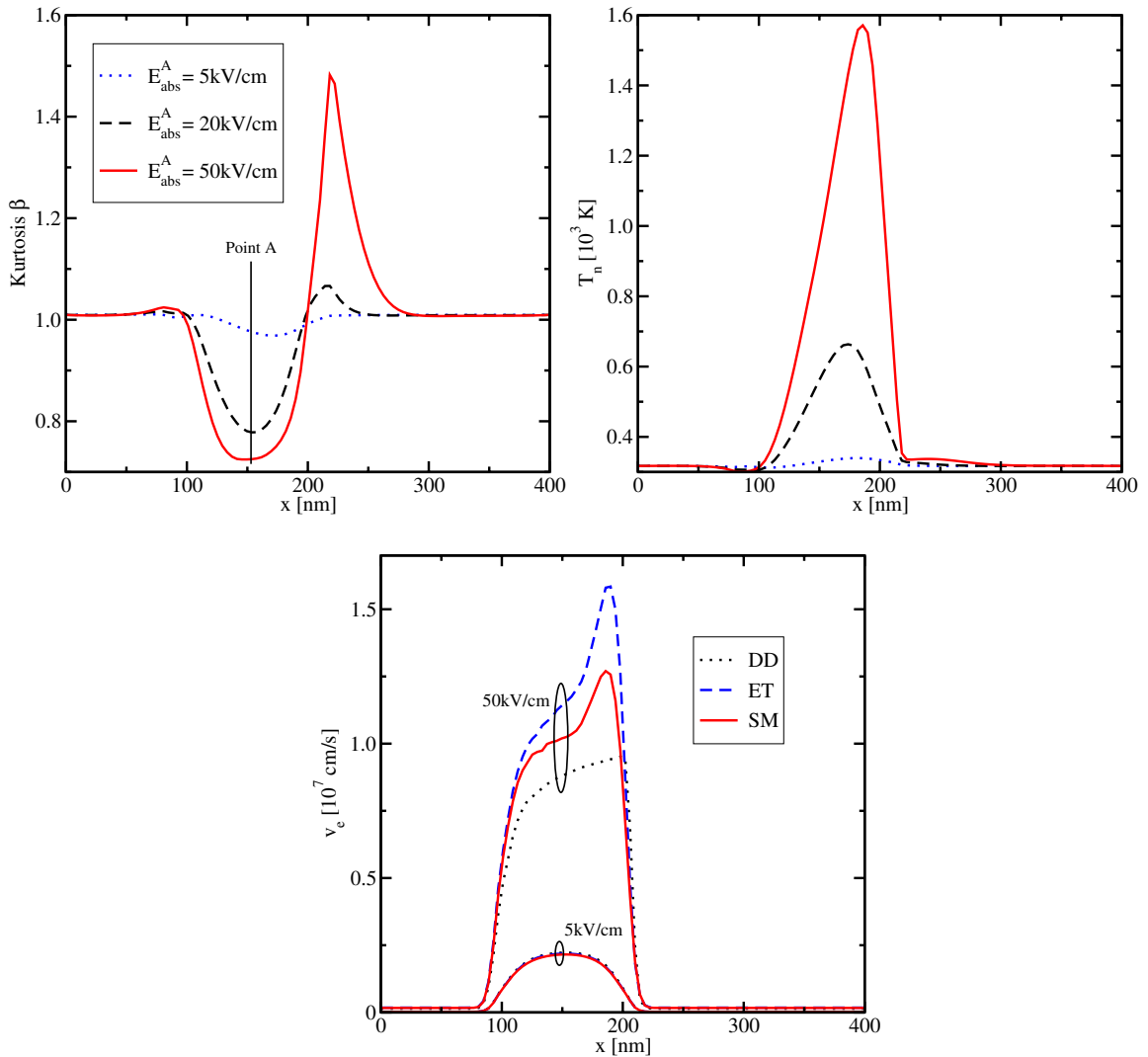
field [142]. The process of increasing energies of the electrons depends on two factors: Acceleration in the field and energy dissipation with phonons. Thus, electrons can gain energy from the field without experiencing a single collision, or the second possibility of receiving the same energy is that the electrons achieve energy after many collisions, in that way that in each collision the electron loses less energy than it receives from the field during the time between two collisions.

Fig. 3.13 shows impact ionization rates of a 200 nm and a 50 nm channel device calculated with the DD, ET, SM model and the MC method. As can be observed, the impact ionization rate predicted by the SM model is closer to MC data than the ET and the DD model due to the better modeling of the distribution function in the SM model, as explained in the following section.

### 3.2.3 Application of Higher-Order Models on Deca-Nanometer Devices

Higher-order transport models such as the SM model can cover non-local effects due to the improved modeling of the distribution function. This is very important for deca-nanometer devices, where short channel effects have a strong influence on carrier transport properties. The channel length range of deca-nanometer devices is defined in this work from 100 nm down to 20 nm. However, beside the advantages of higher-order transport models concerning the description of the explained effects, the models also predict a velocity overshoot, when the electric field decreases rapidly. This is the case for instance at the end of the channel of a MOSFET. Since the velocity overshoot at the end of the channel is not observed by MC simulations, the effect is known as the *spurious velocity overshoot* (SVO) [143–145]. In [6] it was demonstrated that the reason for the SVO is due to the closure relation and to the modeling of the transport





**Figure 3.12:** Kurtosis  $\beta$  and the carrier temperature for electric fields of 5 kV/cm, 20 kV/cm, and 50 kV/cm through a 100 nm channel  $n^+n^+$  device (the value of the fields in the upper left part is calculated at point A). For high fields, the kurtosis increases at the beginning of the drain region, which means that the high-energy tail of the distribution function is becoming very important. In the right upper part, the carrier temperature profile for different electric fields is shown. The kurtosis exceeds unity, while the carrier temperature drops down. The velocity profile for fields of 5 kV/cm and 50 kV/cm is shown on the lower part. For low fields, all models yield the same velocity profiles, which is an indication that the heated Maxwellian can be used. For high fields, a significant deviation of the velocity profiles can be observed.

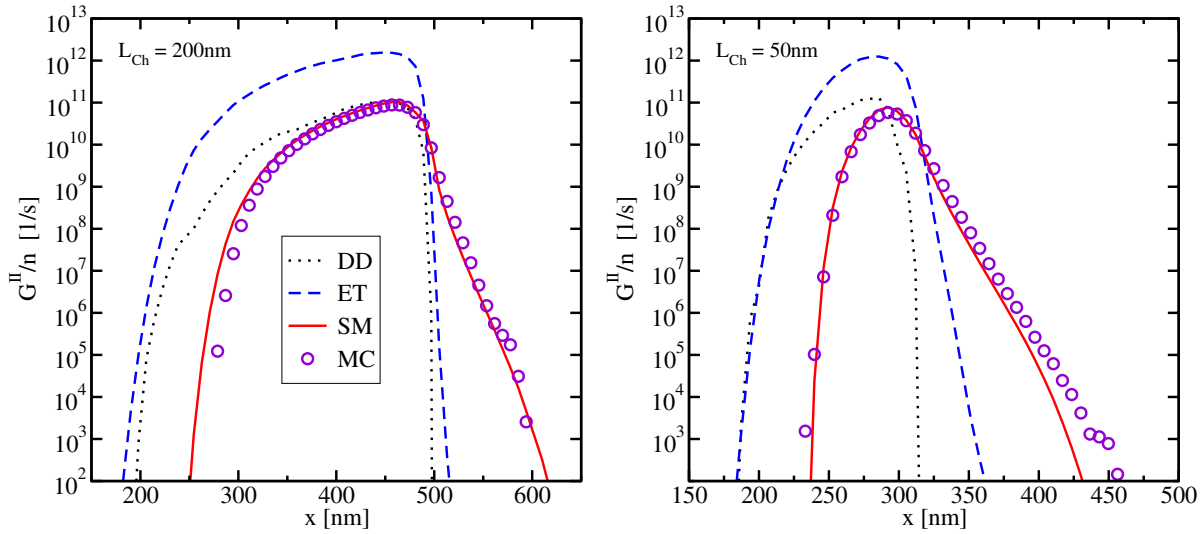


**Figure 3.13:** The impact ionization rate is calculated with MC, the DD, ET, and the SM model for a 200 nm and a 50 nm structure. Due to the better modeling of the distribution function in the SM model, the results are closer to the MC data than the DD and the ET model (after [5]).

parameters. For higher-order transport models, the error in the SVO decreases. This is shown in Fig. 3.14.

Here, the evolution of the velocity profile within several  $n^+n^+$  structures calculated with the DD, ET, SM, and the SHE as a reference, is presented. An electric field of 50 kV/cm in the middle of the channel of each device has been assumed. For long channel devices, all models yield more or less the same velocity profile, while for decreasing channel lengths, the SVO in the ET model and the reduced one in the six moments model are clearly visible. The velocity of the ET model increases very fast for decreasing channel lengths and is four times as high as the results obtained from SHE simulations at  $L_{Ch} = 15$  nm. On the other hand, the DD model does not predict any velocity overshoot and stays always under the saturation velocity  $v_{sat}$  of the bulk. The SM model predicts a velocity profile closer to the SHE data than the DD and the ET model, due to the advanced description of the high-energy part of the distribution function, following that the closure relation of the SM model is improved compared to the ET model. One of the consequences is that the SVO is reduced in the SM model. Therefore, with a better description of the closure relation and the transport parameters, the SVO would disappear as demonstrated in Fig. 3.15. Here, the velocity profile of the ET model is presented, considering closure relations and relaxation times based on MC simulations. As can be observed, the SVO in the ET model disappears, which justifies the above mentioned assumption. The better modeling of device characteristics within higher-order moments is also reflected in the currents, which is pointed out in Fig. 3.16. Here, the output characteristics of a 40 nm and 80 nm channel length  $n^+n^+$  structure calculated with the DD, ET, SM, and the reference SHE model are shown. While the relative error of the current calculated with the SM and the ET model stays more or less constant in long channel devices (see Fig. 3.5), there is a significant deviation of this pattern in the error in short channel devices.

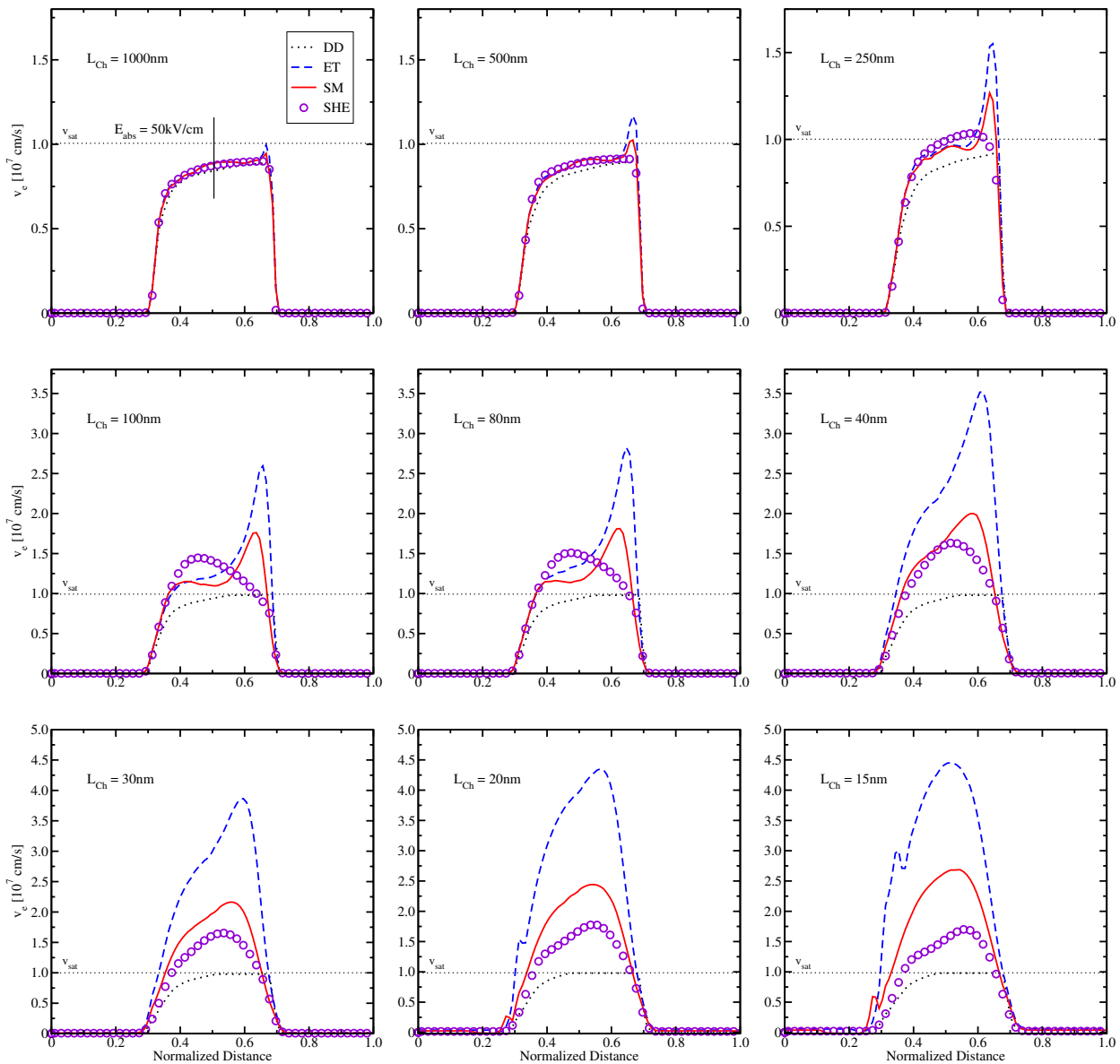


**Figure 3.14:** Evolution of the carrier velocity profiles for decreasing channel lengths calculated with the DD, ET, and the SM model. The velocities are compared to the results obtained from SHE simulations. While the maximum velocity of the DD model is the saturation velocity  $v_{\text{sat}}$ , the spurious velocity overshoot at the end of the channel in the ET and the SM model is clearly visible. The velocity overshoot at the beginning of the channel can be quantitatively identified at the 100 nm device in the ET and the SM model.

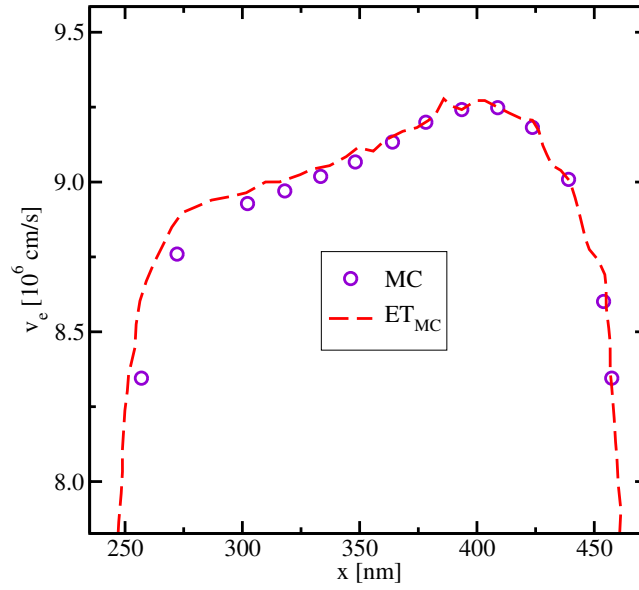


**Figure 3.15:** Velocity profile calculated with ET model and MC data. Due to the MC closure in the ET model for the fourth order moment and due to the improved modeling of the transport parameters, the spurious velocity overshoot at the end of the channel disappears (after [6]).

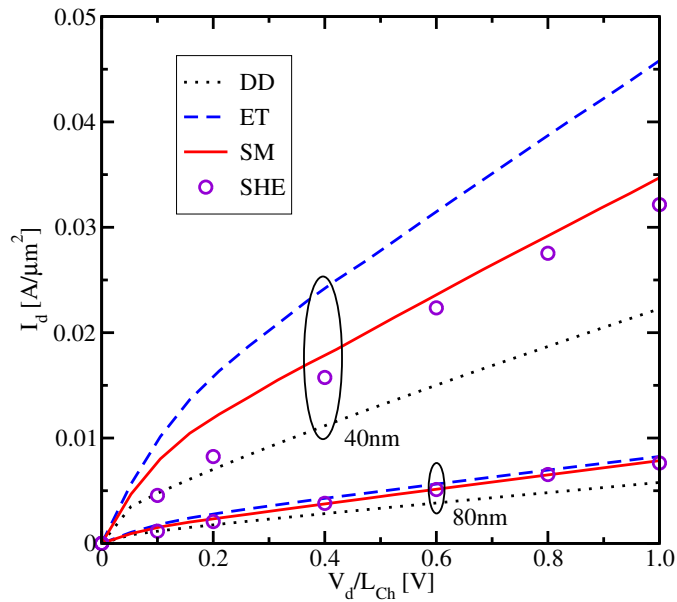


**Figure 3.16:** Output currents of a 80 nm and a 40 nm channel length  $n^+n^+$  structure calculated with the DD, ET, SM, and SHE model. The ET model overestimates the current at 40 nm, while the SM model yields the most accurate result.

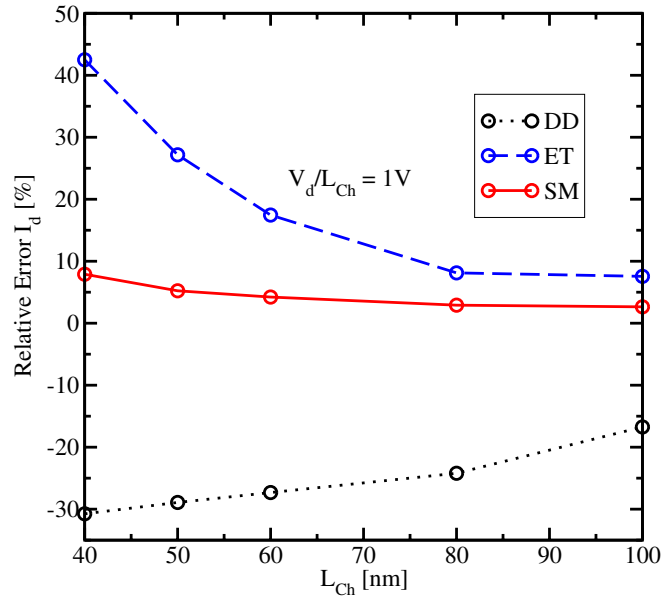


**Figure 3.17:** Relative error in the current of the DD, ET, and the SM model for an  $n^+nn^+$  structure in the channel range from 100 nm down to 40 nm. While the relative error of the SM model is below 6%, the error of the DD and the ET model is at  $-30\%$  and  $40\%$  for a channel length of 40 nm, respectively.

In the short channel range from 40 nm to 100 nm the current calculated with the SM model is below an error of 10%, while the errors of the DD and the ET model are at  $-30\%$  and  $40\%$  for a channel length of 40 nm, respectively (see Fig. 3.17).

As has been pointed out, the ET model is accurate down to a channel length of 80 nm, while a strong increase of the current error can be observed below 80 nm. Therefore, the ET model is a suitable transport model for devices down to 80 nm channel lengths only. However, with channel length below 80 nm the SM model is the model of choice. The strength of the six moments model is that the model gives more informations about the distribution function than the ET model.

'If you can't explain it simply, you don't understand it well enough.'

Albert Einstein

## Chapter 4

---

# Homogeneous Transport in Inversion Layers

---

WITH CONTINUOUSLY downscaling of the device geometry, the influence of quantum mechanical effects on the device characteristics starts to increase. Transport parameters are fundamentally affected by surface roughness scattering [146,147] and quantization [148]. In [149], surface roughness scattering has been approximated using the semi-empirical *Matthiesen* rule. However, the influence of inversion layer effects on higher-order transport parameters has not been studied satisfactorily yet. To point out the impact of these effects on the transport parameters, a self-consistent SMC simulator has been developed. The object of investigations is a homogeneous bulk UTB SOI MOSFET, where the impact of inversion layer effects on the carrier transport is very high.

### 4.1 Subband Monte Carlo Model

Investigations of inversion layer effects using the SMC simulations, have already been given in numerous publications [150–152]. However, a description concerning higher-order transport parameters in the inversion layer, which is important for the characterization of macroscopic transport in realistic devices, has not been done satisfactorily yet.

In order to study the influence of quantization and surface roughness scattering on higher-order transport parameters within high-fields, a self-consistent SMC simulator has been developed [50, 153, 154] (see sketch in Fig. 4.1).

Subband energy levels and wavefunctions are initially determined self-consistently with the *Poisson* equation assuming *Fermi–Dirac* statistics. Based on the subband structure, Monte Carlo calculations are performed taking into account phonon induced, impurity and surface roughness scattering. The non-parabolicity of the band structure is treated by *Kane's* model [70]. The scattering rates are strongly affected by high driving fields, which results in a shift of the wavefunctions. The consequence of this shift is a change in the overlap integral of the scattering operator and therefore a change in the subband occupations, which leads to a modified carrier

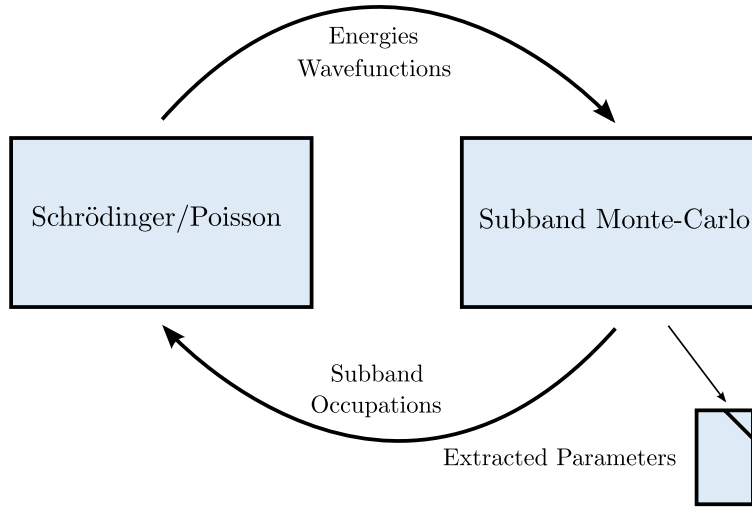


**Figure 4.1:** Principle data flow of the parameter extraction for higher-order transport models. While transport is treated in the SMC code, the influence of the confinement perpendicular to the oxide interface is carried out by the *Schrödinger-Poisson* solver.

concentration. This concentration can be obtained as

$$\begin{aligned}
 n_{\text{tot}}(z) = & 2 \sum_n \int_0^\infty \frac{m_t^*}{\pi \hbar^2} f(\mathcal{E} + \mathcal{E}_n - \mathcal{E}_f) \psi_n^2(z) d\mathcal{E} + 2 \sum_{n'} \int_0^\infty \frac{\sqrt{m_t^* m_l^*}}{\pi \hbar^2} f(\mathcal{E} + \mathcal{E}_{n'} - \mathcal{E}_f) \psi_{n'}^2(z) d\mathcal{E} \\
 & + 2 \sum_{n''} \int_0^\infty \frac{\sqrt{m_t^* m_l^*}}{\pi \hbar^2} f(\mathcal{E} + \mathcal{E}_{n''} - \mathcal{E}_f) \psi_{n''}^2(z) d\mathcal{E}.
 \end{aligned} \tag{4.1}$$

The subband occupation number is represented by the *Fermi-Dirac* distribution function  $f$ . After convergence is reached, which is achieved by an exchange of energy eigenvalues, wavefunctions, and subband occupations, the transport parameters can be extracted.

In Fig. 4.2, a result of the self-consistent loop between the *Schrödinger-Poisson* solver and the MC simulator is presented. Several velocities for different inversion layer concentrations  $N_{\text{inv}}$  as a function of the lateral field for a UTB SOI MOSFET device with a channel thickness of 4 nm and a substrate doping of  $2 \times 10^{16} \text{ cm}^{-3}$  have been extracted.

## 4.2 Surface Roughness Scattering

Surface roughness scattering (SRS) is the main scattering process in high inversion layer concentrations, which has a strong impact on the transport parameters (see Fig. 4.3). Surface roughness can be seen as a barrier at the interface, whose position has a small and slowly varying displacement  $\Delta_r$ . Here,  $\mathbf{r}$  is the two-dimensional vector in the plane of the interface [47].

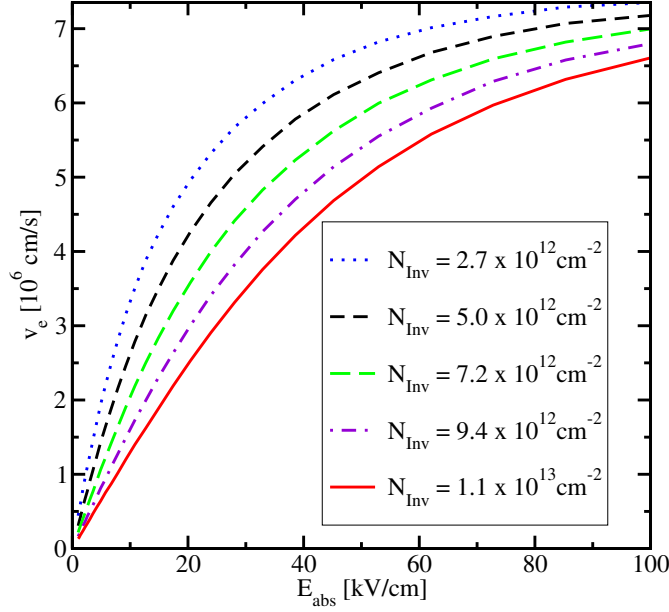


**Figure 4.2:** Carrier velocity as a function of the driving field for different inversion layer concentrations. Due to surface roughness scattering, the carrier velocity decreases for increasing inversion layer concentrations. The maximum velocity is below the saturation velocity of bulk Si.

$\Delta_{\mathbf{r}}$  can be expressed by its *Fourier* components

$$\Delta_{\mathbf{r}} = \sum_{\mathbf{q}} \Delta_{\mathbf{q}} \exp(i\mathbf{q}\mathbf{r}), \quad (4.2)$$

whereas the power spectrum  $\langle |\Delta_{\mathbf{q}}|^2 \rangle$  is usually modeled with a *Gaussian* form as [155]

$$\langle |\Delta_{\mathbf{q}}|^2 \rangle = \pi \Delta^2 \Lambda^2 \exp(-\mathbf{q}^2 \Lambda^2 / 4), \quad (4.3)$$

or with an exponential shape as described in [156, 157].  $\mathbf{q}$  is the difference between the incoming wavevector  $\mathbf{k}$  and the wavevector  $\mathbf{k}'$  after the scattering event.  $\Lambda$  is the correlation length of the oxide thickness fluctuations and should be understood as the minimum distance between two points at which thicknesses are considered independent. The SRS matrix elements  $V_{\mathbf{k}\mathbf{k}'}^{\text{SRS}}$  have been defined and discussed in [158] as

$$V_{\mathbf{k}\mathbf{k}'}^{\text{SRS}} = \frac{\hbar^2}{2m} \Delta_{\mathbf{k}-\mathbf{k}'} \left. \frac{d\psi_n^*}{dx} \frac{d\psi_{n'}}{dx} \right|_{x=0}. \quad (4.4)$$

Therefore, the derivative of the wave function at the interface plays an important role. The quantization direction in equation (4.4) is in  $x$  direction. In [47] it has been shown that the scattering potential depends linearly on the inversion layer concentration  $N_{\text{inv}}$  defined as [1, 47]

$$N_{\text{inv}} = g_v \left( \frac{\sqrt{m_t^* m_l^*}}{\pi \hbar^2} \right) k_B T_n \ln \left( 1 + \exp \left( \frac{\mathcal{E}_f - \mathcal{E}_i}{k_B T_n} \right) \right), \quad (4.5)$$



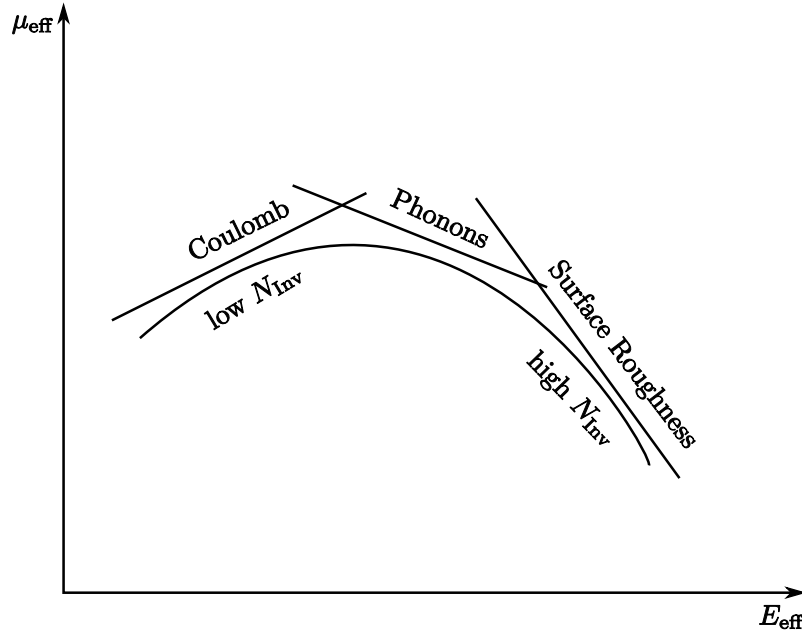


**Figure 4.3:** The effective mobility as a function of the effective field [7]. For increasing bulk doping and for low inversion layer concentrations *Coulomb* scattering is the main scattering process, while for increasing  $N_{\text{inv}}$  phonon scattering becomes more important.

and on the depletion concentration  $N_{\text{dep}}$  which can be expressed as [7]

$$N_{\text{dep}} = \left( 4N\epsilon_{\text{Si}} \frac{k_{\text{B}}T_{\text{L}}}{q^2} \ln \left( \frac{N}{n_{\text{i}}} \right) \right)^{1/2}. \quad (4.6)$$

$N$  and  $n_{\text{i}}$  denote the substrate and the intrinsic concentration, respectively. The influence of this dependence on higher-order transport parameters will be shown in the sequel. Inserting the scattering matrix into *Fermi's* golden rule (see equation (2.137)) and integrating over the whole space, the SRS time  $\tau_{\text{SR}}$  can be written as [47]

$$\frac{1}{\tau_{\text{SR}}} = \frac{2\pi}{\hbar} \sum_{\mathbf{k}'} \langle |\Delta_{\mathbf{k}-\mathbf{k}'}^2| \rangle \left( \frac{V_{\mathbf{k}\mathbf{k}'}^{\text{SRS}}}{\Delta_{\mathbf{k}-\mathbf{k}'} \mathcal{E}(\mathbf{k}-\mathbf{k}')} \right)^2 (1 - \cos(\theta_{\mathbf{k}\mathbf{k}'})) \delta(\mathcal{E}(\mathbf{k}) - \mathcal{E}(\mathbf{k}')). \quad (4.7)$$

With a large correlation length  $\Lambda$ , the interface is locally flat and therefore the term  $\langle |\Delta_{\mathbf{k}-\mathbf{k}'}^2| \rangle$  tends to zero, which means that the surface roughness scattering is not effective. For small  $\Lambda$  the relaxation time is determined by the product of  $\Delta$  and  $\Lambda$  (see equation (4.3)). In fact, for relatively small correlation lengths, a considerable scattering rate is observed, if the amplitude of thickness variations  $\Delta$  is high enough. The energy in the denominator of the expression  $V_{\mathbf{k}\mathbf{k}'}^{\text{SRS}}/\Delta_{\mathbf{k}-\mathbf{k}'} \mathcal{E}(\mathbf{k}-\mathbf{k}')$  reflects the fact that scattering with small wave vectors predominates,  $(1 - \cos(\theta_{\mathbf{k}\mathbf{k}'}))$  is the essential component entering the relaxation time [1], while the delta function is related to the elastic nature of the process.

### 4.3 Influence of Surface Roughness Scattering on Higher-Order Transport Parameters

The main differences between bulk transport and transport in an inversion layer is the occurrence of quantum mechanical effects such as quantum confinement, subbands and SRS. Due to quantum confinement, carriers cannot move in the direction perpendicular to the interface. Thus, carriers have to be treated as a two-dimensional gas, which has a considerable impact on the transport properties.

In Fig. 4.4, higher-order mobilities as a function of the inversion layer concentration  $N_{\text{inv}}$  are shown. In a bulk MOSFET within low fields, the carrier mobility  $\mu_0$  fits the measurement data of Takagi [7,159] quite well, while a significant reduction is observed in the quantized 4 nm channel region of a UTB SOI MOSFET [160]. A considerable deviation of higher-order mobilities for

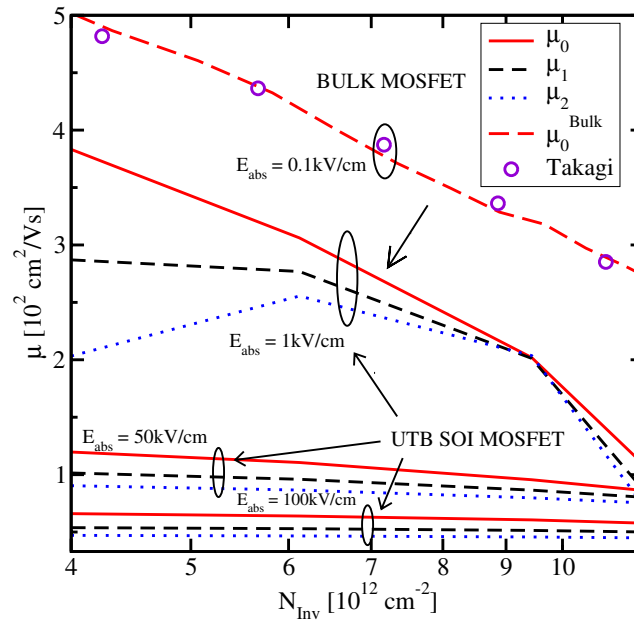


**Figure 4.4:** Higher-order mobilities as a function of the inversion layer concentration  $N_{\text{inv}}$  for different lateral fields. For high fields the difference of the mobilities decreases. For low fields in a bulk MOSFET the carrier mobility is equal to the measurement data of Takagi.

low  $N_{\text{inv}}$  and low fields can be observed, while for high fields this deviation disappears. All mobilities are constant for high fields and are not affected anymore by SRS. The reason for the constant mobilities for high fields can be explained with Fig. 4.5 and Fig. 4.6.

In Fig. 4.5 the conduction band edge for several  $N_{\text{inv}}$  is presented. Due to the band bending for increasing  $N_{\text{inv}}$ , the carriers move closer to the interface, and therefore the influence of SRS becomes stronger, which results in a lowering of the mobilities. For high fields, the distance of the carriers to the interface increases, which reduces the influence of SRS on the mobilities.

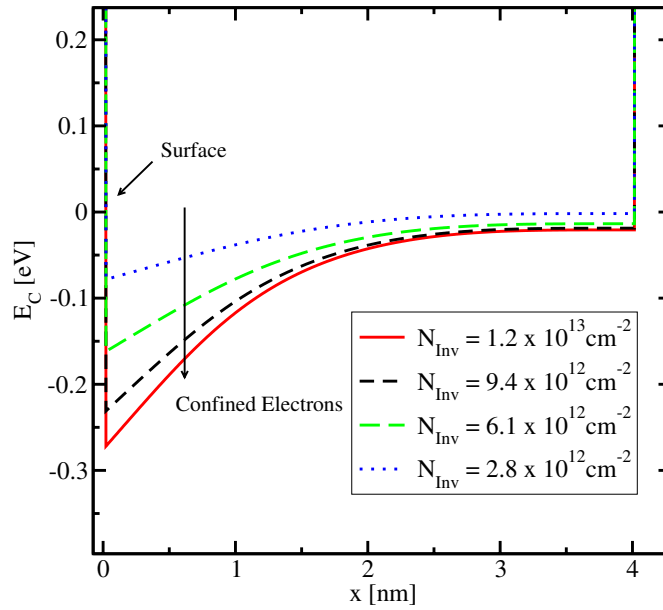


**Figure 4.5:** Conduction band edge as a function of the position for different inversion layer concentrations. For high  $N_{\text{inv}}$ , the carriers are closer to the interface and hence they are more affected by surface roughness scattering than for low  $N_{\text{inv}}$ .

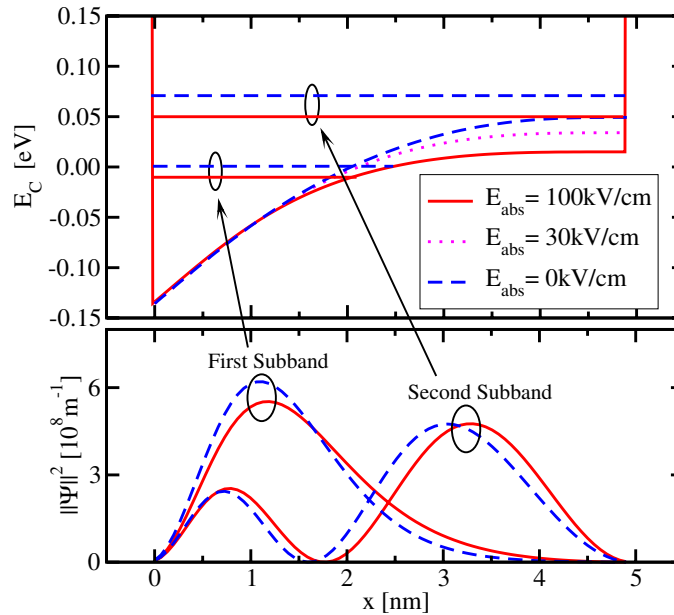


**Figure 4.6:** Conduction band and wavefunctions of a UTB SOI MOSFET for different electric fields. Both the wavefunctions and subbands are shifted with increasing lateral electric fields. The conduction band edge is affected by the change in the subband occupations.

This is demonstrated in Fig. 4.6. Here, the behavior of the conduction band edge together with the first two subbands and their wavefunctions for different driving fields of 30 kV/cm and 100 kV/cm is presented. As pointed out before, there is a shift of the conduction band edge and subbands to lower values for increasing driving fields. The result of this band edge shift is that the wavefunction is shifted away from the interface, which means that the probability of finding a carrier near the interface decreases. As a consequence, the influence of surface characteristics on the transport parameters decreases as well. Therefore, the effect of SRS on the mobilities is drastically reduced for high fields.

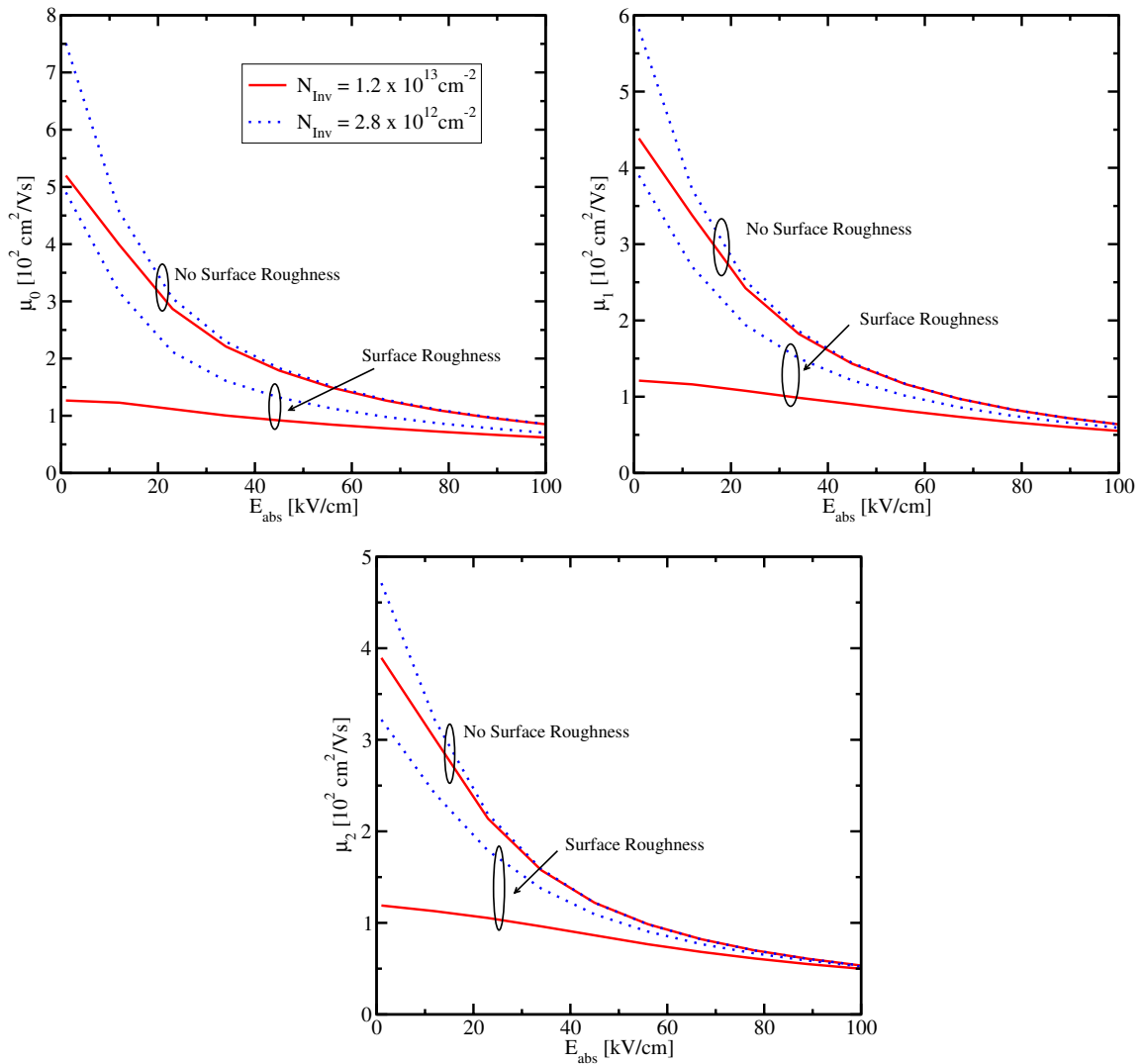


**Figure 4.7:** Influence of surface roughness scattering on  $\mu_0$ ,  $\mu_1$ , and  $\mu_2$  as a function of the lateral field for different  $N_{\text{inv}}$ . For low fields, surface roughness scattering has a strong impact, while for high fields the mobilities are unaffected by SRS.

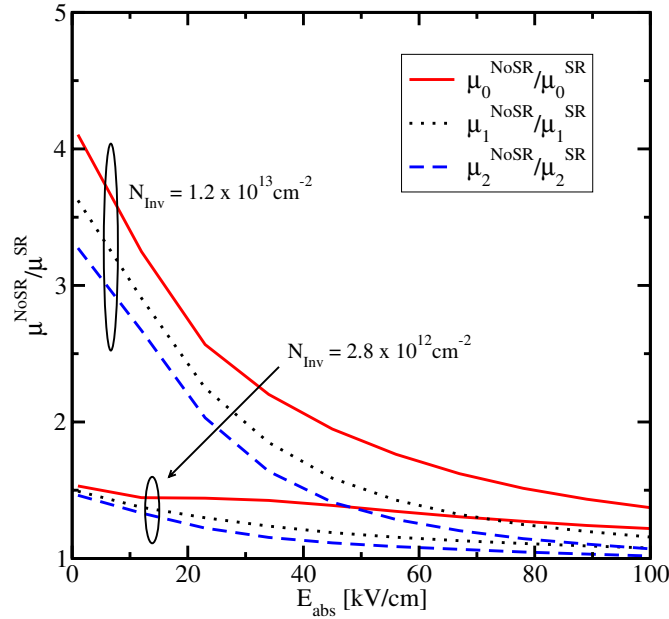


**Figure 4.8:** Ratio between the mobilities neglecting and considering SRS for high and low  $N_{inv}$  values as a function of the lateral field. For low  $N_{inv}$ , the mobilities are unaffected. The carrier mobility is more affected by SRS than the higher-order mobilities.

This is visible in Fig. 4.7. Here, higher-order mobilities as a function of the electric field for different inversion layer concentrations have been calculated both with and without surface roughness scattering. For fields above 120 kV/cm, the effect of surface roughness scattering on the carrier mobility can be neglected, while for the energy flux mobility and the second-order energy flux mobility even at 100 kV/cm the scattering process has only a minor impact. Thus, higher-order mobilities are not so much affected by SRS as the carrier mobility.

This is demonstrated in Fig. 4.8, where the ratios of higher-order mobilities with and without SRS for high and low inversion layer concentrations of  $1.2 \times 10^{13} \text{ cm}^{-2}$  and  $2.8 \times 10^{12} \text{ cm}^{-2}$ , respectively, are plotted. The difference in the low  $N_{inv}$  regime between the ratio curves of  $\mu_0$  and the higher-order mobilities is not as high as in the strong inversion regime. This can be explained as follow: Surface roughness scattering changes the momentum relaxation time  $\tau_0$  and therefore the velocity, which is proportional to  $\tau_0$ , is shifted to lower values for increasing  $N_{inv}$  (see Fig. 4.10). Therefore, the antisymmetric part of the distribution function is reduced for high inversion layer concentrations following that the distribution function becomes more isotropic. The effect is that the impact of SRS on the energy flux is not as high as on the carrier flux. This is pointed out in Fig. 4.9, where the ratio of the momentum relaxation time and the energy-flux relaxation time  $\tau_3$  is presented. Due to the strong increase for high  $N_{inv}$  of  $\tau_0$  compared to  $\tau_3$ , the higher-order mobilities, which are proportional to the relaxation times, are not as affected by SRS as  $\mu_0$ . The dependence of  $\mu_0$  on  $N_{inv}$  has an impact on the carrier velocity as pointed out in Fig. 4.10. There, the velocity for high inversion layer concentration and low inversion layer concentration is shown. The difference in the high field case between the carrier velocities considering once SRS and neglecting SRS for the high inversion layer concentration case is about 25 %, while the velocities in the high and low  $N_{inv}$  neglecting SRS respectively, yield the same result.

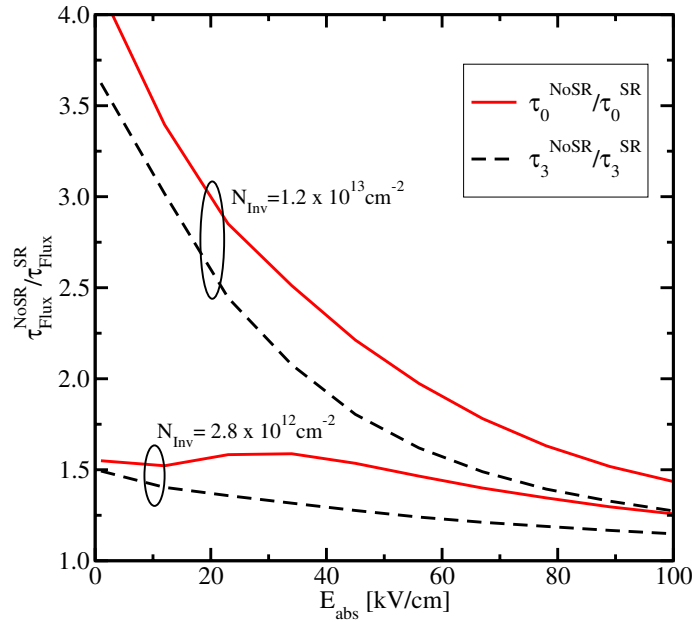


**Figure 4.9:** Ratio of the momentum relaxation time  $\tau_0$  and energy flux relaxation time  $\tau_3$  for different  $N_{\text{inv}}$  as a function of the driving field. Surface roughness scattering influences  $\tau_0$  more than  $\tau_3$ , especially for high inversion layer concentrations.

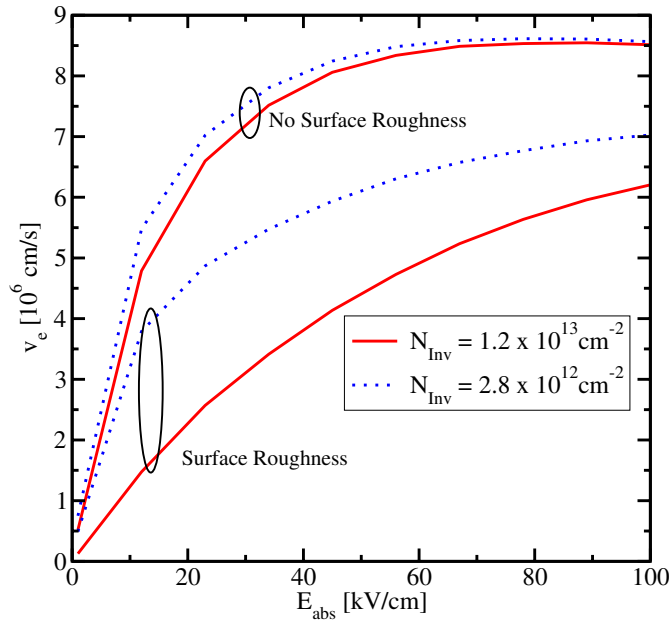


**Figure 4.10:** Influence of surface roughness scattering on the electron velocities for different  $N_{\text{inv}}$ . For decreasing  $N_{\text{inv}}$ , SRS loses the influence on the carrier velocity. Due to non-parabolic bands and quantization, the velocity is below the saturation velocity of the bulk.

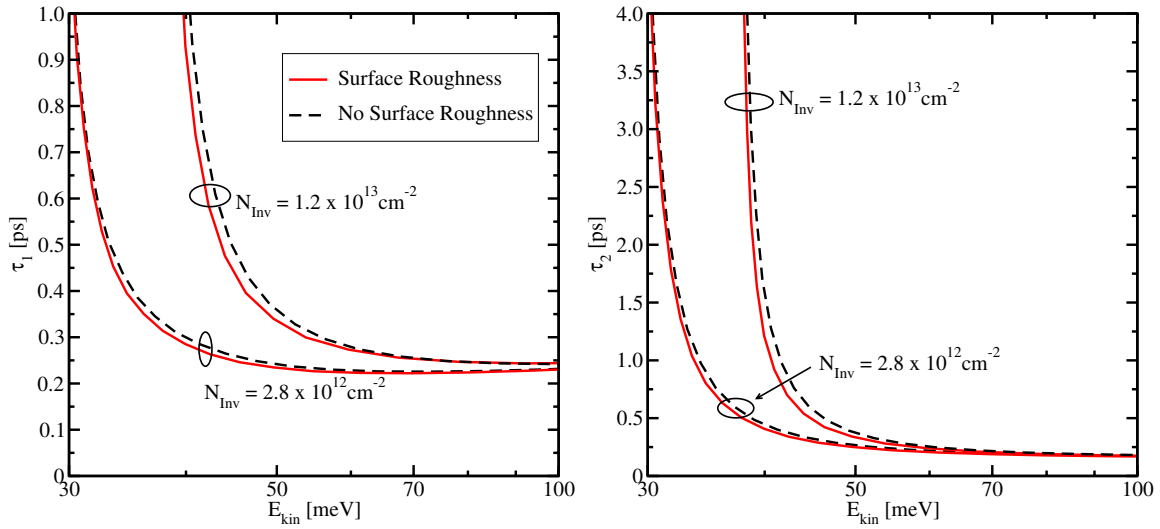


**Figure 4.11:** Influence of surface roughness scattering on  $\tau_1$  and  $\tau_2$  as a function of the kinetic energy of the carriers for different  $N_{inv}$ . Due to the elastic scattering nature of SRS, the relaxation times are not affected by SRS.

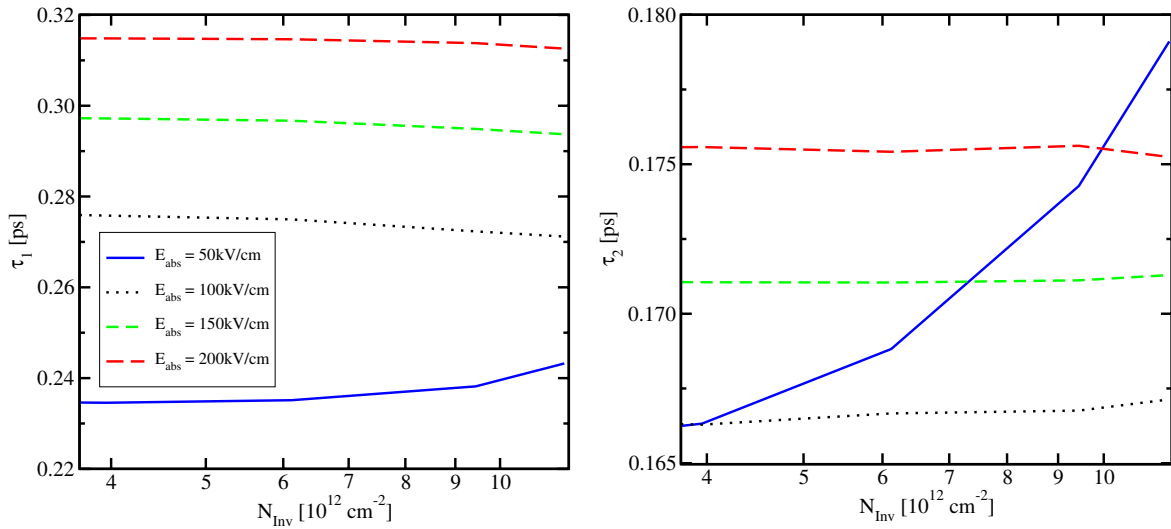


**Figure 4.12:** Energy relaxation time (left side) and the second-order relaxation time (right side) as a function of the inversion layer concentration for different lateral electric fields. For a field of 50 kV/cm and high  $N_{inv}$ ,  $\tau_1$  and  $\tau_2$  increase in contrast to high-fields, where the energy relaxation time remain constant.

Fig. 4.11 shows the energy relaxation time and the second-order relaxation time as a function of the kinetic energy of the carriers for low and high inversion layer concentrations considering and neglecting SRS. Due to the elastic nature of SRS, there is no change in the energy relaxation time and in the second-order relaxation time.

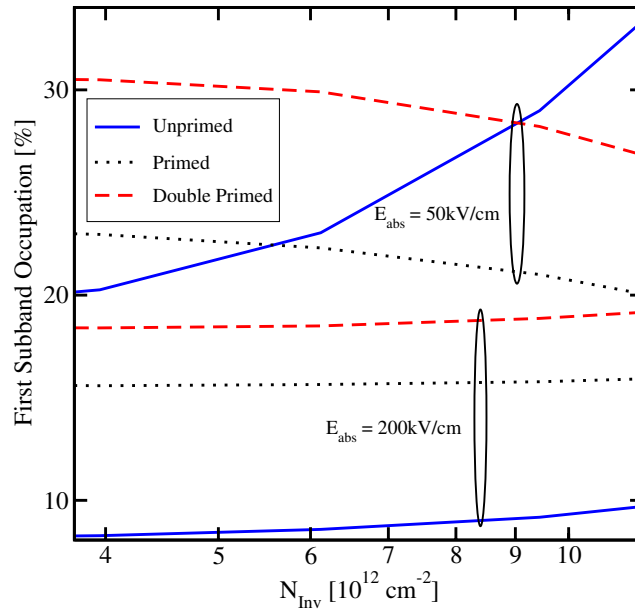
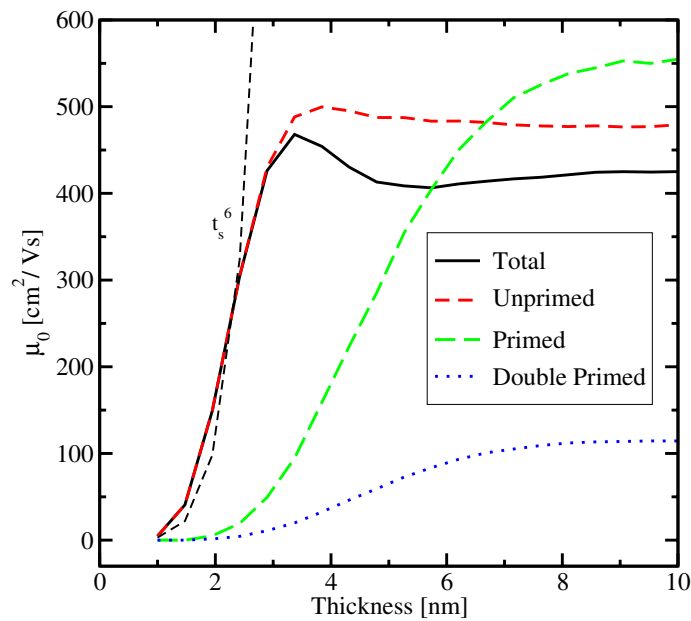


**Figure 4.13:** First subband occupation of the unprimed, primed, and double primed valleys as a function of the inversion layer concentration for fields of 50 kV/cm and 100 kV/cm. Due to the light mass of the unprimed valley in transport direction, the subband occupation number is higher than in the other valleys.

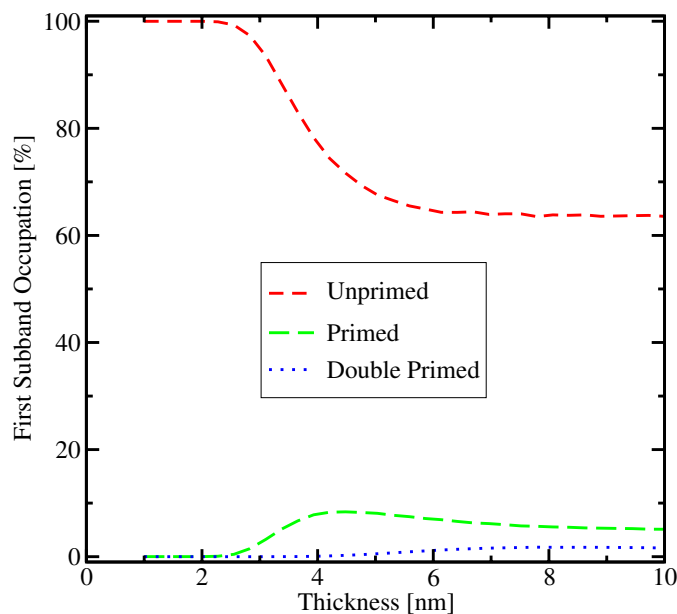
In Fig. 4.12,  $\tau_1$  and  $\tau_2$  as a function of  $N_{inv}$  for different lateral electric fields are presented. As can be observed, the relaxation times for high fields are constant except for a lateral field of 50 kV/cm. There is a significant change in the second-order relaxation time. This can be explained with Fig. 4.13, where the first subband occupation as a function of  $N_{inv}$  of the unprimed, primed, and double primed valleys for lateral fields of 50 kV/cm, and 200 kV/cm is shown. Due to the fast increase of the occupation number of the first subband in the unprimed valley at 50 kV/cm compared to the high-field case, where the occupation is constant, the change in the second-order relaxation times increases as well for high  $N_{inv}$ .

Fig. 4.14 demonstrates the mobilities in each valley and the total average mobility as a function of the channel thickness. The mobilities are indirectly proportional to the effective masses. As has been pointed out in Fig. 2.10, the velocity of the unprimed valley is high compared to the primed and double primed valleys. This is due to the light conduction mass of the unprimed valley and therefore the mobility is also high compared to the other valleys. The maximum peak in the total average mobility is due to a high occupation of the unprimed ladder for a thickness of 2 nm as demonstrated in Fig. 4.15. By increasing the channel thickness to 3 nm, the occupation of the unprimed valley decreases and the occupation of the primed valley with the heavy conduction mass increases. The total mobility curve has a minimum at about 4 nm bulk thickness. At this value, the occupation of the primed valley has its maximum. After the occupation of the double primed valley starts to increase, the total mobility increases too, until the occupation numbers of each valley reach a saturation value. Furthermore, it has been reported in [155] that for ultra thin body devices the carrier mobility is proportional to the device thickness to the power of six, which is in good agreement with the results.





**Figure 4.14:** Mobilities of the unprimed, primed, and double primed valleys, and total average mobility as a function of the channel thickness. At about 3 nm, there is a maximum in the total mobility. This is the point where the mobility of the unprimed valley is already high while the carrier mobility of the remaining valleys is low.



**Figure 4.15:** Populations of the unprimed, primed, and double primed valleys as functions of the channel thickness.

## 4.4 Comparison with Bulk Simulations

To point out just the influence of quantization on higher-order transport parameters, the subband results have been compared to three-dimensional bulk data. Surface roughness scattering has not been considered in these subband simulations.

In Fig. 4.16,  $\mu_0$ ,  $\mu_1$ , and  $\mu_2$  are compared to bulk simulations with a doping of  $10^{16} \text{ cm}^{-3}$ . As can be observed, the higher-order mobilities of the 2D electron gas are below the mobilities of the 3D bulk simulations, especially in the low field regime.

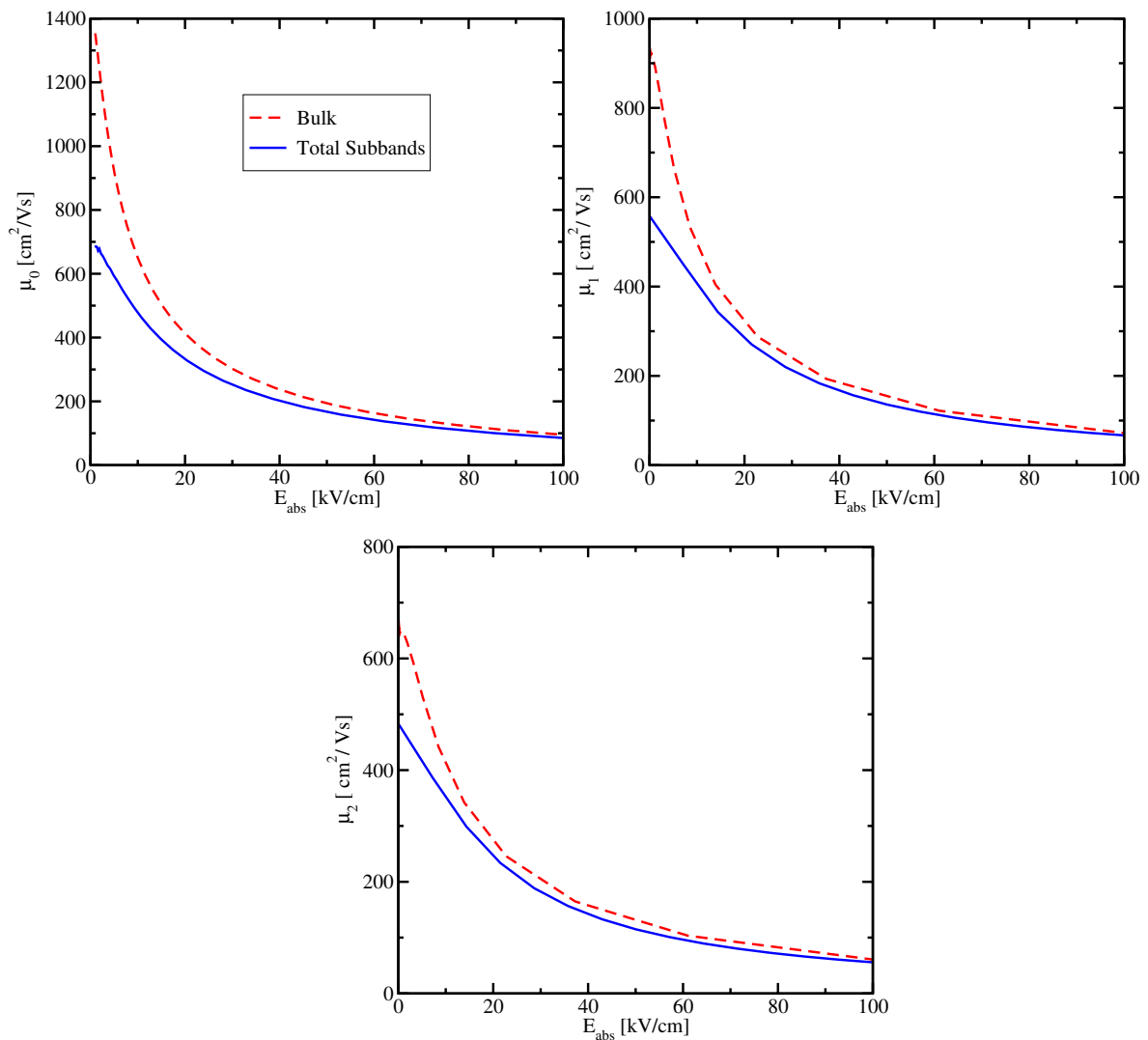


**Figure 4.16:** Carrier, energy-flux, and second-order energy flux mobility of SMC and bulk MC simulations. The mobilities obtained by bulk simulations are higher than in subband simulations. For high fields, the mobilities from subband simulations yield the same value as from bulk simulations.

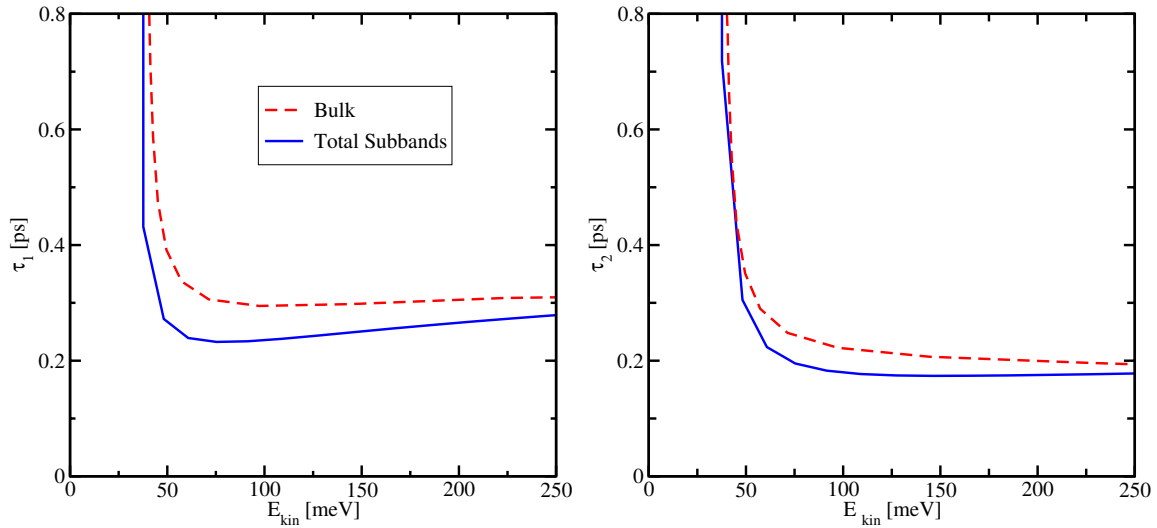


**Figure 4.17:** Comparison of the energy relaxation time and second-order energy relaxation time using 2D SMC data and 3D bulk MC data. For high energies both simulations converge to the same value.

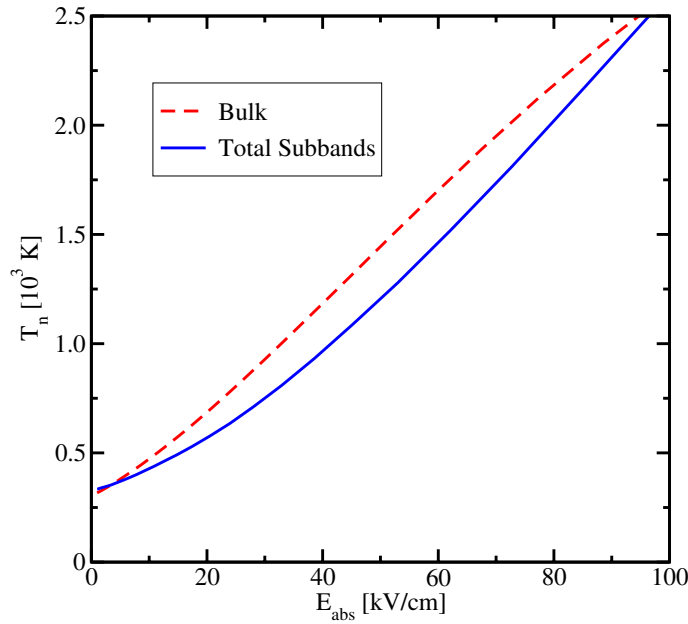
This behavior can be explained as follows: Due to *Heisenberg's* uncertainty principle, there is a wider distribution of momentum in the quantization area, because of a higher localization of the particles than in the bulk. Hence, there are more bulk phonons available that can assist the transition between electronic states. This will lead to an increase of the phonon rates and a decrease of the mobilities [161].

Due to the higher probability of scattering with phonons in the subband case, the energy relaxation time and the second-order energy relaxation time are lower than in the bulk as demonstrated in Fig. 4.17. This is also the case in the carrier temperatures as visualizes in Fig. 4.18.

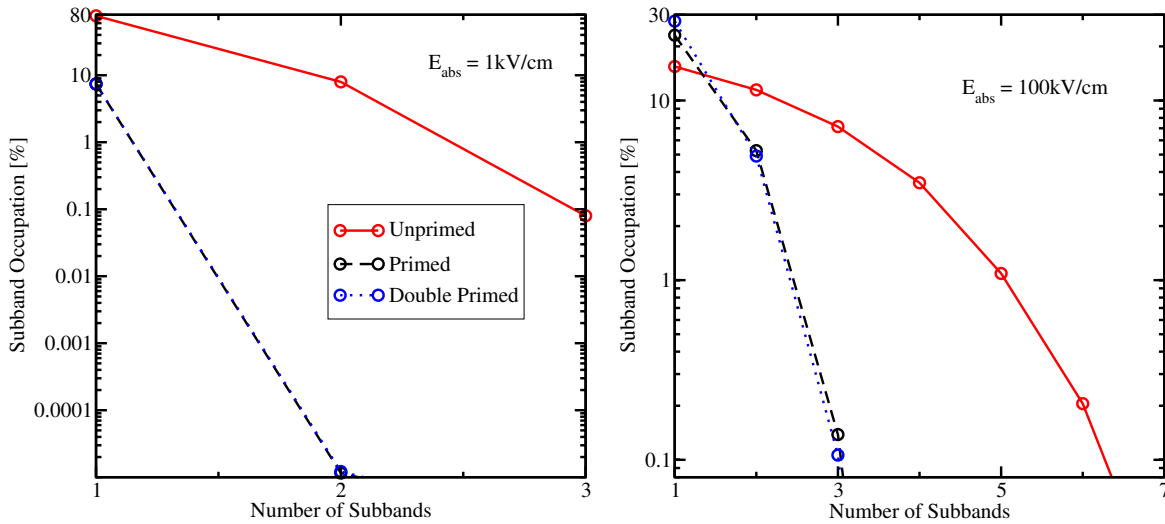
Here, the subband carrier temperature is below the bulk temperature due to the fact, that an increase of the phonon scattering probability decreases the carrier temperature. However, for high energies, the relaxation times and the temperatures of the subband simulations converge to the bulk results due to the occupation of higher subbands.

Fig. 4.19 shows the subband occupation as a function of the subband ladders for a low field and a high field. As pointed out, for an electric field of  $E = 1 \text{ kV/cm}$ , the first subband in the unprimed valley is highly occupied, while the ladders in the primed and double primed valleys are more or less unoccupied. The situation changes for a field of  $E = 100 \text{ kV/cm}$ . The carriers gain more energy, which results in the occupation of higher subbands. The occupation values of the first two ladders in the primed and double primed valleys are higher than in the unprimed valley.

A study of the influence of important inversion layer effects on higher-order transport parameters using the SMC method has been given. The investigations made in this chapter are based on a homogeneous bulk subband system, where all spatial gradients of the macroscopic transport models are negligible. The next chapter is devoted to higher-order transport models in real devices.



**Figure 4.18:** Comparison of the carrier temperature using 2D SMC data and 3D bulk MC data. Due to higher phonon scattering in the 2D case the temperature is lower than in the 3D case.



**Figure 4.19:** Subband occupations as functions of the subband ladders in the unprimed, primed, and double primed valleys for electric fields of 1 kV/cm and 100 kV/cm. For high fields, the subband ladders in the primed and double primed valleys are occupied.

*'Knowing is not enough; we must apply. Willing is not enough; we must do.'*

Johann W. von Goethe

## Chapter 5

---

# Subband Macroscopic Models

---

IN ORDER TO ACCURATELY describe carrier transport in the inversion layer of a whole device, a 2D non-parabolic macroscopic transport model up to the sixth order has been developed. To include inversion layer effects and to characterize high field transport, a special transport parameter extraction technique from SMC simulations has been carried out. Surface-roughness scattering as well as quantization are thus inherently considered in the SMC tables as described in the previous chapter. Now it is possible to specify higher-order mobilities as well as the macroscopic relaxation times as a function of the effective field. To verify the validity of the 2D macroscopic models, the results are benchmarked against device-SMC simulations. The models are applied to UTB SOI MOSFETs and their predictions are discussed for different channel lengths.

### 5.1 The Model

As shown in Fig. 5.1, the extracted higher-order transport parameters derived from SMC forms the base for a parameter interpolation within the channel of the device simulator. In the source and in the drain region the transport parameters are set as constant. The device simulator calculates the transverse effective field in the channel, which is the field perpendicular to the current flow defined as

$$E_{\text{eff}} = \frac{\int_0^C E_y n \, dy}{\int_0^C n \, dy}, \quad (5.1)$$

and extracts from the SMC tables the mobilities and relaxation times as a function of the effective field. The upper integration limit  $C$  of equation (5.1) is the channel thickness. The calculated effective field in Fig. 5.2 for different drain voltages  $V_d$  of 0.1 V, 0.25 V, and 0.5 V throughout a 40 nm channel length SOI MOSFET device are shown, while the extracted higher-order parameter-set from SMC simulations for different effective fields is presented in Fig. 5.3 and Fig. 5.4. The explicit equation-set of the 2D six moments model is given as

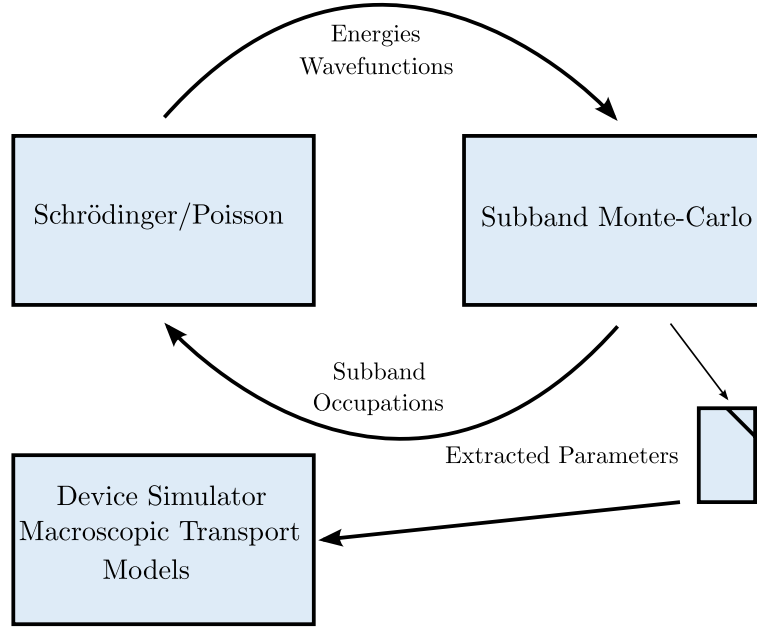


**Figure 5.1:** The SP-SMC loop describes the transport of a two-dimensional electron gas in an inversion layer. After convergency is reached, the device simulator utilizes the extracted parameters to characterize transport through the channel of the whole device.

$$\partial_t (nw_0) + \nabla_{\mathbf{r}} (n\mathbf{V}_0) = -R, \quad (5.2)$$

$$n\mathbf{V}_0 = -2\frac{\mu_0}{q}H_1\nabla_{\mathbf{r}}(nw_1) - s_{\alpha}n\mu_0w_0\nabla_{\mathbf{r}}\tilde{\varphi}, \quad (5.3)$$

$$\partial_t (nw_1) + \nabla_{\mathbf{r}} (n\mathbf{V}_1) + s_{\alpha}qn\mathbf{V}_0\nabla_{\mathbf{r}}\tilde{\varphi} + n\frac{w_1 - w_{10}}{\tau_1} = 0, \quad (5.4)$$

$$n\mathbf{V}_1 = -2\frac{\mu_1}{q}H_2\nabla_{\mathbf{r}}(nw_2) - s_{\alpha}n\mu_1(1 + 2H_1)w_1\nabla_{\mathbf{r}}\tilde{\varphi}, \quad (5.5)$$

$$\partial_t (nw_2) + \nabla_{\mathbf{r}} (n\mathbf{V}_2) + 2s_{\alpha}q\mathbf{V}_1\nabla_{\mathbf{r}}\tilde{\varphi} + n\frac{w_2 - w_{20}}{\tau_2} = 0, \quad (5.6)$$

$$n\mathbf{V}_2 = -2\frac{\mu_2}{q}H_3\nabla_{\mathbf{r}}(nw_3) - s_{\alpha}n\mu_2(1 + 4H_2)w_2\nabla_{\mathbf{r}}\tilde{\varphi}. \quad (5.7)$$

The closure relation of the 2D six moments model has been taken into account according to Fig. 2.15 as

$$w_3^{2D} = 6(k_B T_n)^3 \beta^{2.7}. \quad (5.8)$$

The behavior of the kurtosis  $\beta$  of the 2D six moments model through the channel of the UTB SOI MOSFET with a channel length of 100 nm, 60 nm, and 40 nm, respectively, is shown in Fig. 5.5. On the left side of Fig. 5.5, the second-order temperature  $\Theta = \beta T_n$  and the carrier temperature profile  $T_n$  is shown, while on the right side the kurtosis is presented. In the source region, the kurtosis equals unity in all three shown devices, while the kurtosis decrease down to 0.8

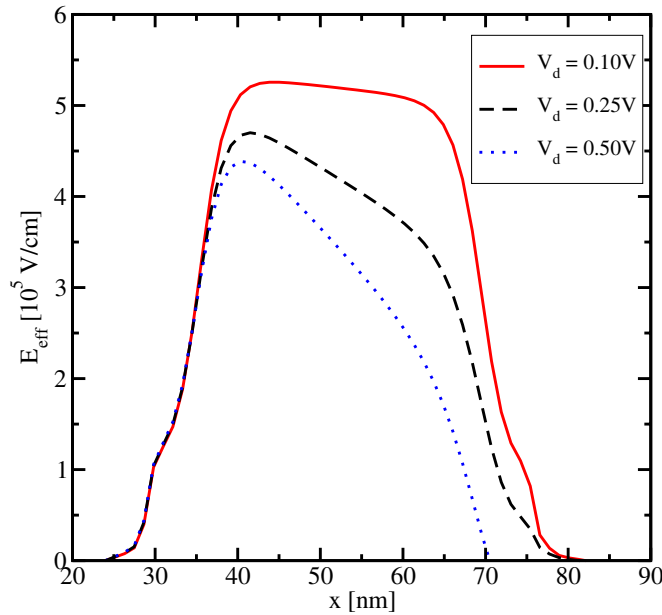


**Figure 5.2:** Effective field profile throughout the whole device for several bias points. With the effective fields and the SMC tables, higher-order transport parameters can be modeled as a function of the effective field.

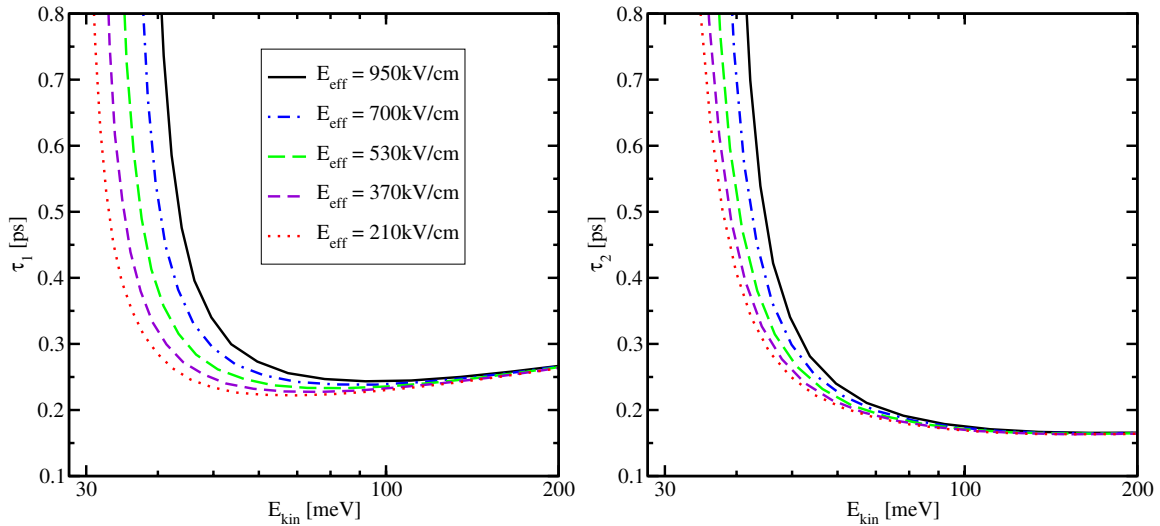


**Figure 5.3:** Energy relaxation time and second-order relaxation time for different effective fields as a function of the kinetic energy of the carriers. For high carrier energies, the relaxation times of the different inversion layers yield the same value.

at the end of the channel, which means that the heated *Maxwellian* overestimates the carrier distribution function in the channel also in the 2D model. Different values greater than one can be observed at the beginning of the drain region. While for the device with a channel length

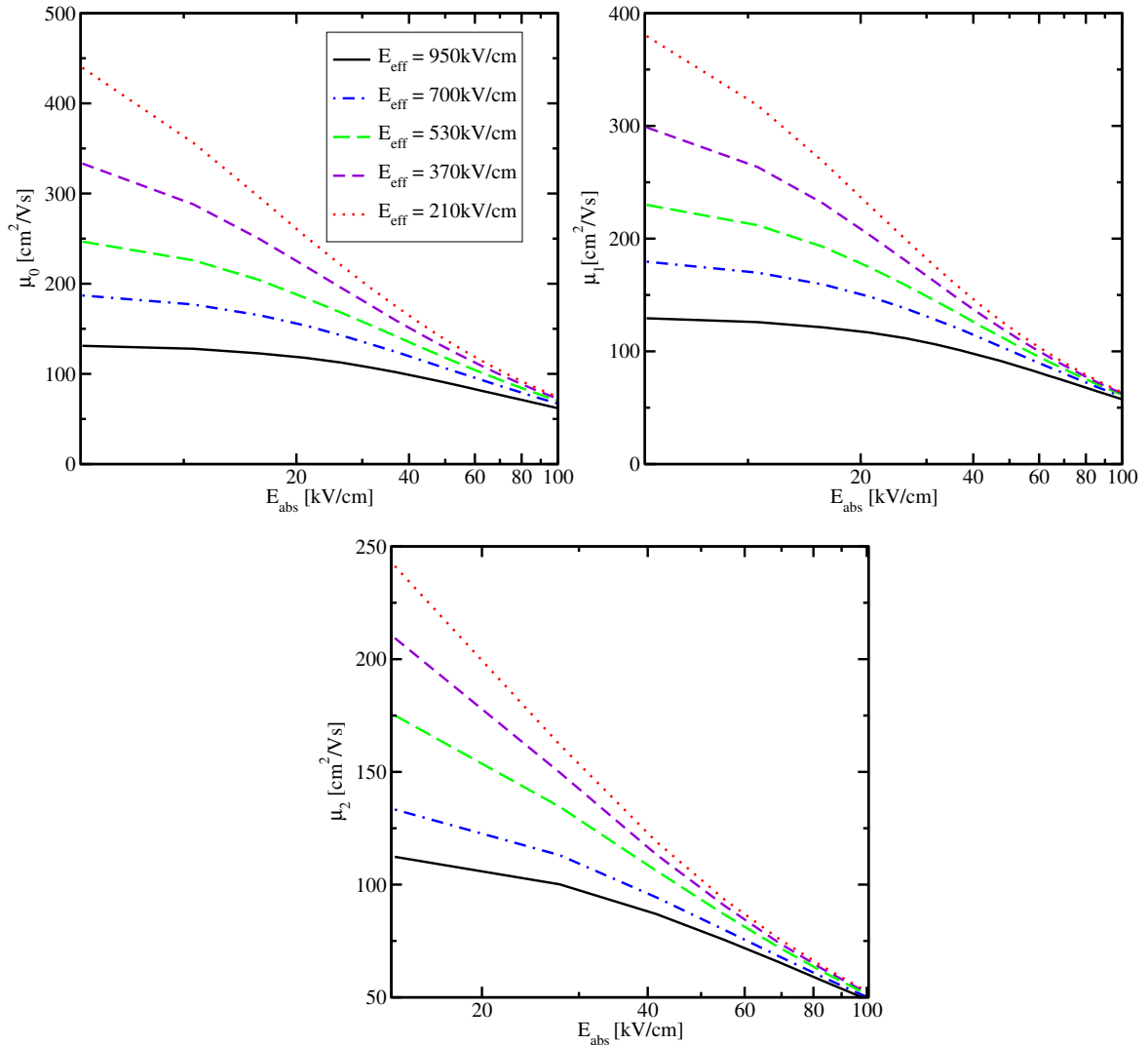


**Figure 5.4:** Carrier and higher-order mobilities for different effective fields as a function of the lateral field. For high fields the mobilities converge to the same value.

of 100 nm the value of the kurtosis is 1.55, the value increases up to 2 for the 40 nm channel length device. Therefore, for decreasing channel lengths, the kurtosis increases in the inversion layer as well, which is an indication of the increasing high energy tail of the distribution function.

In Fig. 5.6, the carrier temperature together with the second-order temperature profiles for drain voltages of 0.3 V and 1 V are plotted. For low fields, a good approximation of the carrier distribution function is the heated *Maxwellian*, while an increase of the kurtosis can be observed for high driving fields especially in the drain region.

## 5.2 The Quantum Correction Model

Quantum mechanical confinement has been considered in the classical device simulator using the quantum correction model IMLDA, which has been consistently calibrated to the *Schrödinger*-



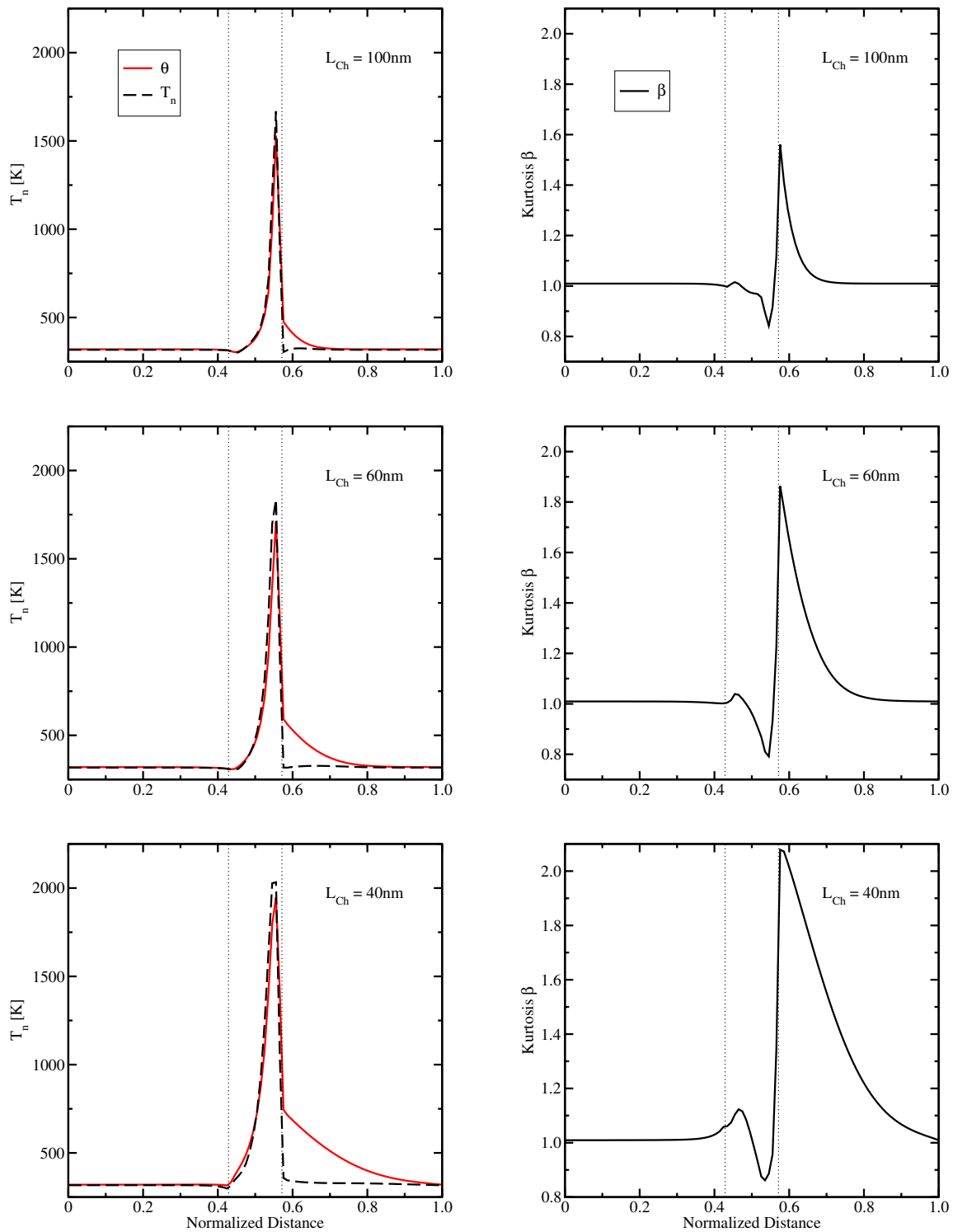


**Figure 5.5:** Second-order temperature  $\theta = \beta T_n$ , carrier temperature  $T_n$ , and kurtosis  $\beta$  for different SOI MOSFETs with channel lengths of 100 nm, 60 nm, and 40 nm. For decreasing channel lengths the kurtosis increases due to the increase of the high energy tail of the distribution function.

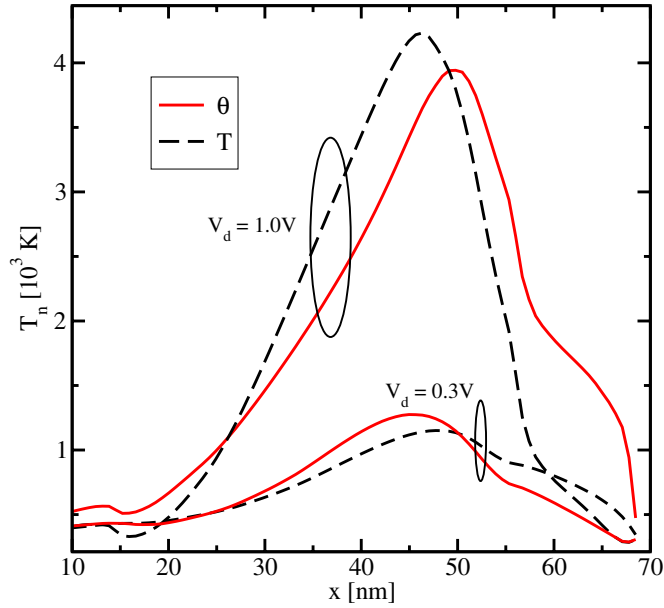


**Figure 5.6:** Temperature and second-order temperature profiles for different drain voltages. For the low drain voltage case, the second-order temperature yields a similar result compared to the carrier temperature, while a significant deviation between  $\theta$  and  $T_n$  especially in the drain region can be observed for high fields.

*Poisson* simulator used in the device-SMC simulator (DSMC) as demonstrated in Fig. 5.7 (see Section 2.3.4). A detailed description of the used DSMC simulator can be found in [148, 162, 163].

The CV-curves of SOI MOSFETs with different gate lengths of 80 nm, 60 nm, and 40 nm are calculated once with the SP solver used in the DSMC simulator and with the classical device simulator including the IMLDA model. As can be observed for high gate voltages both simulations yield the same capacitances and therefore we conclude that the IMLDA model approximates the quantum confinement very well. In the following simulations, a gate voltage of 1.3 V is applied. The importance of the quantum correction model is pointed out in Fig. 5.8. Here, the output current is calculated with the DD, ET, SM, and as a reference with device-*Subband Monte Carlo* data of a 40 nm channel length SOI MOSFET. In the macroscopic models the calibrated quantum correction model has been considered. As can be clearly seen, the SM model predicts an output current very close to the DSMC result, while the ET model overestimates the current and the DD model is below the DSMC result. All currents of the macroscopic models are shifted to higher values when the quantum correction model is neglected. Thus, in order to have a reasonable comparison between the 2D macroscopic transport models and the DSMC simulator, where the *Schrödinger* equation is directly solved, the quantum correction model is very important, as will be demonstrated in the next section.

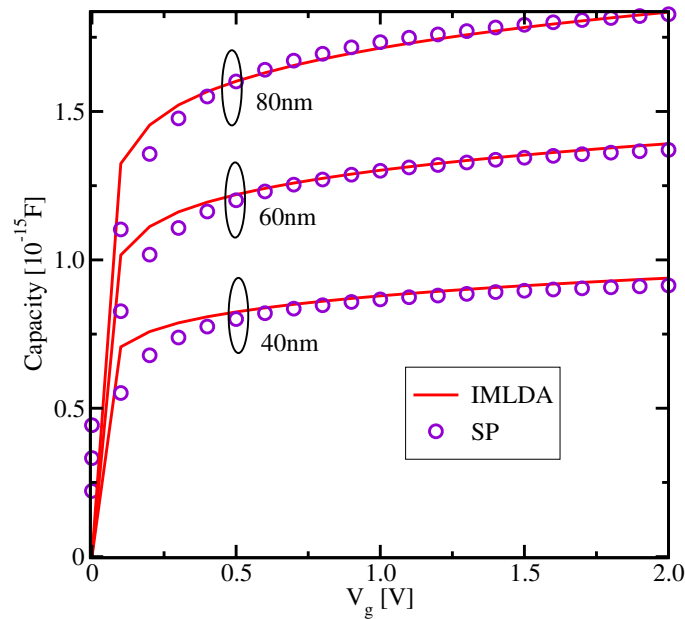


**Figure 5.7:** Capacity versus gate voltages for devices with 40 nm, 60 nm, and 80 nm gate lengths calculated with the *Schrödinger-Poisson* solver and with the calibrated quantum correction model. For a gate voltage used in most simulations of 1.3 V both simulators yield the same result.

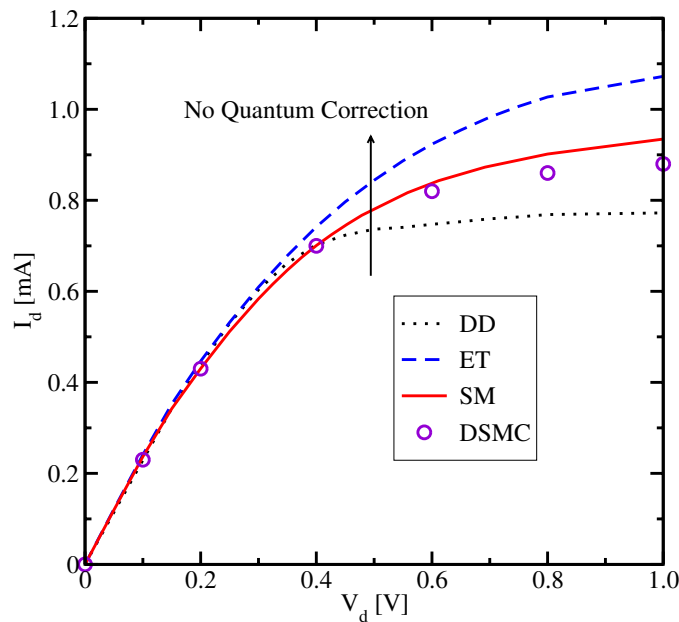


**Figure 5.8:** Output characteristics of a 40 nm channel length UTB SOI MOSFET calculated with the DD, ET, SM models and, as a reference, with DSMC data. As can be observed, the SM model delivers a current very close to the SMC current. Neglecting the quantum correction model increases the output current of the macroscopic models.

### 5.3 Comparison with Device-SMC

To investigate the validity of the developed subband macroscopic models a comparison with the device-SMC simulator will be carried out. Starting with the long channel device, the further focus is put on short channel devices.

#### 5.3.1 Long Channel Device

As a consistency check for long channel devices, all macroscopic transport models together with the DSMC method must yield the same results. In Fig. 5.9 output characteristics of a 1000 nm and a 100 nm channel length SOI MOSFETs are presented.

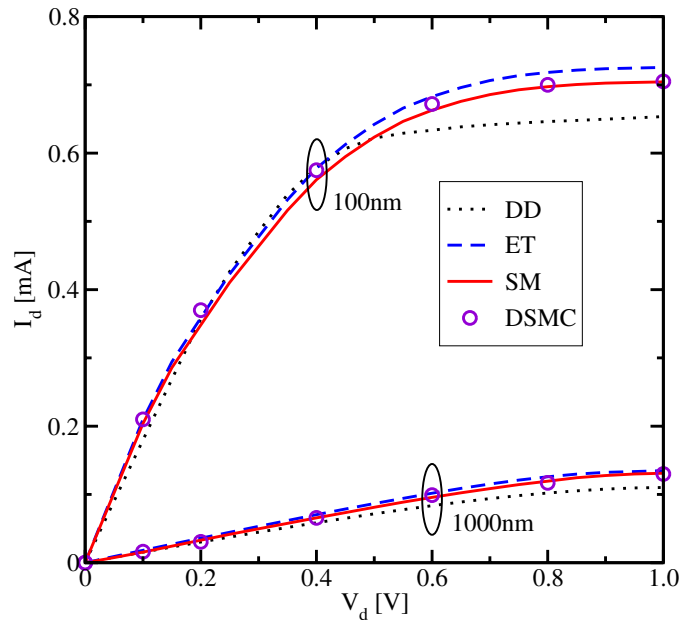


**Figure 5.9:** Output current of 1000 nm and 100 nm channel devices calculated with the DD, ET, and SM model are compared to the output current obtained by DSMC simulations. For the 1000 nm device, the results of all models converge.

As demonstrated for a channel length of 1000 nm, all models predict approximately the same results. Hence, the DD model is a suitable model for long channel devices. However, for a channel length of 100 nm, the SM model and the DSMC method predict comparable output currents, while a significant deviation of the current to lower values can be observed in the DD model for high drain voltages. While the DD model yields lower values, the ET model slightly overestimates the results from DSMC simulations. This current overestimation of the ET model increases for decreasing channel lengths as can be seen in short channel devices (see Fig. 5.8).

### 5.3.2 Short Channel Devices

Output currents of a 40 nm channel SOI MOSFET device have been already demonstrated in Fig. 5.8. The current of a critical channel length device of 30 nm is pointed out in Fig. 5.10. As can be observed already at  $V_d = 0.2$  V, the DD model underestimates the current of the SMC simulation, while the ET overestimates the current. The marks at drain voltages of  $V_d = 0.2$  V,  $V_d = 0.4$  V,  $V_d = 0.6$  V, and  $V_d = 0.8$  V are linked to the velocity profiles presented in Fig. 5.11. However, at high drain voltages, even the DD model is closer to the DSMC results than the ET model. The most accurate model is the SM model, which is also visible in the velocity profiles shown in Fig. 5.11.

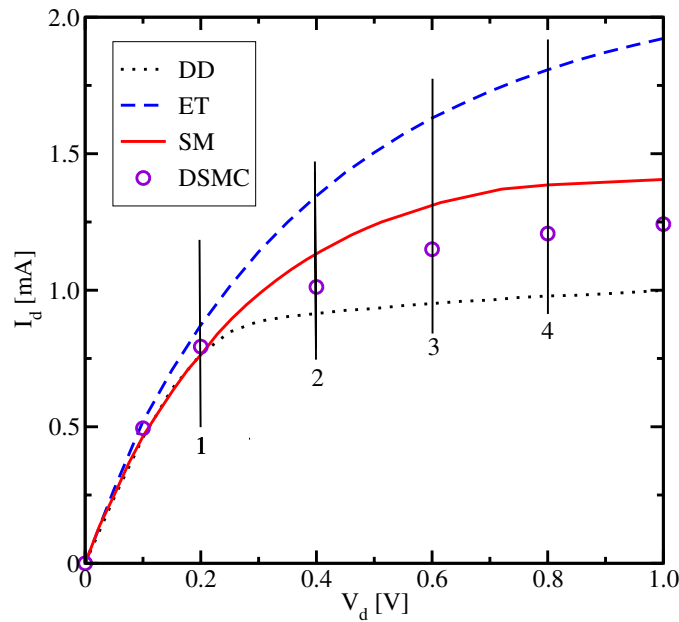


**Figure 5.10:** Output current of a 30 nm channel length device calculated with the DD, ET, SM models, and with the SMC method. The SM model predicts the most accurate result, while ET overestimates and DD underestimates the current, respectively.

Here the velocity profile for several drain voltages of  $V_d = 0.2$  V,  $V_d = 0.4$  V,  $V_d = 0.6$  V, and  $V_d = 0.8$  V of the 30 nm channel device is presented. At low drain voltage of  $V_d = 0.2$  V, the velocity of all macroscopic transport models are equal to the velocity profile obtained by MC simulations, which corresponds to the same output current of Fig. 5.10. However, with increasing drain voltages the velocity profile obtained by the ET model increases rapidly, which has a strong impact on the current of the ET model. The DD model delivers the lowest velocity of all three models due to the inferior closure relation. The velocity obtained from the SM model is between ET and DD model and is very close to the SMC simulation. The spurious velocity overshoot at the end of the channel in the higher-order transport models is also clearly visible for high drain voltages. For low drain voltages, the peak in the velocity profile at the end of the channel disappears. Due to surface roughness scattering and quantum correction, the velocity profile of the 30 nm device is only half as high as in the 3D case (see Fig. 3.14).

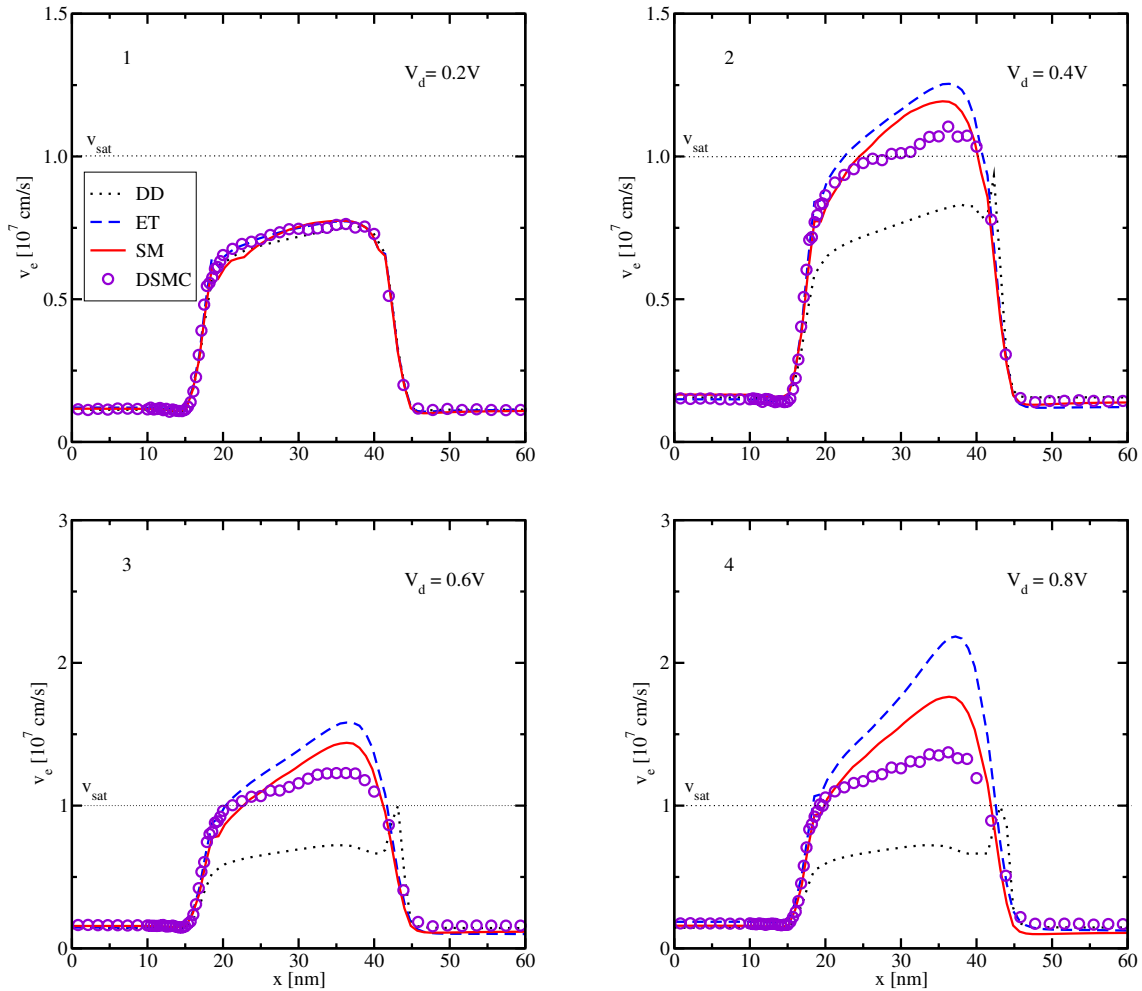


**Figure 5.11:** Evolution of the velocity profiles of a UTB SOI MOSFET with a channel length of 30 nm for drain voltages of  $V_d = 0.2\text{ V}$ ,  $V_d = 0.4\text{ V}$ ,  $V_d = 0.6\text{ V}$ , and  $V_d = 0.8\text{ V}$ . The spurious velocity overshoot, especially in the ET model is clearly visible for drain voltages of 0.8 V. The SM model predicts most accurate results.

In Fig. 5.12, the current at  $V_d = 1\text{ V}$  as a function of the channel length is shown. For 100 nm, the ET and the SM model yield an output current with an error below 5% (see Fig. 5.13), while the error of the current of the DD model is about  $-8\%$ . With a further decrease of the channel length down to 70 nm, the error of the ET model increases rapidly, while the SM model stays below 5%. At about 60 nm, even the magnitude of the error of the DD is smaller than the ET model. For a critical channel length of 30 nm, the error of the DD, ET, and SM model is  $-20\%$ ,  $55\%$ , and  $14\%$ , respectively. Fig. 5.14 shows the transit frequencies of devices with different channel lengths. As can be observed, the SM model is as well the most accurate model compared to the DD and the ET model. The error of the DD model (see Fig. 5.15) of the transit frequencies is higher than the error of the current at very short channel lengths. Therefore, comparing all three macroscopic transport models, the SM approach predicts the most accurate results, while the error of the DD and especially of the ET model increase rapidly below a channel length of 80 nm.

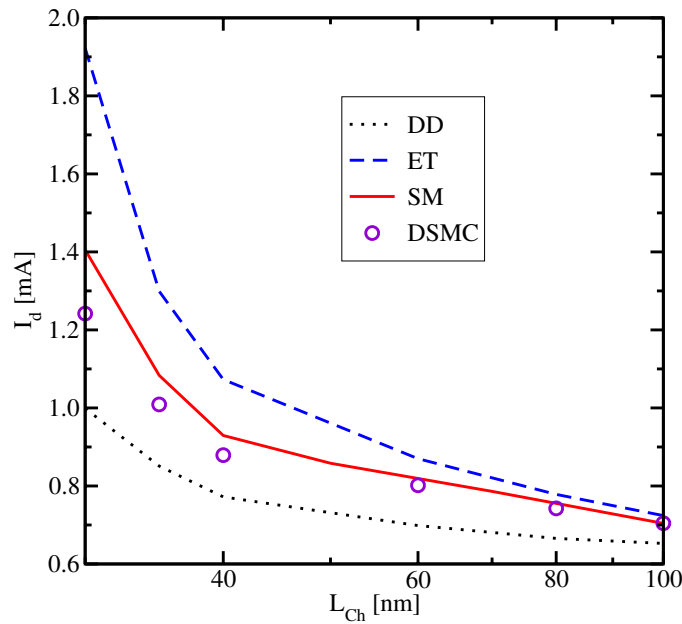


**Figure 5.12:** Output current at  $V_d = 1$  V as a function of the channel length. A significant increase in the current of the ET model at channel lengths below 80 nm can be observed, while the current from the DD model is below the current of the DSMC. The SM model yields the most accurate current.

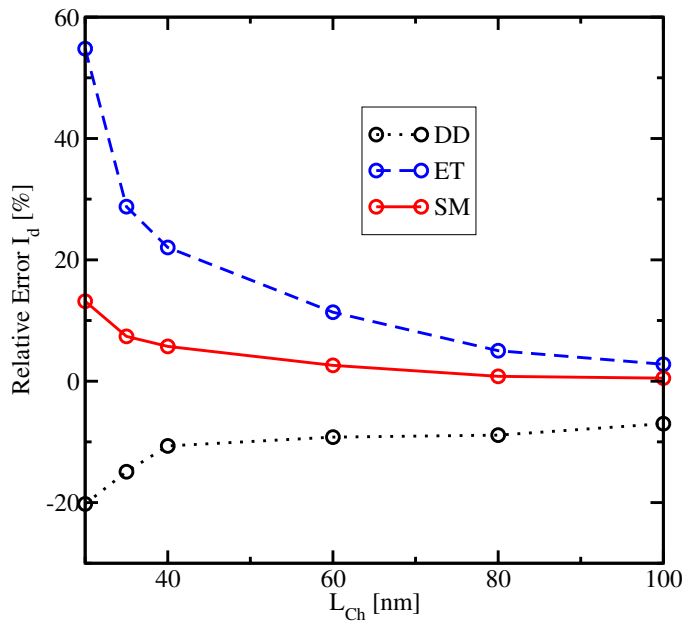


**Figure 5.13:** Relative error as a function of the channel length of the DD, ET, and the SM models. The error of the ET model increases rapidly for devices with a channel length below 80 nm where even the DD model becomes better. The SM model is the most accurate model for short channel devices.

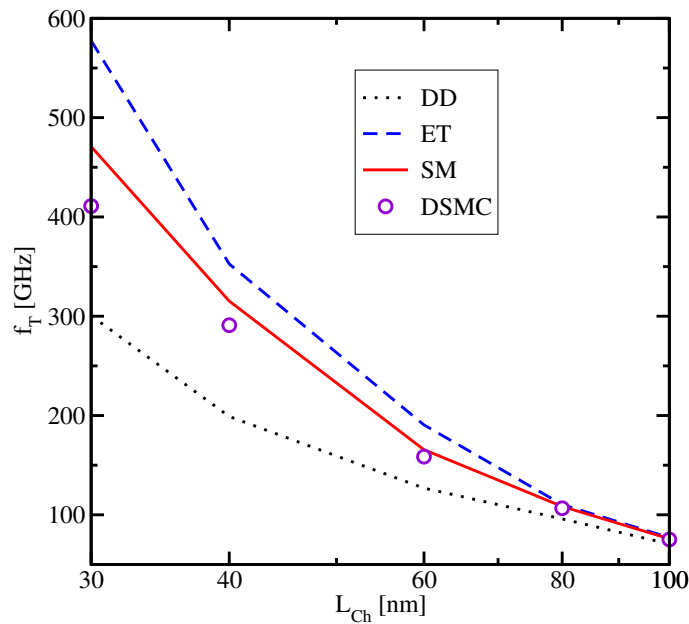


**Figure 5.14:** Transit frequencies as a function of the channel length. A significant increase of the frequency in the ET model at channel lengths below 80 nm can be observed, while the frequency from the DD model is below the frequency of the DSMC. The SM model yields the most accurate result.

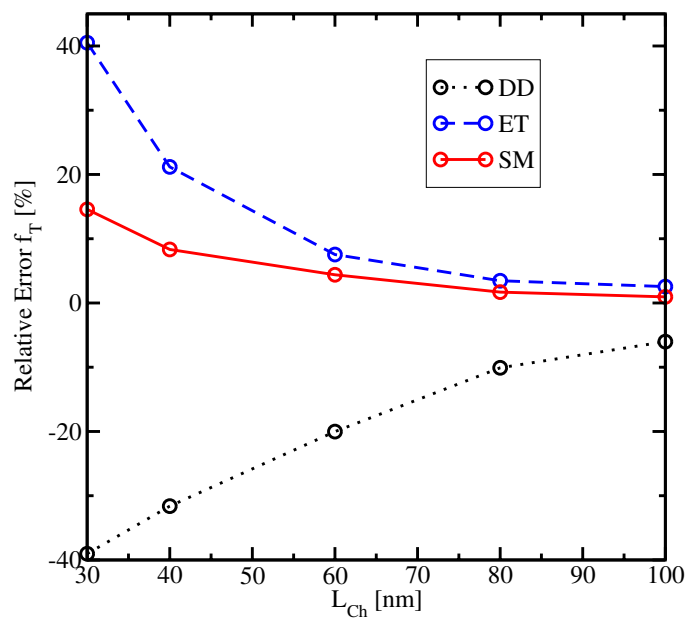


**Figure 5.15:** Relative error of the transit frequencies as a function of the channel length of the DD, ET, and the SM models. The error of the DD model is higher than the error of the current (see Fig. 5.13), while the SM model is here as well the most accurate model.



## 5.4 Influence of SRS on Device Simulations

In order to show the influence of surface roughness scattering within higher-order macroscopic transport models of a whole device, macroscopic transport model simulations have been performed once with MC tables, where SRS is neglected and than with MC tables, where SRS is considered. To show just the impact of SRS, the quantum correction model has been turned off. A 40 nm channel length UTB SOI MOSFET is here the object of investigations.

Fig. 5.16 shows the carrier mobility and higher-order mobility cut of the 40 nm device. As can be observed the influence of SRS at the beginning of the channel is stronger than at the end. This can be explained as follows: As shown in Chapter 4, for low energies the carrier wavefunctions

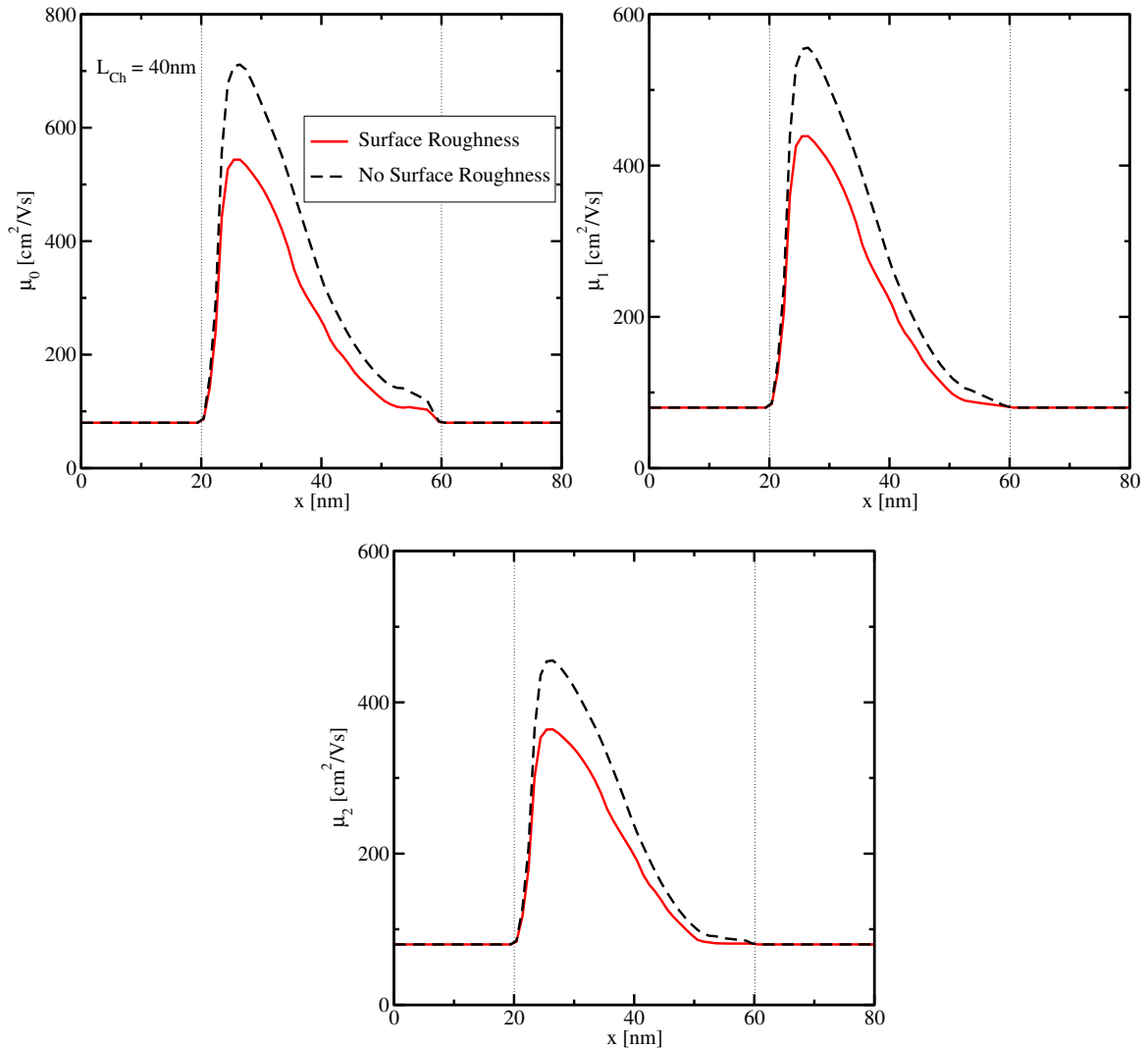


**Figure 5.16:** Carrier and higher-order mobilities for a 40 nm channel length device. The influence of SRS at the beginning of the channel is stronger than at the end.

are closer to the interface than for high energies. The carriers are shifted away from the interface and therefore the impact of surface roughness scattering decrease for high energies. Since the carriers have got low energies at the beginning of the channel the impact of SRS is high. With increasing energies SRS decreases. This is visible in Fig. 5.16. Due to the elastic nature of SRS the relaxation times are unaffected by SRS as already demonstrated in Chapter 4.

Due to the elastic nature of the scattering process, SRS has got only a minor influence on the carrier temperature  $T_n$  and the second-order temperature  $\Theta$  as presented in Fig. 5.17. Fig. 5.18

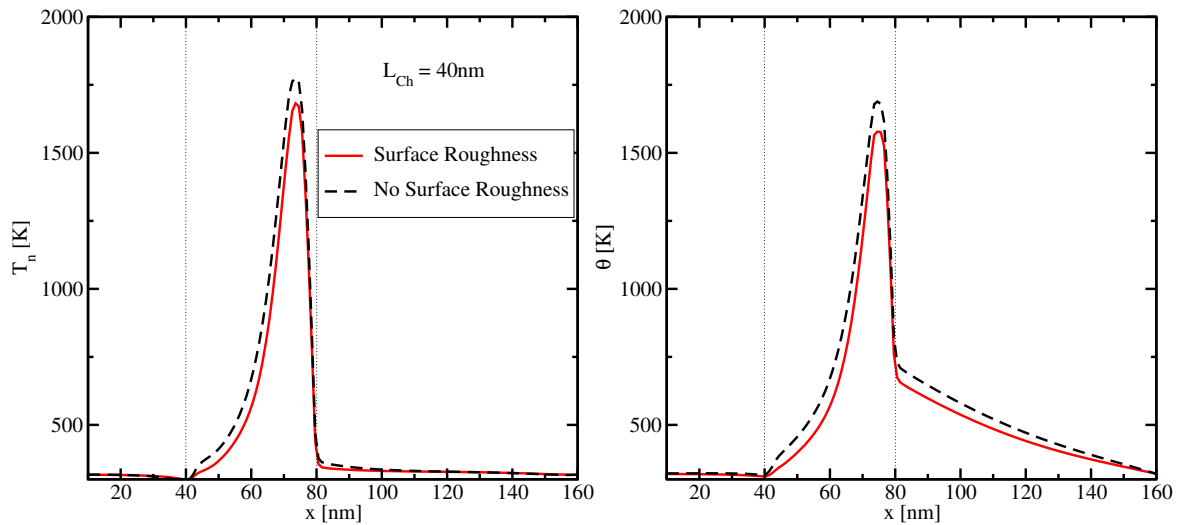


**Figure 5.17:** Carrier temperature  $T_n$  and second-order temperature  $\Theta$  calculated once with MC tables considering SRS and neglecting SRS, respectively. As can be seen  $T_n$  and  $\Theta$  are unaffected by SRS.

shows output characteristics calculated with the DD, ET, and the SM model considering and neglecting SRS. As pointed out, the current, where surface roughness scattering has been neglected is significantly higher, than the current with surface roughness scattering.

## 5.5 2D Subband Simulations versus 3D Bulk Simulations

In this section, a comparison between the 2D higher-order macroscopic models and the 3D higher-order models based on bulk MC tables is carried out. The quantum correction model has been turned off in the device simulator for the 2D and in the 3D case, in order to depict the influence of the 2D discretization and the 2D subband MC tables. In order to have an adequate comparison between 3D bulk simulations, where by definition no surface roughness scattering is considered, SRS has been also neglected in the 2D subband models.

Fig. 5.19 presents velocity profiles of the UTB SOI MOSFET with a channel length of 40 nm calculated with the DD, ET, and the SM model. As can be observed 3D bulk macroscopic models with fullband MC data yield higher velocities than the 2D macroscopic models with subband MC data, where surface roughness scattering is neglected.

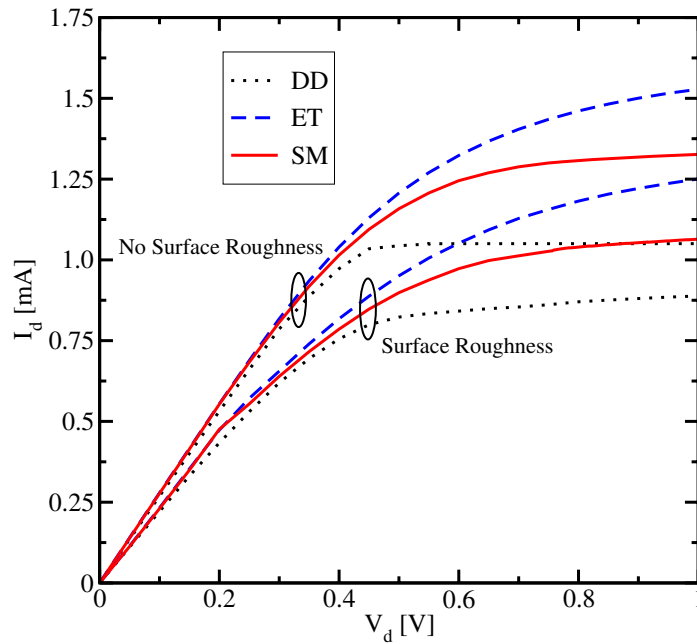


**Figure 5.18:** Output characteristics of a 40 nm channel length SOI MOSFET calculated with the DD, ET, and the SM model using SMC data with SRS and SMC data without SRS.

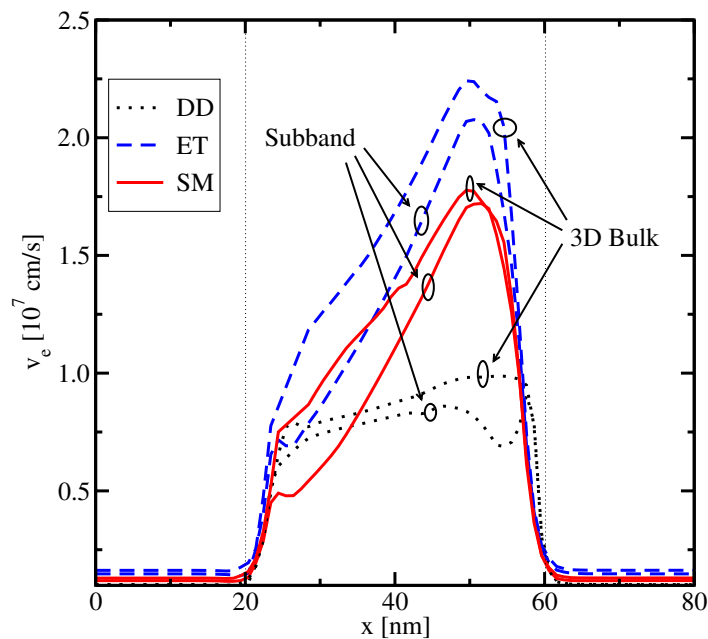


**Figure 5.19:** Velocity profile of a 40 nm channel length SOI MOSFET computed with the two-dimensional DD, ET, and SM model neglecting SRS in the subband MC tables and with the 3D macroscopic models using fullband MC tables.

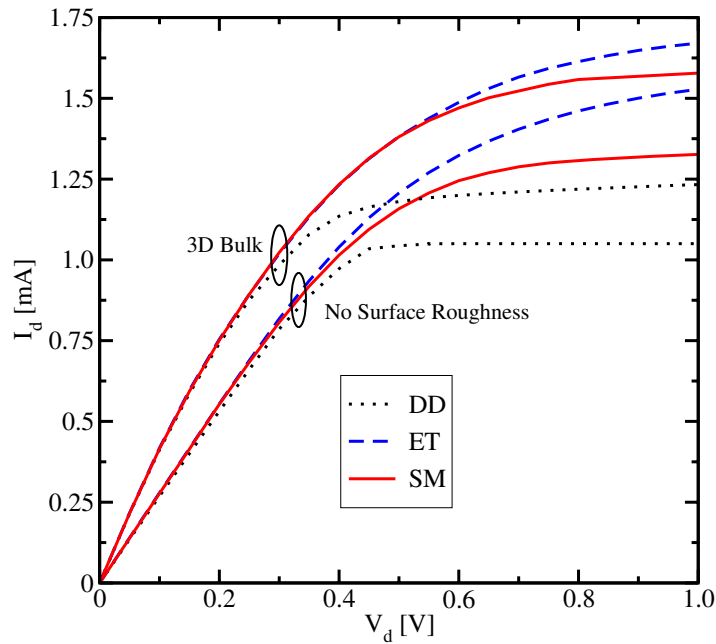


**Figure 5.20:** Output characteristics of a 40 nm channel length SOI MOSFET calculated once with the 2D macroscopic models using SMC data without SRS and with their 3D counterpart using fullband MC data.

Due to the higher velocities in the bulk regime, the output currents of the DD, ET, and the SM model are also higher than in the subband system as shown in Fig. 5.20.

A higher-order macroscopic approach to describe carrier transport in the inversion channel of advanced devices such as UTB SOI MOSFETs has been demonstrated and successfully compared to device-SMC data. A very good agreement of the output current down to channel length of 40 nm between the SMC simulations and the 2D six moments model based on SMC data is observed. The great advantage of macroscopic models compared to Monte Carlo simulations is the time factor, which makes it suitable for engineering applications.

*'There are two possible outcomes: if the result confirms the hypothesis, then you have made a measurement. If the result is contrary to the hypothesis, then you have made a discovery.'*

Enrico Fermi

## Chapter 6

---

# Material Investigations

---

**A**N OUTLOOK of the behavior of higher-order macroscopic transport parameters in the bulk regime of semiconductor alloys such as Silicon-Germanium (SiGe) and Gallium Arsenide (GaAs) is given. Investigations concerning the closure relation of the six moments model using the MC method are carried out.

### 6.1 Higher-Order Parameter Extraction

So far in this work, all transport investigations have been performed for Si. However, for instance in high-frequency devices such as high electron mobility transistors (HEMTs) the basic semiconductor material is GaAs. Therefore, for engineering applications, an accurate macroscopic description of carrier transport in other materials is of substantial importance. With the developed MC based transport parameter model it is possible to characterize higher-order transport models in these materials with as few approximations as possible. Hence, a study of higher-order parameters in these material systems is very crucial. In order to describe 3D bulk higher-order macroscopic transport models in materials as SiGe [164–166] and GaAs [167], the relaxation times as well as the higher-order mobilities are extracted as a function of the kinetic energy of the carriers and as functions of the lateral electric field, respectively.

#### 6.1.1 Silicon-Germanium

With increasing Ge fraction up to 40% in Si, the values of higher-order mobilities decrease, due to the increase of alloy scattering as visualized in Fig. 6.1. Here, the mobilities  $\mu_0$ ,  $\mu_1$ , and  $\mu_2$  are presented as a function of the electric field for a doping concentration of  $10^{15} \text{ cm}^{-3}$ ,  $10^{17} \text{ cm}^{-3}$ , and  $10^{19} \text{ cm}^{-3}$ , respectively and for a Ge composition in Si of 10% and 40%. A non-parabolic band structure has been assumed. As pointed out the mobilities of 10% Ge fraction are higher than the mobilities of 40%. For high-fields the values of the mobilities yield more or less the same results, while for low fields a significant splitting especially in the 10% Ge fraction case between the highly doped and the lowly doped concentration is visible. The energy flux and the second-order energy flux mobilities are for low doping concentrations lower

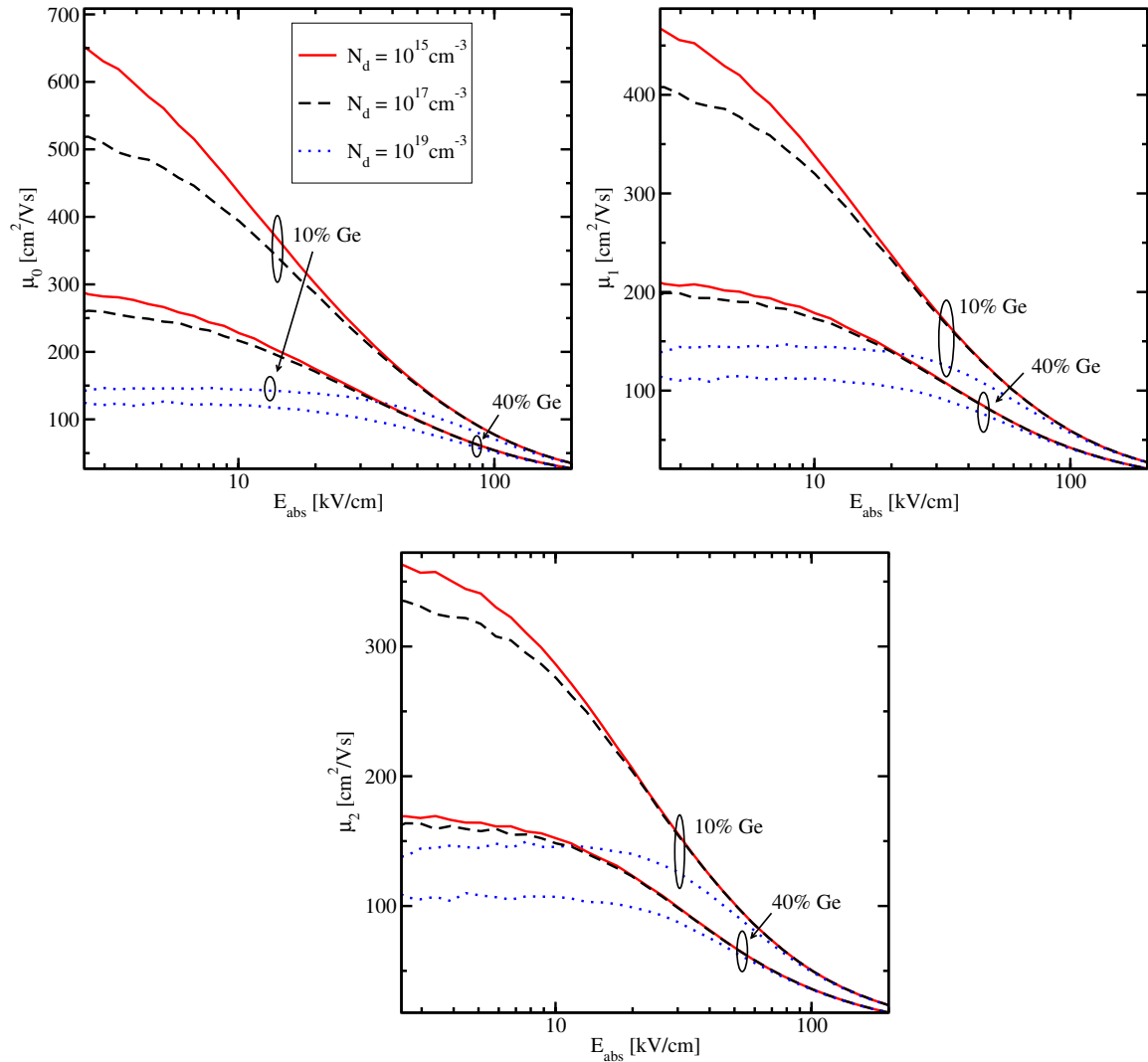


**Figure 6.1:** Carrier mobility and higher-order mobilities for a 10 % and 40 % Ge composition, respectively as a function of the lateral electric field. Ge has got a deep influence on the mobilities for low fields, while for high-fields the influence of Ge on the mobilities decreases.

than the carrier mobility. However, as can be seen, for increasing doping concentrations the higher-order mobilities together with  $\mu_0$  are practically equal. Such a behavior is also typical for Si (see Fig. 3.1). The carrier mobility together with the higher-order mobilities for low fields as a function of the Ge composition are given in Fig. 6.2. The carrier mobility shows a very good agreement with the mobility data from [8]. All mobilities have a minimum at 40 % Ge, while a high increase of the mobility values at a Ge composition greater than 80 % can be observed. For pure Ge the mobilities are very high. In Fig. 6.3, the energy relaxation time and the second-order relaxation time are given for different Ge fractions as a function of the carrier kinetic energy. As can be observed, the energy relaxation time for the 10 % Ge case is lower than for the 40 % Ge case, which is an indication of the higher optical phonon scattering rate in the 10 % Ge case compared to the 40 % Ge.

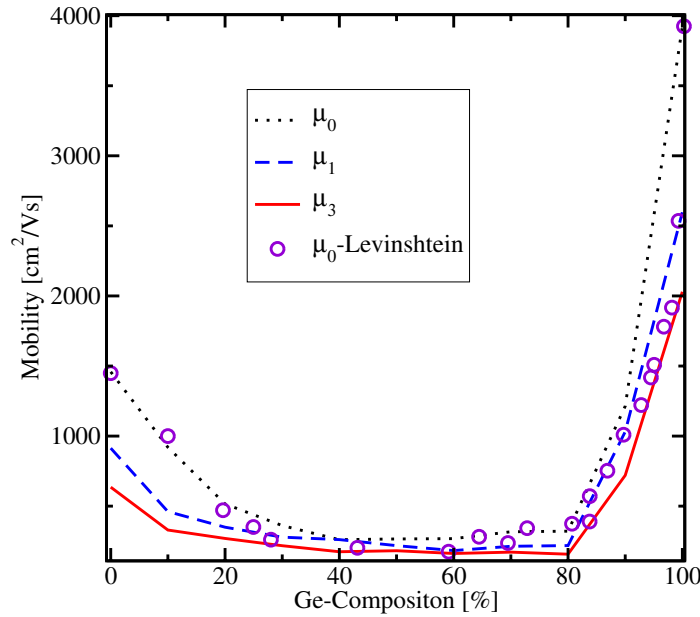


**Figure 6.2:** Low field carrier mobility together with higher-order mobilities as a function of the Ge composition. The carrier mobility fits the data from [8] quite well. The minimum of the mobilities is at 40 %, while a high increase of the mobility values can be observed for Ge composition greater than 80 %.

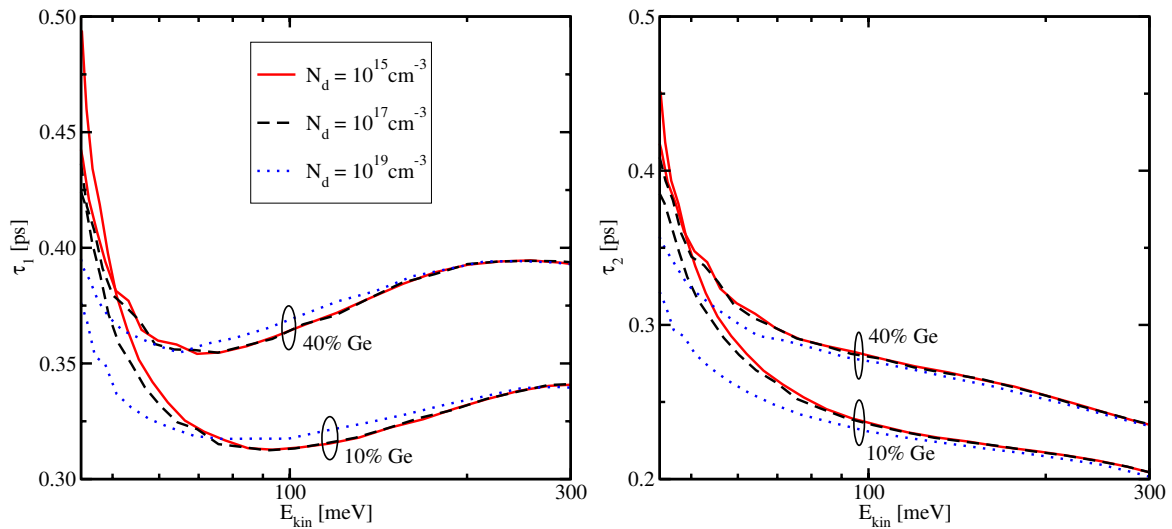


**Figure 6.3:** The energy relaxation time (left) and the second-order relaxation time (right) for a Ge mole fraction of 10 % and 40 % as a function of the carrier energy. For the 10 % Ge case the relaxation times are lower than for the 40 % Ge case.

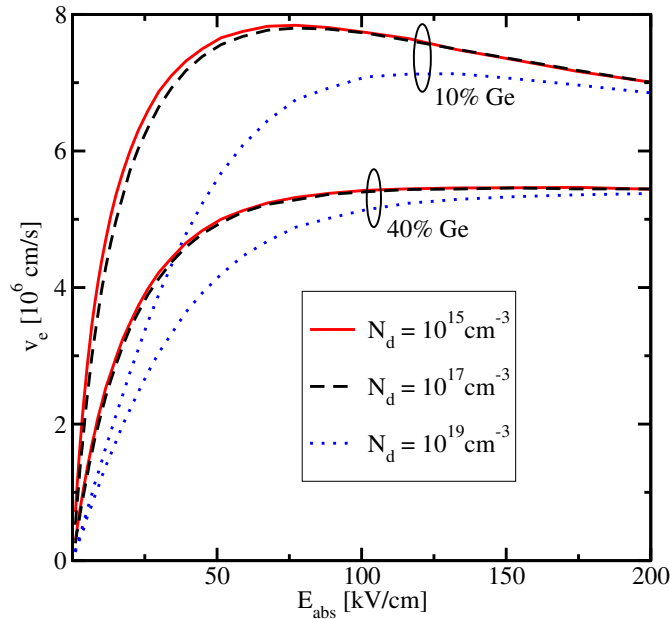


**Figure 6.4:** Carrier velocities for different doping concentrations as a function of the electric field and for different Ge compositions. For high fields the velocities are independent of the doping concentrations, while the velocities for low Ge compositions are higher than for the 40 % case.

The velocities for the same doping concentrations as for the higher-order transport parameters are shown in Fig. 6.4. For high electric fields the values of the velocities are independent of the doping concentrations, while their maximum values are reduced in the 40 % Ge case. For Ge composition higher than 40 % the velocity would increase, due to the rise of the carrier mobility for Ge composition greater than 40 % as can be seen in Fig. 6.2.

The kurtosis of a 100 nm channel length  $n^+nn^+$  structure is presented in Fig. 6.5 for pure Si and for SiGe with a Ge composition of 40 %. An electric field of 50 kV/cm in the middle of the channel has been applied. As can be observed in the channel, the kurtosis of the 40 % Ge case is approximately 0.85, while the kurtosis in the Si case is 0.8. The maximum values at the beginning of the drain region is 1.4 in Si and 1.3 in SiGe, respectively. The kurtosis in 40 % Ge is closer to unity than for the Si case, which is an indication that the carrier distribution function of 40 % Ge is closer to a heated *Maxwellian* than in pure silicon. This is also visible in Fig. 6.6.

Next, investigations concerning the empirical factor  $c$  of the closure relation of the six moments model in SiGe are carried out. The sixth moment from MC simulations divided by the analytical expressions (2.124) is shown in Fig. 6.6. The lower order moments from equation (2.124) has been used from MC. It has been demonstrated that the value 2.7 is as well the best choice in SiGe and is even improved compared to the Si case, which is also pointed out in Fig. 6.6.



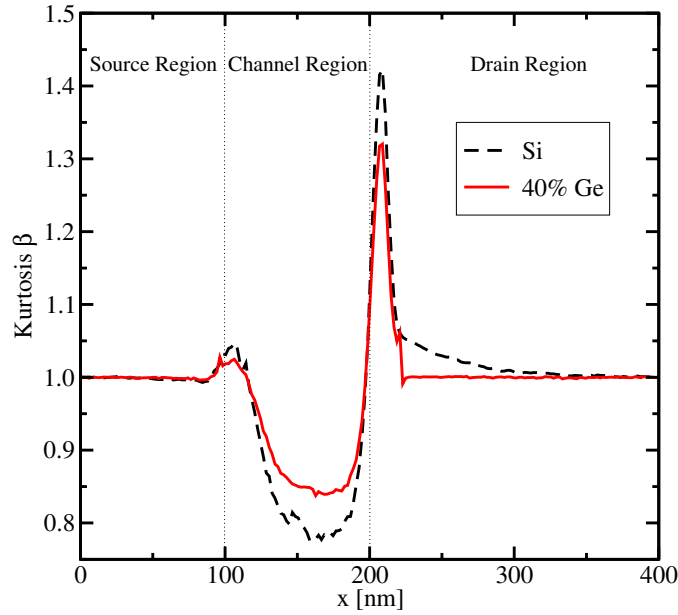


**Figure 6.5:** Kurtosis for a 100 nm  $n^+nn^+$  structure for Si and SiGe. In the channel region the kurtosis of SiGe is higher than in Si, while the kurtosis of Si exceeds the one of SiGe at the beginning of the drain region.

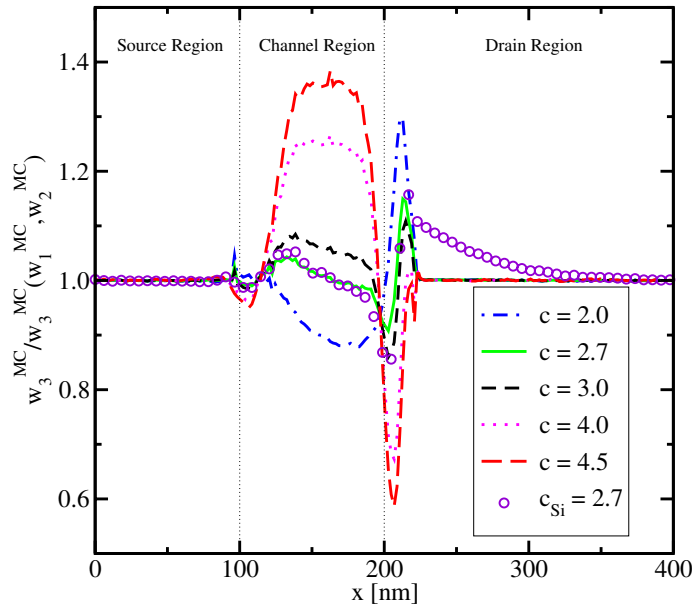


**Figure 6.6:** Sixth moment obtained by MC simulations divided by the expression from equation (2.124) for different values of  $c$ . The value 2.7 is also a very good choice in SiGe and is even improved compared to Si.

### 6.1.2 Gallium Arsenide

The carrier mobility together with the higher-order mobilities are presented in Fig. 6.7. As demonstrated,  $\mu_0$  is very high for a doping concentration of  $10^{15} \text{ cm}^{-3}$  compared to Si, which makes GaAs very attractive for high electron mobility transistors (HEMT) [167–171]. Lower values of  $\mu_1$  and  $\mu_2$  can be observed for doping concentrations of  $10^{15} \text{ cm}^{-3}$  and  $10^{17} \text{ cm}^{-3}$ , while for high doping concentrations, the values of all three mobilities are comparable.

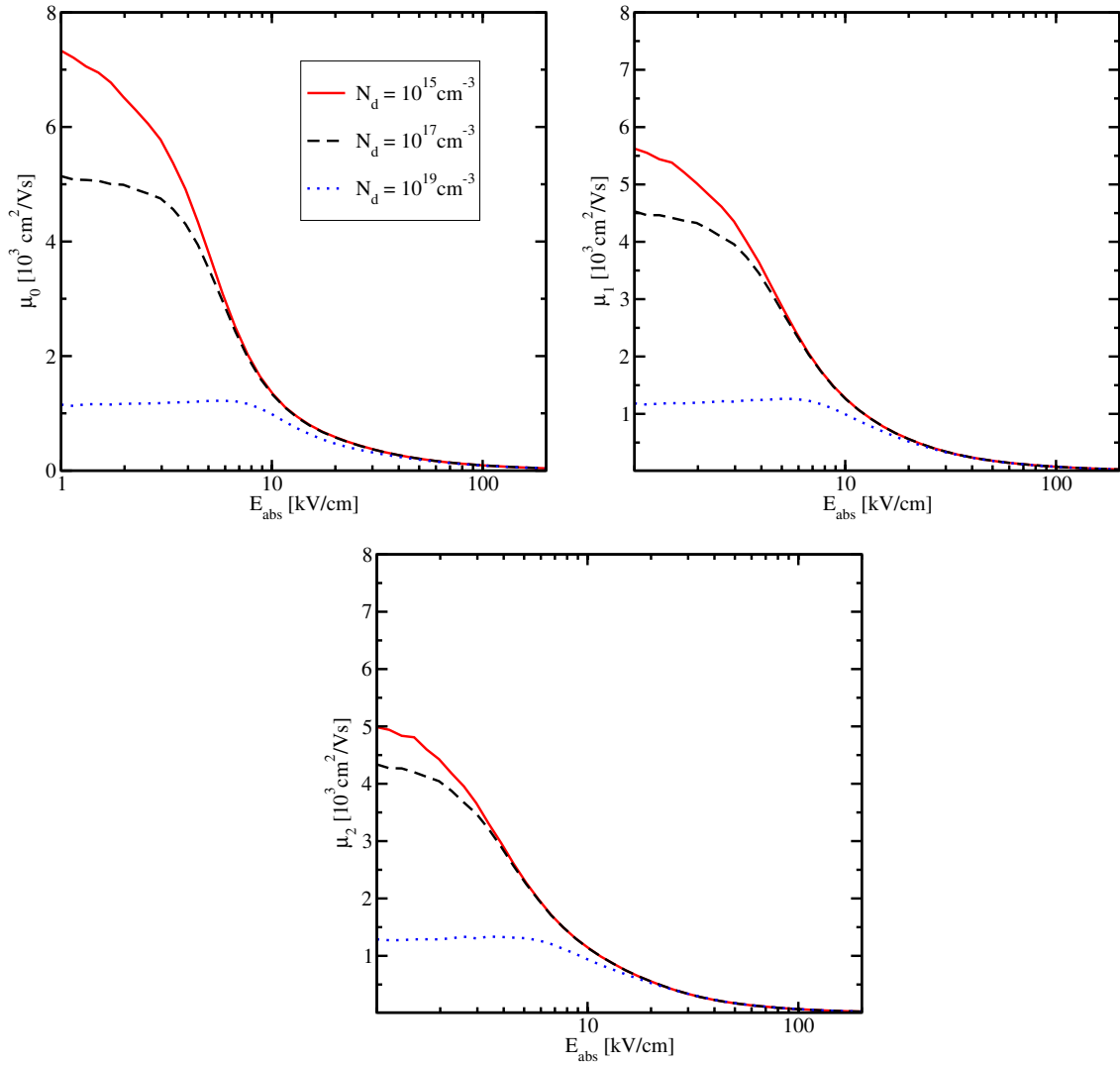


**Figure 6.7:** Carrier mobility and higher-order mobilities for GaAs as a function of the lateral electric field. The values of the mobilities are very high with respect to the ones for Si.

The energy relaxation time and the second-order energy relaxation time for different dopings as a function of the kinetic energy is presented in Fig. 6.8. As depicted, the value of  $\tau_1$  is higher than in Si or SiGe and the peak corresponds to the kinetic energy of 100 meV.

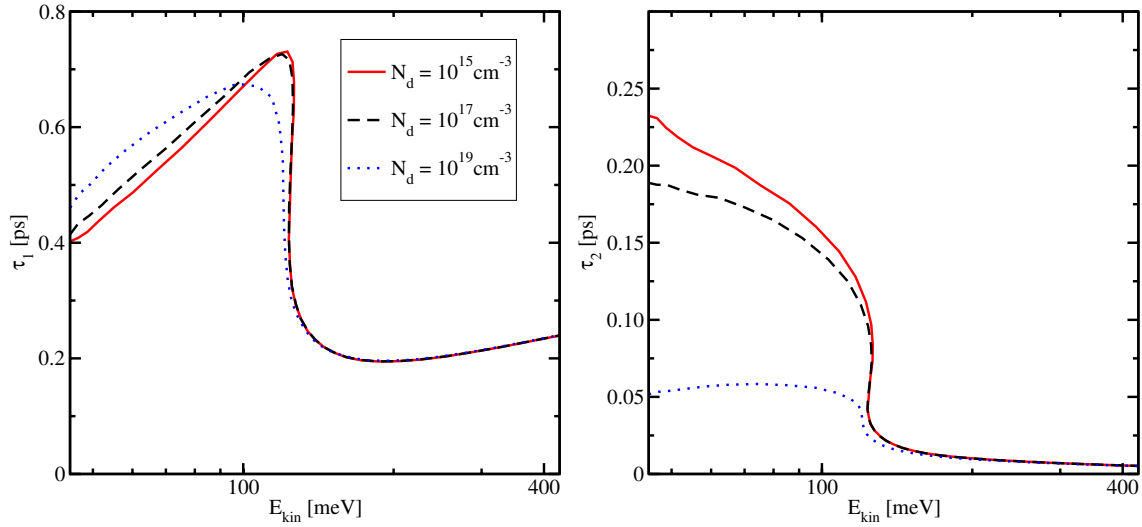


**Figure 6.8:** Energy relaxation time and the second-order relaxation time for GaAs obtained for different doping concentrations as a function of the kinetic energy. The energy relaxation time has its maximum at 100 meV, while the shape of the second-order energy relaxation time is completely different compared to the energy relaxation time.

Different relaxation times can be observed for different doping concentrations for energies below 150 meV, while for high kinetic energies  $\tau_1$  and  $\tau_2$  are doping concentration independent. Note that the shape of  $\tau_1$  and  $\tau_2$  is different compared to Si and SiGe, where these values are more or less equal. The reason of the strong decrease of the relaxation times at 120 meV is the transition of the carriers from the light effective mass valley ( $\Gamma$ -valley) to the heavy effective mass (L-valley). In Fig. 6.9 the velocity for doping concentrations of  $10^{15} \text{ cm}^{-3}$ ,  $10^{17} \text{ cm}^{-3}$ , and  $10^{19} \text{ cm}^{-3}$  are plotted as a function of the driving field. This velocity behavior in GaAs can be explained in a two valley picture [9] similar to the shape of the relaxation times as demonstrated in Fig. 6.10. Here the valleys around the  $\Gamma$  and L points of GaAs are shown. The  $\Gamma$ -valley and the L-valley have effective masses of  $m^* = 0.063m_0$  and  $m^* = 0.55m_0$ , respectively. Due to the light effective mass, the carrier mobility of the  $\Gamma$  valley is high, while the mobility decreases in the L-valley due to the heavy mass. Such a behavior related to different effective masses in each valley of GaAs leads to the decrease of carrier velocity for high fields as demonstrated in Fig. 6.9. However, the maximum carrier velocity in GaAs is more or less twice as high as in Si and therefore the kinetic energy of the carriers is four times larger than in Si. This is also reflected in Fig. 6.11.

Here, the kurtosis of a  $n^+nn^+$  structure with a channel length of 100 nm in GaAs and Si is given. As can be observed, the kurtosis in GaAs is higher in the channel and at the beginning of the drain region than in Si, which is an indication of the higher influence of the energies in GaAs on the distribution function than in Si. This is depicted in Fig. 6.12. Here, the closure relation investigations of the six moments model concerning the empirical factor  $c$  of equation (2.124) is shown and compared to the Si case. As can be observed 2.7 is also a very good choice for  $c$  in GaAs.

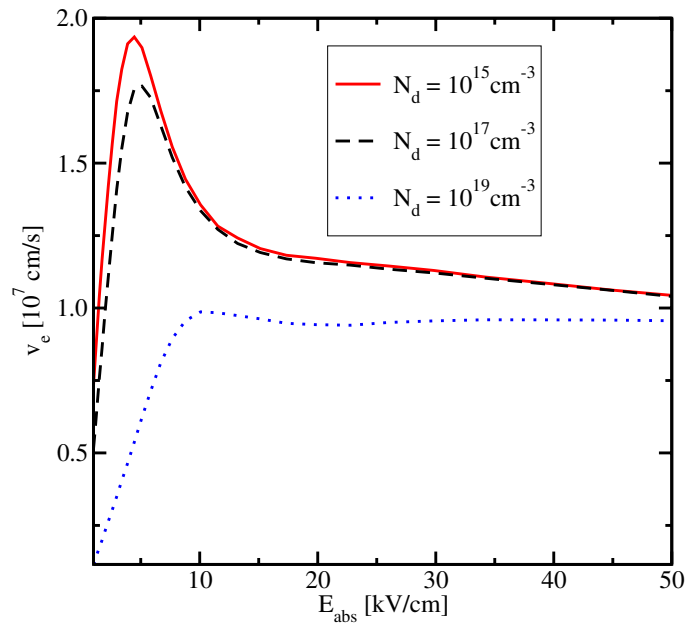


**Figure 6.9:** The carrier velocity for different doping concentrations as a function of the driving field. For a field of 5 kV/cm the carrier velocity has its maximum, while for high fields the velocity decreases.

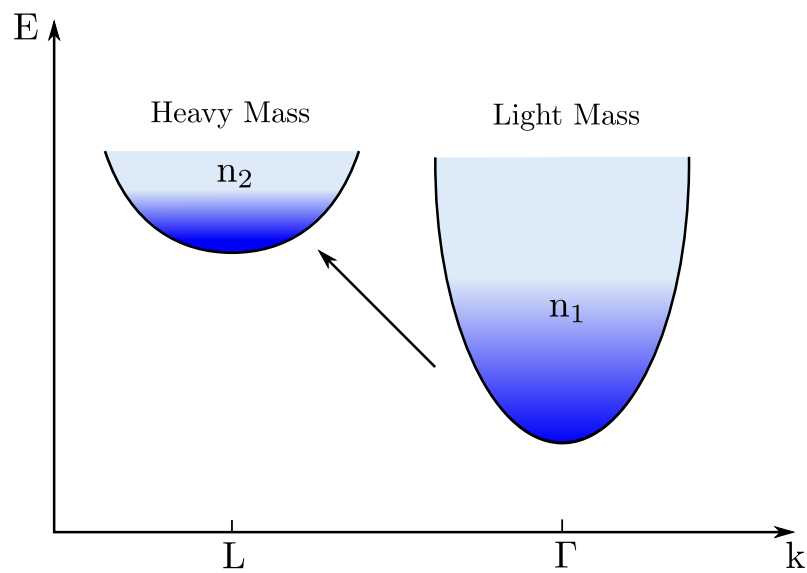


**Figure 6.10:**  $\Gamma$ - and L-valleys of GaAs are shown. For low fields the carriers are in the light hole  $\Gamma$ -valley, while for high-fields the carriers are in the upper heavy hole valleys, decreasing the carrier velocity (after [9]).

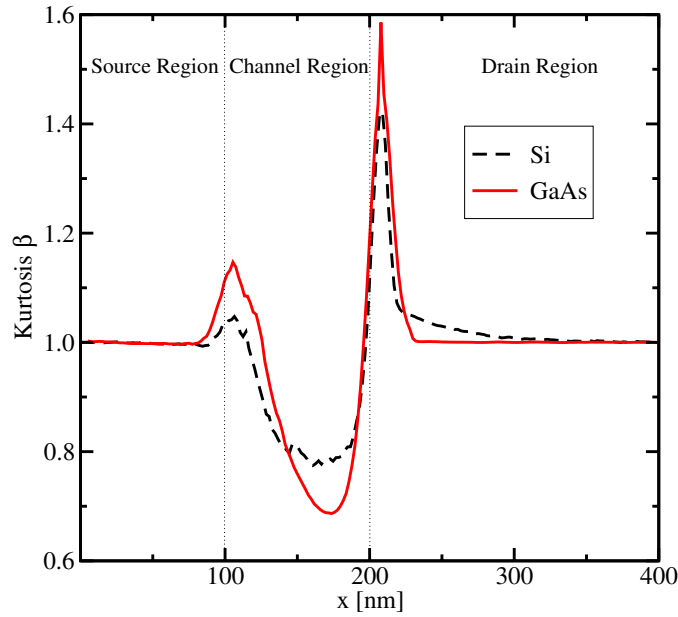


**Figure 6.11:** Kurtosis profile of the  $n^+nn^+$  structure with a channel length of 100 nm of GaAs and Si. The kurtosis at the end of the channel is lower in GaAs than in Si, while the kurtosis of GaAs is beyond Si at the beginning of the drain region.

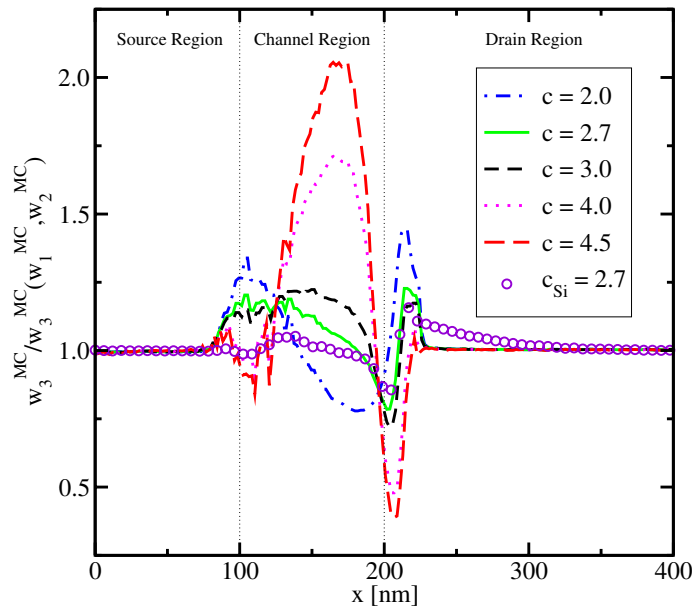


**Figure 6.12:** Sixth moment obtained by MC simulations divided by the analytical expression from equation (2.124) for different values of  $c$ . The lower-order moments for equation (2.124) have been taken from MC simulations. Note that  $c = 2.7$  is also a good choice in GaAs.

'A man may die, nations may rise and fall, but an idea lives on.'

Albert Einstein

## Chapter 7

---

# Summary and Conclusion

---

TO EFFICIENTLY characterize carrier transport in the inversion layer of deca-nanometer devices, a higher-order transport model for a two-dimensional electron gas based on *Subband Monte Carlo* tables has been developed. The first six moments of *Boltzmann's* transport equation are considered and compared to device-*Subband Monte Carlo* simulations. Fully depleted ultra thin body SOI MOSFETs with several channel lengths are the objects of investigations. As a consistency check, for long channel devices ( $\approx 1000$  nm) all models converge to the same results. With decreasing channel lengths down to 100 nm, the drift-diffusion model underestimates the current compared to the reference *Subband Monte Carlo* device simulator, while the energy transport and the six moments model can accurately reproduce the reference results. The error of the current of the energy transport model increases rapidly below a channel length of 80 nm and becomes even larger than the error of the drift-diffusion model at 40 nm. The error of the six moments model is about 17% for a critical channel length of 30 nm, while the errors of the drift-diffusion and the energy transport model are at -20% and 55%, respectively. A comparison of a very sensitive quantity, the transit frequencies of the drift-diffusion, energy transport, and the six moments model has been carried out. The error of the drift-diffusion, energy transport, and the six moments model is at -40%, 40%, and 18% for a channel length of 30 nm, respectively. The inaccuracy of the drift-diffusion model in the transit frequency is twice as large as in the current. The developed six moments model for carrier transport in inversion layers yields very accurate results through the whole scattering dominated regime and outperforms the energy transport and the drift-diffusion model in deca-nanometer channel length devices.

Furthermore, a detailed study concerning the impact of surface roughness scattering and quantization on higher-order transport parameters is given for the homogeneous inversion layer and in a whole device. It has been demonstrated that the influence of surface roughness scattering on the carrier mobility within low fields is higher than for the higher-order mobilities, while the relaxation times are unaffected by surface roughness scattering, due to the elastic nature of the process. The influence of quantization on transport parameters is presented by a comparison between *Subband Monte Carlo* simulations and three-dimensional bulk Monte Carlo data. Additionally, the behavior of higher-order macroscopic models for a three-dimensional electron gas has been investigated using  $n^+nn^+$  test-structures. Here, short channel effects as well as the validity of macroscopic models are studied and benchmarked against the *Spherical Harmonics Expansion* approach. The increasing error of the models for decreasing channel lengths

is demonstrated. Investigations concerning the closure relation of the six moments model are given. It shows that the empirical factor of the closure relation of the three-dimensional electron gas can be used also in a quantized system of a two-dimensional electron gas and in material alloys such as SiGe and GaAs. In order to use higher-order macroscopic transport models in material alloys, higher-order transport parameters are extracted and discussed.

---

# Bibliography

---

- [1] M. Lundstrom, *Fundamentals of Carrier Transport*. Cambridge University Press, 2000.
- [2] M. Karner, A. Gehring, S. Holzer, M. Pourfath, M. Wagner, W. Gös, M. Vasicek, O. Baumgartner, C. Kernstock, K. Schnass, G. Zeiler, T. Grasser, H. Kosina, and S. Selberherr, “A Multi-Purpose Schrödinger–Poisson Solver for TCAD applications,” *J. Comput. Electronics*, vol. 6, pp. 179–182, 2007.
- [3] M. Wagner, M. Karner, and T. Grasser, “Quantum Correction Models for Modern Semiconductor Devices,” in *Proceedings of the XIII International Workshop on Semiconductor Devices*, 2005.
- [4] T. Grasser, T. Tang, H. Kosina, and S. Selberherr, “A Review of Hydrodynamic and Energy–Transport Models for Semiconductor Device Simulation,” *Proceedings of the IEEE*, vol. 91, pp. 251–274, 2003.
- [5] T. Grasser, H. Kosina, and S. Selberherr, “Hot Carrier Effects within Macroscopic Transport Models,” *Int. J. of High Speed Electronics and Systems*, vol. 13, pp. 973–901, 2003.
- [6] T. Grasser, H. Kosina, and S. Selberherr, “Investigation of Spurious Velocity Overshoot using Monte Carlo Data,” *Appl. Phys. Lett.*, vol. 79, pp. 1900–1902, 2001.
- [7] S. Takagi, A. Toriumi, M. Iwase, and H. Tango, “On the Universality of Inversion Layer Mobility in Si MOSFET’s: Part I - Effects of Substrate Impurity Concentration,” *IEEE Trans. Electron Devices*, vol. 41, pp. 2357–2362, 1994.
- [8] M. Levinshstein, S. Rumyantsev, and M. Shur, *Properties of Advanced Semiconductor Materials*. John Wiley & Sons, Inc., 2001.
- [9] S. Sze and K. Ng, *Physics of Semiconductor Devices*. Wiley, 2007.
- [10] G. Moore, “Cramming more Components onto Integrated Circuits,” *Electronics*, vol. 38, 1965.
- [11] G. Moore, “Lithography and the Future of Moore’s Law,” in *Proc. SPIE*, 1995.



- [12] S. I. Association, "International Technology Roadmap for Semiconductors - 2007 Update, 2007," tech. rep., <http://www.itrs.net>, 2007.
- [13] G. Shahidi, "SOI Technology for the GHz Era," *IBM J.Res.Dev.*, vol. 46, pp. 121–131, 2002.
- [14] D. Scharfetter and H. Gummel, "Large-Signal Analysis of a Silicon Read Diode Oscillator," *IEEE Trans.Electron Devices*, vol. 16, pp. 64–77, 1969.
- [15] T. Tang, "Extension of the Scharfetter-Gummel Algorithm to the Energy Balance Equation," *IEEE Trans.Electron Devices*, vol. ED-31, pp. 1912–1914, 1984.
- [16] R. Stratton, "Diffusion of Hot and Cold Electrons in Semiconductor Barriers," *Physical Review*, vol. 126, no. 6, pp. 2002–2014, 1962.
- [17] T. Bordelon, V. Agostinelli, X. Wang, C. Maziar, and A. Tasch, "Relaxation Time Approximation and Mixing of Hot and Cold Electron Populations," *Electronics Letters*, vol. 28, pp. 1173–1175, 4 June 1992.
- [18] B. J. Geurts, M. Nekovee, H. M. J. Boots, and M. F. H. Schuurmans, "Exact and Moment Equation Modeling of Electron Transport in Submicron Structures," *Appl.Phys.Lett.*, vol. 59, pp. 1743–1745, Sep 1991.
- [19] A. Abramo and C. Fiegna, "Electron Energy Distributions in Silicon Structures at low Applied Voltages and High Electric Fields," *J.Appl.Phys.*, vol. 80, pp. 889–893, 1996.
- [20] T. Grasser, H. Kosina, M. Gritsch, and S. Selberherr, "Using Six Moments of Boltzmann's Transport Equation for Device Simulation," *J.Appl.Phys.*, vol. 90, pp. 2389–2396, 2001.
- [21] T. Grasser, R. Kosik, C. Jungemann, H. Kosina, and S. Selberherr, "Nonparabolic Macroscopic Transport Models for Device Simulation based on Bulk Monte Carlo Data," *J.Appl.Phys.*, vol. 97, no. 12, 2005.
- [22] C. Jacoboni and L. Reggiano, "The Monte Carlo Method for the Solution of Charge Transport in Semiconductors with Applications to Covalent Materials," *Review of Modern Physics*, vol. 55, pp. 645–705, 1983.
- [23] E. Ungersböck and H. Kosina, "Monte Carlo Study of Electron Transport in Strained Silicon," *J.Comput.Electronics*, vol. 5, pp. 79–83, 2006.
- [24] M. Nedjalkov, H. Kosina, and S. Selberherr, "Monte Carlo Algorithms for Stationary Device Simulations," *Math. Comp. in Simulation*, vol. 62, pp. 453–461, 2003.
- [25] G. Meller, L. Li, and H. Kosina, "Monte Carlo Simulation of Molecularly Doped Organic Semiconductors," in *3rd European Conference on Organic Electronics and Related Phenomena Book of Abstracts*, 2005.
- [26] D. Venture, A. Gnudi, and G. Baccarani, "Multidimensional Spherical Harmonics Expansion of Boltzmann Equation for Transport in Semiconductors," *Appl.Math.Lett.*, vol. 5, pp. 85–90, 1992.

- [27] V. Sverdlov, A. Gehring, H. Kosina, and S. Selberherr, “Quantum Transport in Ultra-Scaled Double-Gate MOSFETs: A Wigner Function-Based Monte Carlo Approach,” *Solid-State Electron.*, vol. 49, pp. 1510–1515, 2005.
- [28] J. Wang and M. Lundstrom, “Does Source-to-Drain Tunneling Limit the Ultimate Scaling of MOSFETs?,” in *IEDM*, 2002.
- [29] M. Lundstrom and Z. Ren, “Essential Physics of Carrier Transport in Nanoscale MOSFETs,” *IEEE Trans. Electron Devices*, vol. 49, pp. 133–141, Jan. 2002.
- [30] M. Büttiker, Y. Imry, R. Landauer, and S. Pinhas, “Generalized Many-Channel Conductance Formula with Application to Small Rings,” *Physical Review B*, vol. 31, pp. 6207–6215, 1985.
- [31] S. Datta, *Quantum Transport Atom to Transistor*. Cambridge University Press, 2005.
- [32] H. Kosina, V. Sverdlov, and T. Grasser, “Wigner Monte Carlo Simulation: Particle Annihilation and Device Applications,” in *Proc. International Conference on Simulation of Semiconductor Processes and Devices*, pp. 357–360, 6–8 Sept. 2006.
- [33] M. Nedjalkov, H. Kosina, and D. Vasileska, *Wigner Ensemble Monte Carlo: Challenges of 2D Nano-Device Simulation*. Springer-Verlag Berlin Heidelberg, 2008.
- [34] M. Fischetti, “Theory of Electron Transport in Small Semiconductor Devices using the Pauli Master Equation,” *J. Appl. Phys.*, vol. 83, pp. 270–291, 1998.
- [35] M. Fischetti, “Master-Equation Approach to the Study of Electronic Transport in Small Semiconductor Devices,” *Physical Review B*, vol. 59, pp. 4901–4917, 1999.
- [36] G. Lindblad, “On the Generators of Quantum Dynamical Semigroups,” *Communications in Math. Phys.*, vol. 48, pp. 119–130, 1976.
- [37] S. Gao, “Lindblad Approach to Quantum Dynamics of Open Systems,” *Physical Review B*, vol. 57, pp. 4509–4517, 1998.
- [38] H. Nakazato, Y. Hida, K. Yuasa, B. Militello, A. Napoli, and A. Messina, “Solution of the Lindblad Equation in the Kraus Representation,” *Physical Review A*, vol. 74, pp. 0621131–0621138, 2006.
- [39] A. Jünger, *Mathematical Modeling of Semiconductor Devices*.
- [40] A. Pechtl, *Vorlesungen über Theoretische Elektrotechnik, Zweiter Teil: Elektrodynamik*. Institut für Grundlagen und Theorie der Elektrotechnik, TU Wien, 1998.
- [41] S. Selberherr, *Analysis and Simulation of Semiconductor Devices*. Springer Verlag Wien New York, 1984.
- [42] T. Grasser and M. Karner, *Modellierung elektronischer Bauelemente*. Institute for Microelectronics, TU Vienna, 2006. Lecture Notes.
- [43] E. Schrödinger, “Quantisierung als Eigenwertproblem,” *Ann. Phys.*, vol. 79, no. 3, pp. 361–376, 1926.

- [44] M. Karner, “Multi-Dimensional Simulation of Closed Quantum Systems,” Master’s thesis, Technische Universität Wien Fakultät für Elektrotechnik, 2004.
- [45] F. Schwabl, *Quantenmechanik für Fortgeschrittene*. Springer-Verlag Berlin Heidelberg, 2004.
- [46] Y. Tsididis, *Operation and Modeling of the MOS Transistor*. McGraw-Hill Series in Electrical Engineering, 1987.
- [47] T. Ando, A. Fowler, and F. Stern, “Electronic Properties of Two-Dimensional Systems,” *Review of Modern Physics*, vol. 1982, pp. 437–672, 1982.
- [48] D. Grau, *Übungsaufgaben zur Quantentheorie*. Carl Hanser Verlag München Wien, 1993.
- [49] A. Trellakis, A. Galick, A. Pacelli, and U. Ravaioli, “Iteration Scheme for the Solution of the Two-Dimensional Schrödinger-Poisson Equations in Quantum Structures,” *J.Appl.Phys.*, vol. 81, pp. 7881–7884, 1997.
- [50] M. Vasicek, M. Karner, E. Ungersböck, M. Wagner, H. Kosina, and T. Grasser, “Modeling of Macroscopic Transport Parameters in Inversion Layers,” in *Simulation of Semiconductor Processes and Devices*, 2007.
- [51] T. Grasser, “Non-Parabolic Macroscopic Transport Models for Semiconductor Device Simulation,” *Physica A*, vol. 349, pp. 221–258, 2005.
- [52] P. Markowich, C. Ringhofer, and C. Schmeiser, *Semiconductor Equations*. Springer-Verlag Wien New York, 1990.
- [53] A. Jüngel, *Transport Equations for Semiconductors*. Institut für Mathematik Johannes Gutenberg-Universität Mainz, 2004.
- [54] W. Nolting, *Grundkurs Theoretische Physik 6: Statistische Physik*. Springer Berlin - Heidelberg, 2002.
- [55] A. Vlasov, “On Vibration Properties of Electron Gas,” *J. Exp. Theor. Phys.*, vol. 8, pp. 444–470, 1938.
- [56] W. Ludwig, *Festkörperphysik*. Akademische Verlagsgesellschaft Wiesbaden, 1978.
- [57] C. Jacoboni and P. Lugli, *The Monte Carlo Method for Semiconductor Device Simulation*. Springer Wien - New York, 1989.
- [58] P. Palestri, M. Mastrapasqua, A. Pacelli, and C. King, “A Drift-Diffusion/Monte Carlo Simulation Methodology for Si<sub>1-x</sub>Ge<sub>x</sub> HBT Design,” *IEEE Trans.Electron Devices*, vol. 49, pp. 1242–1249, July 2002.
- [59] C. Huang, T. Wang, C. Chen, M. Chang, and J. Fu, “Modeling Hot-Electron Gate Current in Si MOSFET’s using a coupled Drift-Diffusion and Monte Carlo Method,” *IEEE Trans.Electron Devices*, vol. 39, pp. 2562–2568, Nov 1992.
- [60] S. Bandyopadhyay, M. Klausmeier-Brown, C. Maziar, S. Datta, and M. Lundstrom, “A Rigorous Technique to Couple Monte Carlo and Drift-Diffusion Models for Computationally Efficient Device Simulation,” *IEEE Trans.Electron Devices*, vol. 34, pp. 392–399, Feb 1987.

- [61] Ashcroft and Mermin, *Solid State Physics*. Harcourt College Publishers, 1976.
- [62] H. Sørensen, P. Hansen, D. Petersen, S. Skelboe, and K. Stokbro, “Efficient Wave-Function Matching Approach for Quantum Transport Calculations,” *Physical Review B*, vol. 79, pp. 205322–1–205322–10, 2009.
- [63] G. Bir and G. Pikus, *Symmetry and Strain-Induced Effects in Semiconductors*. J.Wiley & Sons New York, 1974.
- [64] C. Kittel, *Quantentheorie der Festkörper*. Oldenburg, 1989.
- [65] M. Fischetti, “Monte Carlo Simulation of Transport in Technologically Significant Semiconductors of the Diamond and Zinc-Blend Structures–Part 1: Homogeneous Transport,” *IEEE Trans.Electron Devices*, vol. 38, pp. 634–649, 1991.
- [66] M. Fischetti and S. Laux, “Monte Carlo Simulation of Transport in Technologically Significant Semiconductors of the Diamond and Zinc-Blende Structures. II. Submicrometer MOSFET’s,” *IEEE Trans.Electron Devices*, vol. 38, pp. 650–660, March 1991.
- [67] W. Nolting, *Grundkurs Theoretische Physik 7: Viel-Teilchen-Theorie*. Springer, 2001.
- [68] F. Jensen, *Introduction to Computational Chemistry*. Wiley, 2006.
- [69] R. Martin, *Electronic Structure: Basic Theory and Practical Methods*. Cambridge University Press, 2004.
- [70] E. Kane, “Band Structure of Indium Antimonide,” *J.Phys.Chem.Solids*, vol. 1, pp. 249–261, 1957.
- [71] S. Laux and M. Fischetti, “Monte-Carlo Simulation of Submicrometer Si n-MOSFET’s at 77 and 300 K,” *IEEE Electron Device Lett.*, vol. 9, pp. 467–469, 1988.
- [72] B. Vinter, “Subband Energies in N-Channel Inversion Channel on (111) Ge,” *Physical Review B*, vol. 20, pp. 2395–2397, 1979.
- [73] S. Dhar, *Analytical Mobility Models for Strained Silicon-Based Devices*. PhD thesis, Technische Universität Wien Fakultät für Elektrotechnik, 2007.
- [74] M. Pourfath, *Numerical Study of Quantum Transport in Carbon Nanotube-Based Transistors*. PhD thesis, Technische Universität Wien Fakultät für Elektrotechnik, 2007.
- [75] A. Gehring, *Simulation of Tunneling in Semiconductor Devices*. PhD thesis, Technische Universität Wien Fakultät für Elektrotechnik, 2003.
- [76] S. Datta, “The Non-Equilibrium Green’s Function (NEGF) Formalism: An Elementary Introduction,” in *Proc. Digest. International Electron Devices Meeting IEDM ’02*, pp. 703–706, 8–11 Dec. 2002.
- [77] R. Lake and S. Datta, “Non-Equilibrium Green’s Function Method Applied to Double-Barrier Resonant-Tunneling Diodes,” *Physical Review B*, vol. 45, pp. 6670–6686, 1992.
- [78] S. Datta, “Nanoscale Device Modeling: The Green’s Function Method,” *Superlattices & Microstructures*, vol. 28, pp. 253–278, 2000.

- [79] M. Anantram, M. Lundstrom, and D. Nikonov, "Modeling of Nanoscale Devices," *cond-mat/0610247*, 2006.
- [80] H. Kosina, M. Nedjalkov, and S. Selberherr, "A Monte Carlo Method Seamlessly Linking Quantum and Classical Transport Calculations," *J.Comput.Electronics*, vol. 2, pp. 147–151, 2003.
- [81] V. Sverdlov, T. Grasser, and H. Kosina, "Scattering and Space-Charge Effects in Wigner Monte Carlo Simulations of Single and Double Barrier Devices," *J.Comput.Electronics*, vol. 5, pp. 447–450, 2006.
- [82] M. Nedjalkov, E. Atanassov, H. Kosina, and S. Selberherr, "Operator-Split Method for Variance Reduction in Stochastic Solutions of the Wigner Equation," *Monte Carlo Methods and Appl.*, vol. 10, pp. 461–468, 2004.
- [83] H. Kosina, M. Nedjalkov, and S. Selberherr, "Solution of the Space-dependent Wigner Equation using a Particle Model," *Monte Carlo Methods and Appl.*, vol. 10, pp. 359–368, 2004.
- [84] H. Kosina, "Wigner Function Approach to Nano Device Simulation," *Int. J. Computational Science and Engineering*, vol. 2, pp. 100–118, 2006.
- [85] E. Wigner, "On the Quantum Correction for Thermodynamic Equilibrium," *Physical Review*, vol. 40, pp. 749–759, 1932.
- [86] M. Nedjalkov, H. Kosina, and S. Selberherr, *Large-Scale Scientific Computing*, ch. A Weight Decomposition Approach to the Sign Problem in Wigner Transport Simulations, pp. 178–184. Springer Berlin/Heidelberg, 2004.
- [87] L. Shifren, C. Ringhofer, and D. Ferry, "A Wigner Function-Based Quantum Ensemble Monte Carlo Study of a Resonant Tunneling Diode," *IEEE Trans.Electron Devices*, vol. 50, pp. 769–773, March 2003.
- [88] S. Bertoluzza and P. Pietra, "Space-Frequency Adaptive Approximation for Quantum Hydrodynamic Models," *J. Trans. Theory and Stat. Phys*, vol. 29, pp. 375–395, 2000.
- [89] G. Paasch and H. Übensee, "A Modified Local Density Approximation Electron Density in Inversion Layers," *Phys.stat.sol.(b)*, vol. 113, pp. 165–178, 1982.
- [90] W. Hänsch, T. Vogelsang, R. Kircher, and M. Orłowski, "Carrier Transport near the Si/SiO<sub>2</sub> Interface of a MOSFET," *Solid-State Electron.*, vol. 32, pp. 839–849, 1989.
- [91] M. Wagner, M. Karner, J. Cervenka, M. Vasicek, H. Kosina, S. Holzer, and T. T. Grasser, "Quantum Correction for DG MOSFETs," *J.Comput.Electronics*, vol. 5, pp. 397–400, 2006.
- [92] C. Jungemann, C. Nguyen, B. Neinhüs, S. Decker, and B. Meinerzhagen, "Improved Modified Local Density Approximation for Modeling of Size Quantization in NMOSFETs," in *Proc. Intl. Conf. Modeling and Simulation of Microsystems 2001*, 2001.
- [93] C. Nguyen, C. Jungemann, and B. Meinerzhagen, "Modeling of Size Quantization in Strained Si-nMOSFETs with the Improved Modified Local Density Approximation," in *NSTI-Nanotech*, 2005.

- [94] M. Karner, M. Wagner, T. Grasser, and H. Kosina, “A Physically Based Quantum Correction Model for DG MOSFETs,” in *Materials Research Society Spring Meeting (MRS)*, 2006.
- [95] M. V. Dort, P. Woerlee, and A. Walker, “A Simple Model for Quantisation Effects in Heavily-Doped Silicon MOSFETs at Inversion Conditions,” *Solid-State Electron.*, vol. 37, pp. 411–414, 1994.
- [96] F. Bufler, Y. Asahi, H. Yoshimura, C. Zechner, A. Schenk, and W. Fichtner, “Monte Carlo Simulation and Measurement of Nanoscale n-MOSFETs,” *IEEE Trans. Electron Devices*, vol. 50, pp. 418–424, Feb. 2003.
- [97] C. Jungemann, “Advances in Spherical Harmonics Solvers for the Boltzmann Equation,” in *Proc. 9th International Conference on Solid-State and Integrated-Circuit Technology ICSICT 2008*, pp. 357–360, 20–23 Oct. 2008.
- [98] C. Levermore, “Moment Closure Hierarchies for Kinetic Theories,” *J. Stat. Phys.*, vol. 83, pp. 1021–1065, 1996.
- [99] A. Anile and O. Muscato, “Improved Hydrodynamic Model for Carrier Transport in Semiconductor,” *Physical Review B*, vol. 51, pp. 728–740, 1995.
- [100] A. Anile and S. Pennisi, “Extended Thermodynamics of the Blotekjaer Hydrodynamical Model for Semiconductors,” *Continuum Mech. Thermodyn.*, vol. 4, pp. 187–197, 1992.
- [101] O. Muscato and V. Romano, “Simulation of Submicron Silicon Diodes with a Non-Parabolic Hydrodynamical Model based on the Maximum Entropy Principle,” in *Book of Abstracts Computational Electronics IWCE Glasgow 2000. 7th International Workshop on*, pp. 94–95, 22–25 May 2000.
- [102] B. Neinhüs, *Hierarchische Bauelementsimulationen von Si/SiGe Hochfrequenztransistoren*. PhD thesis, Universität Bremen, 2002.
- [103] S. C. Brugger, *Moments of the Inverse Scattering Operator*. Series in Microelectronics, 2006.
- [104] K. Blotekjaer, “Transport Equations for Electrons in Two-Valley Semiconductors,” *IEEE Trans. Electron Devices*, vol. ED-17, pp. 38–47, Jan. 1970.
- [105] M. Gritsch, H. Kosina, T. Grasser, and S. Selberherr, “Revision of the Standard Hydrodynamic Transport Model for SOI Simulation,” *IEEE Trans. Electron Devices*, vol. 49, pp. 1814–1820, Oct. 2002.
- [106] M. Gritsch, *Numerical Modeling of Silicon on Insulator MOSFETs*. PhD thesis, Technische Universität Wien Fakultät für Elektrotechnik, 2002.
- [107] M. Wagner, *Simulation of Thermoelectric Devices*. PhD thesis, Technischen Universität Wien Fakultät für Elektrotechnik, 2007.
- [108] R. Kosik, T. Grasser, R. Entner, and K. Dragosits, “On the Highest Order Moment Closure Problem,” in *Proceedings IEEE International Spring Seminar on Electronics Technology 27th ISSE 2004*, pp. 118–120, IEEE, 2004.

- [109] T. Grasser, R. Kosik, C. Jungemann, B. Meinerzhagen, H. Kosina, and S. Selberherr, "A Non-Parabolic Six Moments Model for the Simulation of Sub-100 nm Semiconductor Devices," *J.Comput.Electronics*, vol. 3, pp. 183–187, 2004.
- [110] D. Caughey and R. Thomas, "Carrier Mobilities in Silicon Empirically Related to Doping and Field," *Proc.IEEE*, vol. 55, pp. 2192–2193, Dec. 1967.
- [111] S. Selberherr, W. Hänsch, M. Seavey, and J. Slotboom, "The Evolution of the MINIMOS Mobility Model," *Archiv für Elektronik und bertragungstechnik*, vol. 44, pp. 161–171, 1990.
- [112] C. Jungemann and B. Meinerzhagen, *Hierarchical Device Simulation The Monte Carlo Perspective*. Springer Wien New York, 2003.
- [113] H. Wang, R.Jaszczak, and R. Coleman, "Monte Carlo Modeling of Penetration Effect for Iodine-131 Pinhole Imaging," *IEEE J. Nuclear Science*, vol. 43, pp. 3272–3277, Dec. 1996.
- [114] G. Fishman, *Monte Carlo Concepts, Algorithms, and Applications*. Springer Series in Operations Research, 1996.
- [115] M. Newman and G. Barkema, *Monte Carlo Methods in Statistical Physics*. Oxford University Press, 2002.
- [116] T. Yu and K. Brennan, "Monte Carlo Calculation of Two-Dimensional Electron Dynamics in GaN&lGaN Heterostructures," *J.Appl.Phys.*, vol. 91, pp. 3730–3736, Mar 2002.
- [117] H. Kosina, M. Nedjalkov, and S. Selberherr, "The Stationary Monte Carlo Method for Device Simulation. I. Theory," *Journal of Applied Physics*, vol. 93, pp. 3553–3563, Mar 2003.
- [118] R. Frühwirth and M. Regler, *Monte-Carlo Methoden, Eine Einführung*. B. I. Wissenschaftsverlag Mannheim, Wien, Zürich, 1983.
- [119] H. Kosina, *Simulation des Ladungstransportes in elektronischen Bauelementen mit Hilfe der Monte-Carlo-Methode*. PhD thesis, Technischen Universität Wien Fakultät für Elektrotechnik, 1992.
- [120] F. Buffer, *Full-Band Monte Carlo Simulation of Nanoscale Strained-Silicon MOSFETs*. Series in Microelectronics, 2003.
- [121] C. Jacoboni, "A new Approach to Monte Carlo Simulation," in *Proc. International Electron Devices Meeting Technical Digest*, pp. 469–472, 3–6 Dec. 1989.
- [122] C. Troger, *Modellierung von Quantisierungseffekten in Feldeffekttransistoren*. PhD thesis, Technische Universität Wien Fakultät für Elektrotechnik, 2001.
- [123] L. Wang, "Monte-Carlo-Simulation des Elektronentransports in Technologisch Signifikanten Halbleitern," Master's thesis, Technische Universität Wien Fakultät für Elektrotechnik, 1995.
- [124] T. Tang and H. Gan, "Two Formulations of Semiconductor Transport Equations based on Spherical Harmonic Expansion of the Boltzmann Transport Equation," *IEEE Trans.Electron Devices*, vol. 47, pp. 1726–1732, Sept. 2000.

- [125] C. Lang and N. Pucker, *Mathematische Methoden in der Physik*. Spektrum Akademischer Verlag, 1998.
- [126] M. Abramowitz and A. Stegun, *Handbook of Mathematical Functions*. United States Department of Commerce, 1972.
- [127] C. Jungemann, A. Pham, and B. Meinerzhagen, “Stable Discretization of the Boltzmann Equation based on Spherical Harmonics, Box Integration, and a Maximum Entropy Disipation Principle,” *J.Appl.Phys.*, vol. 100, p. 13, 2006.
- [128] K. Rahmat, “Simulation of Hot Carriers in Semiconductor Devices,” tech. rep., The Research Laboratory of Electronics Massachusetts Institute of Technology, 1995.
- [129] D. Ventura, A. Gnudi, and G. Baccarani, “A Deterministic Approach to the Solution of the BTE in Semiconductors,” *Revista Del Nuovo Cimento*, vol. 18, pp. 1–33, 1996.
- [130] S. Laux and M. Fischetti, “Transport Models for Advanced Device Simulation-Truth or Consequences?,” in *Proc. Bipolar/BiCMOS Circuits and Technology Meeting the 1995*, pp. 27–34, 2–3 Oct. 1995.
- [131] M. Vasicek, J. Cervenka, M. Wagner, M. Karner, and T. Grasser, “A 2D Non-Parabolic Six-Moments Model,” *Solid-State Electron.*, vol. 52, pp. 1606–1609, 2008.
- [132] Institut für Mikroelektronik, Technische Universität Wien, *Minimos-NT 2.0 User’s Guide*, *I $\mu$ E*, 2002.
- [133] F. Agostino and D. Quercia, “Short-Channel Effects in MOSFETs,” tech. rep., Introduction to VLSI design (EECS 467), 2000.
- [134] F. Assaderaghi, P. Ko, and C. Hu, “Observation of Velocity Overshoot in Silicon Inversion Layers,” *IEEE Electron Device Lett.*, vol. 14, pp. 484–486, Oct. 1993.
- [135] F. Assaderaghi, D. Sinitsky, H. Gaw, J. Bokor, P. Ko, and C. Hu, “Saturation Velocity and Velocity Overshoot of Inversion Layer Electrons and Holes,” in *Proc. International Electron Devices Meeting Technical Digest*, pp. 479–482, 11–14 Dec. 1994.
- [136] A. Das and M. Lundstrom, “Does Velocity Overshoot reduce Collector Delay Time in AlGaAs/GaAs HBTs?,” *IEEE Electron Device Lett.*, vol. 12, pp. 335–337, June 1991.
- [137] S. Laux and M. Fischetti, “Monte Carlo Study of Velocity Overshoot in Switching a 0.1-Micron CMOS Inverter,” in *Proc. International Electron Devices Meeting Technical Digest*, pp. 877–880, 7–10 Dec. 1997.
- [138] T. Mizuno and R. Ohba, “Experimental study of carrier velocity overshoot in sub-0.1  $\mu$ m devices-physical limitation of MOS structures,” in *Proc. International Electron Devices Meeting*, pp. 109–112, 8–11 Dec. 1996.
- [139] R. Quay, *Analysis and Simulation of High Electron Mobility Transistors*. PhD thesis, Technische Universität Wien Fakultät für Elektrotechnik, 2001.
- [140] A.Schenk, *Halbleiterbauelemente-Physikalische Grundlagen und Simulation*. ETH Zurich, Integrated Systems Laboratory, 2001.



- [141] T. Grasser, H. Kosina, C. Heitzinger, and S. Selberherr, "Characterization of the Hot Electron Distribution Function using Six Moments," *J.Appl.Phys.*, vol. 91, pp. 3869–3879, 2001.
- [142] L. Keldysh, "Concerning the Theory of Impact Ionization in Semiconductors," *Soviet Phys.JETP*, vol. 21, pp. 1135–1144, 1965.
- [143] D. Chen, E. Kan, U. Ravaioli, C. Shu, and R. Dutton, "An Improved Energy Transport Model including Nonparabolicity and Non-Maxwellian Distribution Effects," *IEEE Electron Device Lett.*, vol. 13, no. 1, pp. 26–28, 1992.
- [144] D. Chen, E. Sangiorgi, M. Pinto, E. Kn, U. Ravaioli, and R. Dutton, "Analysis of Spurious Velocity Overshoot in Hydrodynamic Simulations," in *Proc. NUPAD IV Numerical Modeling of Processes and Devices for Integrated Circuits Workshop on*, pp. 109–114, 1992.
- [145] T. Tang, S. Ramaswamy, and J. Nam, "An Improved Hydrodynamic Transport Model for Silicon," *IEEE Trans.Electron Devices*, vol. 40, no. 8, pp. 1469–1477, 1993.
- [146] D. Esseni and A. Abramo, "Modeling of Electron Mobility Degradation by Remote Coulomb Scattering in Ultrathin Oxide MOSFETs," *IEEE Trans.Electron Devices*, vol. 50, pp. 1665–1674, July 2003.
- [147] D. Esseni, "On the Modeling of Surface Roughness Limited Mobility in SOI MOSFETs and Its Correlation to the Transistor Effective Field," *IEEE Trans.Electron Devices*, vol. 51, pp. 394–401, March 2004.
- [148] L. Lucci, P. Palestri, D.Esseni, and L.Selmi, "Multi-Subband Monte Carlo Modeling of Nano-MOSFETs with Strong Vertical Quantization and Electron Gas Degeneration," in *IEEE International Electron Devices Meeting*, 2005.
- [149] B. Neinhüs, C. Nguyen, C. Jungemann, and B. M. u, "A CPU Efficient Electron Mobility Model for MOSFET Simulation with Quantum Corrected Charge Densities," in *Solid-State Device Research Conference, 2000. Proceeding of the 30th European*, 2000.
- [150] M. Fischetti and S. Laux, "Monte Carlo Study of Electron Transport in Silicon Inversion Layers," in *Proc. International Electron Devices Meeting Technical Digest*, pp. 721–724, 13–16 Dec. 1992.
- [151] M. Fischetti and S. Laux, "Monte Carlo Study of Sub-Band-Gap Impact Ionization in Small Silicon Field-Effect Transistors," in *Proc. International Electron Devices Meeting*, pp. 305–308, 10–13 Dec. 1995.
- [152] M. Fischetti, S. Laux, and A. Kumar, "Simulation of Quantum Transport in Small Semiconductor Devices," in *Proc. International Conference on Simulation of Semiconductor Processes and Devices SISPAD 2005*, pp. 19–22, 01–03 Sept. 2005.
- [153] M. Karner, A. Gehring, S. Holzer, M. Pourfath, M. Wagner, H. Kosina, T. Grasser, and S. Selberherr, "VSP - A Multi-Purpose Schrödinger-Poisson Solver for TCAD Applications," in *11th Workshop on Computational Electronics*, 2006.
- [154] Institut für Mikroelektronik, Technische Universität Wien, *VMC 2.0 Users Guide*, 2006.

- [155] S. Jin, M. Fischetti, and T. Wang, "Modeling of Surface-Roughness Scattering in Ultrathin-Body SOI MOSFETs," *IEEE Trans. Electron Devices*, vol. 54, pp. 2191–2203, 2007.
- [156] S. Goodnick, D. Ferry, C. Wilmsen, Z. Liliental, D. Fathy, and O. Krivanek, "Surface Roughness at the Si(100)-SiO<sub>2</sub> Interface," *Physical Review B*, vol. 32, pp. 8171–8186, 1985.
- [157] D. Ferry and S. Goodnick, *Transport in Nanostructures*. Cambridge University Press, 1997.
- [158] R. Prange and T. Nee, "Quantum Spectroscopy of the Low-Field Oscillations in the Surface Impedance," *Physical Review*, vol. 168, pp. 779–786, 1968.
- [159] S. Takagi, A. Toriumi, M. Iwase, and H. Tango, "On the Universality of Inversion Layer Mobility in Si MOSFET's: Part 11-Effects of Surface Orientation," *IEEE Trans. Electron Devices*, vol. 41, pp. 2363–2368, 1994.
- [160] A. Khakifirooz and D. Antoniadis, "On the Electron Mobility in Ultrathin SOI and GOI," *IEEE Trans. Electron Devices Letters*, vol. 25, pp. 80–82, 2004.
- [161] F. Gamiz and M. V. Fischetti, "Monte Carlo Simulation of Double-Gate Silicon-On-Insulator Inversion Layers: The Role of Volume Inversion," *J. Appl. Phys.*, vol. 89, pp. 5478–5487, 2001.
- [162] L. Lucci, D. Esseni, P. Palestri, and L. Selmi, "Comparative Analysis of Basic Transport Properties in the Inversion Layer of Bulk and SOI MOSFETs: A Monte-Carlo Study," in *Proc. Proceeding of the 34th European Solid-State Device Research conference ESSDERC 2004*, pp. 321–324, 21–23 Sept. 2004.
- [163] L. Lucci, P. Palestri, D. Esseni, L. Bergagnini, and L. Selmi, "Multisubband Monte Carlo Study of Transport, Quantization, and Electron-Gas Degeneration in Ultrathin SOI n-MOSFETs," *IEEE Trans. Electron Devices*, vol. 54, pp. 1156–1164, May 2007.
- [164] S. Monfray, T. Skotnicki, P. Coronel, S. Harrison, D. Chanemougame, F. Payet, D. Dartartre, A. Talbot, and S. Borel, "Applications of SiGe Material for CMOS and Related Processing," in *Proc. Bipolar/BiCMOS Circuits and Technology Meeting*, pp. 1–7, 8–10 Oct. 2006.
- [165] J. Hamel, Y. Tang, and K. Osman, "Technological Requirements for a Lateral SiGe HBT Technology Including Theoretical Performance Predictions Relative to Vertical SiGe HBTs," *IEEE Trans. Electron Devices*, vol. 49, pp. 449–456, March 2002.
- [166] U. Konig, A. Gruhle, and A. Schuppen, "SiGe Devices and Circuits: Where are Advantages over III/V?," in *Proc. th Annual IEEE Gallium Arsenide Integrated Circuit (GaAs IC) Symposium Technical Digest 1995*, pp. 14–17, 29 Oct.–1 Nov. 1995.
- [167] J. Blakemore, "Semiconductor and other Major Properties of Gallium Arsenide," *J. Appl. Phys.*, vol. 53, pp. 123–181, 1982.
- [168] J. Ruch, "Electron Dynamics in Short Channel Field-Effect Transistors," *IEEE Trans. Electron Devices*, vol. ED-19, pp. 652–654, 1972.

- [169] T. Aigo, H. Yashiro, A. Jono, A. Tachikawa, and A. Moritani, "Comparison of Electronic Characteristics and Thermal Resistance for HEMTs Grown on GaAs and Si Substrates," *Electron.Lett.*, vol. 28, pp. 1737–1738, 1992.
- [170] T. Ishida, T. Nonaka, C. Yamagishi, Y. Kawarada, Y. Sano, M. Akiyama, and K. Kaminishi, "VIB-7 GaAs MESFET Ring Oscillator on Si Substrate," *IEEE Trans. Electron Devices*, vol. 31, pp. 1988–1988, Dec 1984.
- [171] I. Thayne, G. Jensen, M. Holland, C. Y. A. L. Weigi, A. Paulsen, J. Davies, S. Beaumont, and P. Bhattacharya, "Comparison of 80-200 nm Gate Length Al<sub>0.25</sub>As/GaAs/(GaAs:AlAs), Al<sub>0.3</sub>As/In<sub>0.15</sub>As/GaAs, and In<sub>0.52</sub>As/In<sub>0.65</sub>As/InP HEMTs," *IEEE Trans. Electron Devices*, vol. 42, pp. 2047–2055, Dec. 1995.

---

## Own Publications

---

- [1] M. Vasicek, V. Sverdlov, J. Cervenka, T. Grasser, H. Kosina, and S. Selberherr “Transport in Nanostructures: A Comparative Analysis Using Monte Carlo Simulation, the Spherical Harmonic Method, and Higher Moments Models” in *7th International Conference on Large-Scale Scientific Computations*, 2009.
- [2] M. Vasicek, T. Grasser, “Advanced Macroscopic Transport Models” in *Quantum Systems and Devices: Analysis, Simulations, Applications*, pp. 32, 2009.
- [3] M. Vasicek, M. Cervenka, M. Karner, and T. Grasser, “Consistent Higher-Order Transport Models for SOI MOSFETs” in *International Conference on Simulation of Semiconductor Processes and Devices 2008*, pp. 129–132, 2008.
- [4] M. Karner, O. Baumgartner, M. Pourfath, M. Vasicek, and H. Kosina, “Investigation of a MOSCAP Using NEGF” in *2007 International Semiconductor Device Research Symposium*, 2007.
- [5] M. Vasicek, J. Cervenka, M. Wagner, M. Karner, T. Grasser, “A 2D Non-Parabolic Six-Moments Model” *J.Solid State Electronics*, vol. 3, pp. 168–173, 2008.
- [6] M. Vasicek, J. Cervenka, M. Wagner, M. Karner, and T. Grasser, “A 2D-Non-Parabolic Six Moments Model” in *2007 International Semiconductor Device Research Symposium*, 2007.
- [7] M. Vasicek, J. Cervenka, M. Karner, M. Wagner, T. Grasser, “Parameter Modeling for Higher-Order Transport Models in UTB SOI MOSFETs” *J.Comput.Electronics*, vol. 3, pp. 168–173, 2008.
- [8] M. Vasicek, J. Cervenka, M. Karner, M. Wagner, and T. Grasser, “Parameter Modeling for Higher-Order Transport Models in UTB SOI MOSFETs,” in *12th International Workshop on Computational Electronics Book of Abstracts*, pp. 96–97, 2007.
- [9] M. Vasicek, M. Karner, E. Ungersböck, M. Wagner, H. Kosina, and T. Grasser, “Modeling of Macroscopic Transport Parameters in Inversion Layers,” in *International Conference on Simulation of Semiconductor Processes and Devices 2007*, pp. 201–204, 2007.

- [10] T. Grasser, M. Vasicek, and M. Wagner, “Higher-Order Moment Models for Engineering Applications,” in *Equadiff, Wien*, 2007.
- [11] M. Wagner, M. Karner, J. Cervenka, M. Vasicek, H. Kosina, S. Holzer, and T. Grasser, “Quantum Correction for DG MOSFETs,” *J.Comput.Electronics*, vol. 5, pp. 397–400, 2007.
- [12] M. Karner, A. Gehring, S. Holzer, M. Pourfath, M. Wagner, W. Gös, M. Vasicek, O. Baumgartner, C. Kernstock, K. Schnass, G. Zeiler, T. Grasser, H. Kosina, and S. Selberherr, “A Multi-Purpose Schrödinger-Poisson Solver for TCAD Applications,” *J.Comput.Electronics*, vol. 6, pp. 179–182, 2007.
- [13] M. Karner, A. Gehring, M. Wagner, R. Entner, S. Holzer, W. Gös, M. Vasicek, T. Grasser, H. Kosina, and S. Selberherr, “VSP-A Gate Stack Analyzer,” in *WODIM 2006 14th Workshop on Dielectrics in Microelectronics Workshop Programme and Abstracts*, pp. 101–102, 2006.
- [14] M. Karner, S. Holzer, W. Gös, M. Vasicek, M. Wagner, H. Kosina, and S. Selberherr, *Physics and Technology of High-k Gate Dielectrics 4*, vol. 3, ch. Numerical Analysis of Gate Stacks, pp. 299–308. The Electrochemical Society; ECS Transactions, 2006.
- [15] M. Karner, S. Holzer, M. Vasicek, W. Gös, M. Wagner, H. Kosina, and S. Selberherr, “Numerical Analysis of Gate Stacks,” in *Meeting Abstracts 2006 Joint International Meeting*, p. 1119, Meeting of the Electrochemical Society (ECS), Cancun, 2006.

---

# Curriculum Vitae

---

**September 3<sup>th</sup>, 1979**

Born in Vienna, Austria.

**June 1998**

High school graduation (*Matura*)  
at the 'Real-Gymnasium der Dominikanerinnen'.



**January 1999**

Compulsory military service, Garde.

**October 1999**

Enrolled in Technical Physics at the Vienna University of Technology, Austria.

**August 2004**

Internship at VATECH.

**November 2005**

Received degree of Diplom-Ingenieur (M.Sc.) in Technical Physics from the Vienna University of Technology.

**January 2006**

Entered doctoral program at the Institute for Microelectronics, Vienna University of Technology, under the supervision of Prof. *Tibor Grasser*.